Spatially-Graded Elastomeric Lattice Structures with Integrated Electronic Sensors

by

Charles M. Dwyer

Submitted in Partial Fulfillment of the Requirements

for the Degree of

Master of Science in Engineering

in the

Chemical Engineering

Program

YOUNGSTOWN STATE UNIVERSITY

December 2021

Spatially Graded Elastomeric Lattice Structures with Integrated Electronic Sensors

Charles M. Dwyer

I hereby release this thesis to the public. I understand that this thesis will be made available from the OhioLINK ETD Center and the Maag Library Circulation Desk for public access. I also authorize the University or other individuals to make copies of this thesis as needed for scholarly research.

Signature:

Charles M. Dwyer, Student Date

Approvals:

Dr. Pedro Cortes, Thesis Advisor Date

Dr. Eric MacDonald, Committee Member Date

Dr. Frank X. Li, Committee Member Date

Dr. Salvatore A. Sanders, Dean of Graduate Studies Date

Abstract

Additive manufacturing has enabled the design and construction of complex structures with intricate and tailored features like functionally-graded lattices. Lattices can be created with varying strut densities, designs, and even materials – all of which change the model's capabilities for specific scenarios. Different lattices are used in protective padding to mitigate impacts seen in sports or military, packaging to protect goods during transit, and in general consumer products like footwear for midsole customizability.

In this research, different elastomeric materials were used to create samples to compare impact absorption capability. These materials included Carbon SIL30, Ultimaker TPU, EOS TPE 300, FormLabs Rebound, NinjaTek NinjaFlex, FormLabs Elastic 50A, and FormLabs Flexible 80A. Combinations of these samples were also studied, producing results in between those of the two separate materials. Lattices can be fused in such a way that optimal responses are produced to soften an impact or to quickly dissipate the energy.

An ionic liquid sensor from the University of Akron was placed inside a lattice designed with a pocket for the sensor during the printing process. The design and customizability of the lattice allows wires to be connected to the carbon nanotube traces and into a voltage source. Thus, a flexible impact sensor was seamlessly integrated into an additively manufactured lattice. A Bluetooth-enabled CC2650 microcontroller was used to relay data to a remote connection, paving the way for live data collection and analysis to determine the severity of impact. Due to increased data collection and customizability, many industries can be made safer and more comfortable for workers, soldiers, athletes, and consumers.

Table of Contents

Abstract iii
Table of Contents iv
List of Figures vi
List of Tables xi
Nomenclature xii
1.0 Introduction 1
1.1 Elastomeric Lattices 1
1.1.1 Applications 1
1.1.2 Foams and Engineered Structures 3
1.2 Lattice Generation and Design 4
1.3 Elastomeric Materials 6
1.3.1 Resin-Based 6
1.3.2 Filament-Based 7
1.3.3 Powder-Based 8
1.4 Flexible Sensor Integration 9
1.5 Motivation for Thesis 9
1.6 Objectives 10
1.7 Organization 11
1.8 Scope of Work 11
2.0 Literature Review 13
2.1 Elastomeric Lattices 13
2.1.1 Applications 13
2.1.2 Protective Impact Foams 15
2.2 Lattice Design 17
2.2.1 TPMS and Rod-and-Ball Lattices 17
2.2.2 Origami-Derived Lattices 18
2.2.3 Prism Structures 19
2.3 Common Elastomers and Flexible Materials 21
2.3.1 Stratasys Tango Black Plus 21
2.3.2 NinjaTek NinjaFlex and SemiFlex 21

2.3.3 Ultimaker TPU 95A 23
2.3.4 Carbon FPU 50 and SIL 30 25
2.3.5 FormLabs Rebound, Flexible 80A, and Elastic 50A 27
2.3.6 EOS TPE 300, TPU 1301, and PA 11 28
2.4 Flexible Sensors 30
2.5 Head and Helmet Safety 32
3.0 Experimental Methodology 35
3.1 Materials and Methods 35
3.2 Quasi-Static Compression Testing 38
3.3 Low Velocity Impact Testing 39
3.3.1 Lattice Testing 40
3.3.2 Helmet System Testing 41
3.3.3 Data Analysis and Processing 42
3.4 Side-Graded Lattice Modeling 42
3.5 Lattice Sensor Testing 45
4.0 Results and Discussion 48
4.1 Individual Lattices 48
4.1.1 SIL 30 and TPU 95A Lattices 49
4.1.2 Quasi-Static Compression of TPE 300, NinjaFlex, and Rebound Lattices 53
4.1.3 Low Velocity Impacting of TPE 300, NinjaFlex, and Rebound Lattices ... 55
4.2 Hybrid Lattices 58
4.2.1 VG ULTI and VG SIL 30 58
4.2.2 VG TPE 300 and NG NinjaFlex 63
4.3 Side-Graded Lattices 69
4.4 Helmet System 73
4.5 Embedded Sensor System 76
5.0 Conclusions 80
References 83

List of Figures

Figure 1.1: Riddell Diamond Technology-based latticed helmet, released in partnership with Carbon [10]. 2
Figure 1.2: Comparison of stiffness of elastomers to foams based on density [20]. 4
Figure 1.3: Common lattice variations; (a) non-graded, (b) vertically-graded, and (c) side-graded. Blue represents thin struts, while red represents thick struts; relative strut sizing is shown under (c). 5
Figure 1.4: Diagram of stereolithography process. Here, the laser cures the resin from the bottom of the tank and the part rises during printing. Some methods of SLA place the laser above the tank and the part sinks into the resin as the layers cure [29]. 7
Figure 1.5: FFF printing method. Molten material is laid in layers and built upon via a hot nozzle. Material is commonly fed to the extruder in a filament form; however, other materials like pellets (FGF printing) can be used as well with modified setups [30,31]. 8
Figure 1.6: SLS process overview. Lasers fuse powdered granules in layers as the part grows downward [32]. 9
Figure 2.1: Hexr helmet with PA 11 honeycomb lining. The simple lattice design greatly reduces the rotational acceleration effects of an oblique impact [39,40]. 14
Figure 2.2: Relative modulus versus relative density for lattice structures, including foams. The labeled slopes represent the restrictions based on failure behavior. These boundaries are challenged with AM-based designed lattices [18]. 15
Figure 2.3: Conehead EPS foam designed with low density (grey) and high density (white) sections. The functionally-graded approach is like what is easily achievable with additively manufactured designed lattices [41]. 16
Figure 2.4: Unit cells of various lattice designs [4]. 17
Figure 2.5: Young's modulus for various lattice geometries at (a) 10% relative density (considered to be relatively low), and (b) 25% relative density (considered to be relatively high) [4]. 18
Figure 2.6: Miura-Ori lattice model exhibiting a stacked folded origami-like arrangement [53]. 19

Figure 2.7: Various prism lattice designs. From left to right: hexagonal, square, diamond, circular, triangular [55]. 19
Figure 2.8: Honeycomb lattices subjected to various impact energies. Notice the high efficiency of the uniformly dense sample (black line) in (b). The efficiency is later traded for increased transmission due to early densification in (c). The functionally-graded honeycombs exhibit a wider working range at the expense of lower efficiency [57]. 20
Figure 2.9: Honeycomb lattice printed from SemiFlex. Photo (a) shows a closeup of the cells and (b) shows the compression response at various strains (ε) [61]..... 22
Figure 2.10: (a) Stress-strain curves for five compression cycles, n, for the SemiFlex honeycomb samples with a relative density of 0.34. (b) SEA values for cycles 1-5. Note the decrease in performance as the number of compression cycles increase [61]. 23
Figure 2.11: Ventilator designed by Ahmed et al. [68] in response to the COVID-19 pandemic. Photo (a) shows the different sizing possible with additive manufacturing and (b) shows the 3D printed parts from differently-colored TPU 95A. The large white vessel is the balloon for the pumping of air into a patient's airways. 25
Figure 2.12: Application of SIL 30 additively manufacturable silicone. (a) Exploded view of COVID-19 customizable N95 mask with silicone seal and (b) assembled mask [75]. 26
Figure 2.13: New Balance shoes made with FormLabs Rebound resin-based lattices [78]. Athletic footwear is a common application of 3D printed lattices. 27
Figure 2.14: EOS Digital Foam helmet liner. Digital Foam technology allows for mass customization of protective foam products [83]. 29
Figure 2.15: Shin guard designed by EOS with PA 11 material [86,89]. The lattice design allows for increased air circulation, while effectively protecting the shins. 30
Figure 2.16: Flexible sensor design consisting of PDMS elastomer and fabric strain sensor (a) in its initial state, and (b) under impact [90]. 31
Figure 2.17: Flexible sensor design using IL layer and CNT traces showing (a) 3D model, (b) side view of sensor, and (c) layer-by-layer construction of sensor [33]. 32
Figure 3.1: Non-graded samples of (a) Carbon SIL 30 and (b) FormLabs Rebound. 36
Figure 3.2: Non-graded samples of (a) NinjaTek NinjaFlex and (b) Ultimaker TPU 95A. 36
Figure 3.3: Non-graded sample of EOS TPE 300. 37

Figure 3.4: Comparison of range of elastic Young's modulus values for various samples and materials. 38
Figure 3.5: Stress versus strain curve for non-graded (NG) EOS TPE 300 lattice during quasi-static compression. Features listed are the elastic Young's modulus and absorbed energy. 39
Figure 3.6: Vertical impact tower setup containing impactor with load cell, fixed bottom platen with sample, and vertical columns for linear ball bearings. 40
Figure 3.7: Helmet impact setup including vertical columns, linear ball bearings, and the modified load cell position. For the impacts, lattices are contained inside a polycarbonate helmet shell to act as padding. 41
Figure 3.8: Average stress-strain curve of five tensile tests of EOS TPE 300 samples. Over 300% elongation at break is observed in these results. 43
Figure 3.9: Final stress-strain curve for TPE 300 fitted with HYPERFIT 2.181 and Ogden 3rd order parameters. The curve was used for modeling the material properties of the TPE 300 elastomer. 44
Figure 3.10: (a) Half lattice with sensor inserted and (b) full lattice with visible signal wiring. 46
Figure 3.11: Circuit schematic of the embedded sensor lattice system. The lattice itself is shown on the left side of the figure, while the microcontroller, labeled MCU, is shown on the right. 46
Figure 3.12: Photo showing complete setup of sensor testing. Included are the power supply (bottom left), breadboard (middle), circuit board (right), and lattice on steel platen for impacting (top). 47
Figure 4.1: Force versus time curves for SIL 30 and TPU 95A (ULTI) lattices at various impact energies (corresponding to 5, 10, 15, 20, and 30 cm heights). 50
Figure 4.2: Force versus displacement curves for SIL 30 and TPU 95A lattices at various impact energies with densification points labeled. 51
Figure 4.3: Absorbed energy at densification for each material and gradation combination, normalized by mass. 52

Figure 4.4: Densification energies for all tested lattice combinations from phase 2. Stiffer materials require more energy to fully compress all struts, which translates to a higher densification energy. 53
Figure 4.5: Microscope images showing (a) thin struts of VG TPE 300, (b) thick struts of TPE 300, (c) thin struts of VG Rebound, and (d) thick struts of VG Rebound. Note the incorrectly filled voids on the Rebound sample (shown by red arrows), which resulted in increased stiffness. 54
Figure 4.6: Energy absorption efficiency for each lattice combination. Optimal lattice configurations can be determined for different levels of displacement. 55
Figure 4.7: Force-time curves for the first four impacts of each material and spatial gradation. Densification is shown by the sharp peak of a force curve. 56
Figure 4.8: Force-displacement curves for the first four impacts of each material and spatial gradation. Densification is shown by the sharp increase in force without increase in displacement. 57
Figure 4.9: Absorbed energy at densification of each lattice material for (a) non-graded and (b) vertically-graded configurations. 58
Figure 4.10: Snapshots of Hybrid 1 impact during the 14.63 J test. Note the immediate densification of SIL 30 and the stiffness of ULTI until the end of the compression. 59
Figure 4.11: Force-time curves for VG ULTI, VG SIL 30, and Hybrid 1. 60
Figure 4.12: Graphs showing (a) absorbed energy at densification for constituent systems and Hybrid 1, and (b) densification SIE for all tested systems. 61
Figure 4.13: Peak energy absorbed at various impact energies versus time until peak energy was observed. 62
Figure 4.14: Acceleration responses of all three lattice configurations. Lower peak accelerations translate to safer impact attenuation. 63
Figure 4.15: Energy absorption efficiency from quasi-static compression testing of double-stacked lattices and Hybrid 2. 64
Figure 4.16: 10.06 J (20 cm) impact of Hybrid 2 from high-speed video footage. TPE 300 is the white lattice on top and NinjaFlex is shown in yellow on the bottom. 65
Figure 4.17: Force versus time data for two selected impact energies from Hybrid 2 testing. Also shown are double-stacked NG NinjaFlex in yellow and VG TPE 300 in grey. 66

Figure 4.18: Percent displacement versus peak measured force during low velocity impacts of double-stacked NG NinjaFlex, VG TPE 300, and Hybrid 2. 67
Figure 4.19: Densification specific impact energy (SIE) for each double-stacked lattice and Hybrid 2. SIE is density-normalized energy absorbed at densification. 68
Figure 4.20: Acceleration results from (a) 3.20 J impact and (b) 10.06 J impact for double-stacked NinjaFlex, TPE 300, and Hybrid 2. 69
Figure 4.21: Self-aligning platen on the Instron universal testing machine compressing a side-graded TPE 300 lattice. The angle was found to be 12°. 70
Figure 4.22: FEA model and experimental data for a 5 cm impact on non-graded TPE 300. 71
Figure 4.23: Frame-by-frame procession of impact with FEA modeling. Red represents areas of high stress and blue represents areas of low stress. 72
Figure 4.24: Force-time curves for SG TPE 300 experimental impact and FEA impact. 73
Figure 4.25: Inside view of helmet shell containing VG TPE 300 and NG NinjaFlex lattices (from the Hybrid 2 arrangement). Also, (b) shows the full helmet apparatus mounted to the linear ball bearings from Figure 3.7. 74
Figure 4.26: Force profiles for the 62.39 J helmet impact (40 cm). The grey curve in (a) shows a traditional helmet foam performance during the same test. 75
Figure 4.27: Acceleration response of the helmet system outfitted with Hybrid 2 padding. Oscillations are observed due to bouncing of the system after impact. 76
Figure 4.28: Oscilloscope data (light) overlaid with MCU data (dark) to compare accuracy of MCU processing with an existing reliable collection method. 77
Figure 4.29: Comparison of sensor output voltages and traditional load cell output voltages during the (a) 7.77 J impact and (b) 28.34 J impact. 78
Figure 4.30: Eight impact heights from load cell and sensor data. Force (N) was derived from the load cell amplifier to find a conversion for the sensor data. 79

List of Tables

Table 2.1: Material properties of Stratasys Tango Black Plus elastomer [59]. 21
Table 2.2: Material properties of NinjaTek NinjaFlex and SemiFlex elastomers [64,65]. 23
Table 2.3: Material properties of Ultimaker TPU 95A [67]. 24
Table 2.4: Material properties of Carbon FPU 50 and SIL 30 flexible plastics [72,74].. 27
Table 2.5: Material properties for FormLabs Rebound, Flexible 80A, and Elastic 50A elastomers [76,79,80]. 28
Table 2.6: Material properties for EOS TPE 300, TPU 1301, and PA 11 flexible plastics [84,85,87]. 30
Table 3.1: Elastomeric thermoplastic material physical properties. 37
Table 3.2: Ogden 3rd order material model parameters based on the average tensile test data of EOS TPE 300. 43
Table 3.3: Updated Ogden 3rd order model parameters with inclusion of load softening and strain-rate hardening. 45
Table 4.1: Impact heights and corresponding energies and velocities as determined from experimental results. 48
Table 4.2: Average accelerations from assorted impacts and spatial variations. 73

Nomenclature

AM	Additive Manufacturing
ASTM	American Society for Testing and Materials
CAD	Computer Aided Design
CNT	Carbon Nanotube
DLS	Digital Light Synthesis
EAE	Energy Absorption Efficiency
EPP	Expanded Polypropylene
EPS	Expanded Polystyrene
EPU	Expanded Polyurethane
EVA	Ethylene Vinyl Acetate
FEA	Finite Element Analysis
FFF	Fused Filament Fabrication
FGF	Fused Granulate Fabrication
FSS	Fabric Strain Sensor
HIC	Head Injury Criterion
HIP	Head Impact Power
IL	Ionic Liquid
ISO	International Organization for Standardization
MCU	Microcontroller Unit
MJ	Material Jetting
ML	Mechanoluminescence
MO	Miura-Ori
NFL	National Football League
NG	Non-Graded
NHTSA	National Highway Traffic Safety Administration
NOCSAE	National Operating Committee for Standards in Athletic Equipment
PA	Polyamide
PDMS	Polydimethylsiloxane

PU	Polyurethane
SEA	Specific Energy Absorption
SG	Side-Graded
SIE	Specific Impact Energy
SIL 30	Carbon Silicon Polyurethane Elastomer
SLA	Stereolithography
SLS	Selective Laser Sintering
TBI	Traumatic Brain Injury
TPE	Thermoplastic Elastomer
TPMS	Triply Periodic Minimal Surface
TPU	Thermoplastic Polyurethane
ULP FEHM	Louis Pasteur University Finite Element Head Model
ULTI	Ultimaker TPU 95A
VG	Vertically-Graded
VPP	Vat Photopolymerization

1.0 Introduction

Elastomeric lattice structures are lightweight alternative systems to traditional impact attenuation devices based on flexible foams [1,2]. Lattices can be tailored to fit individual needs, impact strengths, or even comfort levels through the usage of additive manufacturing (AM) and functionally graded design. AM enables the fabrication of complex structures like lattices based on a wide range of materials. These lattices can be integrated with monitoring gadgets during the printing process, like flexible sensors in elastomers. These sensors have the ability to transmit data wirelessly about the forces experienced by the lattice structure [3]. Elastomeric lattices can also be designed in a way that allows more airflow to keep the equipment cooler overall [4]. These properties may be useful in the sports, military, shipping, and emergency services sectors.

1.1 Elastomeric Lattices

1.1.1 Applications

Contact sports, like American football, can result in many types of injuries, including severe head injury. These are mitigated with the use of helmets and extensive padding; however, research shows that some of the most dangerous impacts occur off-axis. These impacts transmit a rotational acceleration to a wearer's head and can result in serious head injury. Traditional helmets were designed with only linear accelerations in mind, leading to risk of injury from rotational impact conditions [5]. Some head injury metrics were formulated to assess possible damage and protection level from helmets for various impacts. These include the Gadd Severity Index, and the National Highway Traffic Safety Administration's (NHTSA) Head Injury Criterion (HIC) [6]. Interestingly, functionally-graded lattices are more effective at reducing the risk of Traumatic Brain Injury (TBI) than traditional foams, which is a direct result of the various compressive energies required to densify the different parts of a functionally-graded lattice [7–9]. Therefore, AM may play a key role in the development of safer protective equipment in sports. Figure 1.1 shows a helmet manufactured by Riddell and Carbon containing a customizable lattice liner [10].

Figure 1.1: Riddell Diamond Technology-based latticed helmet, released in partnership with Carbon [10].

Another potential use scenario for additively manufactured lattice structures is in the military industry. Many activities require protective gear in the military sector and lattices may be able to contribute a level of customization that has not been achievable yet. By constructing lattice padding that perfectly fits a serviceperson's body or head, the protective equipment is more comfortable and safer faor the wearer [11]. U.S. Army researchers have developed 3D printed lattice structures for use in combat and recreational helmets. These lattice liners are 27% more efficient at energy absorption and have the ability to allow more airflow overall, resulting in a more comfortable experience [12]. Comfort is vital when wearing helmets for extended periods of time in hot climates worldwide.

Motorcycle riders would also benefit from AM technology [13]. One of the most common elements of crashes involve rotational accelerations that current helmet designs are not able to mitigate properly [14]. AM allows rapid experimentation with and design of functionally-graded lattice liners, which aim to solve the oblique impact problem. According to Finite Element Analysis (FEA) modeling done by Khosroshahi et al. [13], functionally-graded lattices reduced the maximum rotational acceleration from an off-axis

impact by 55-70%. Improvements in safety and comfort for consumers, military personnel, and athletes are expected with the inclusion of these lattices.

Worldwide transit of goods is an enormous sector of industry with many uses for protective packaging. Many items that may be prone to breaking on impact are packaged with foams or air bubbles. According to Grand View Research [15], "the global foam protective packaging demand was valued at $5.72 billion in 2016". Additively manufactured lattice structures could be designed in a customized manner so that objects are tightly protected during shipment [16]. The novel padding systems can be reused many times, due to the nature of elastomeric materials [17]. These use scenarios encompass a wide range of industries, from athletics to military, leading to the future popularization of lattice protection in everyday life.

1.1.2 Foams and Engineered Structures

Foams are a main alternative to elastomeric lattices. Foams are generally considered to be a subset of the broader lattice category, exhibiting a stochastic – or randomized – nature [18,19]. Conventionally designed lattices are a type of engineered structure, with perfect gaps and consistent struts or trusses. According to Michael F. Ashby [18], all lattices are governed by stretch-dominated and bend-dominated properties for failure, but foams are mostly bend-dominated. The bending failure mode restriction – without the ability to customize the foam cells as can be done with AM – limits the performance of foams in stiffness and in strength when compared to that of a stretch-dominated similar cell. While foam cells can be only somewhat controlled during creation, AM enables a different kind of customizability on a unit cell basis [19]. Figure 1.2 contains a map of foams and elastomeric materials by density and Young's modulus. The chart shows how foams achieve a similar level of stiffness as elastomers, but with a lower density [20].

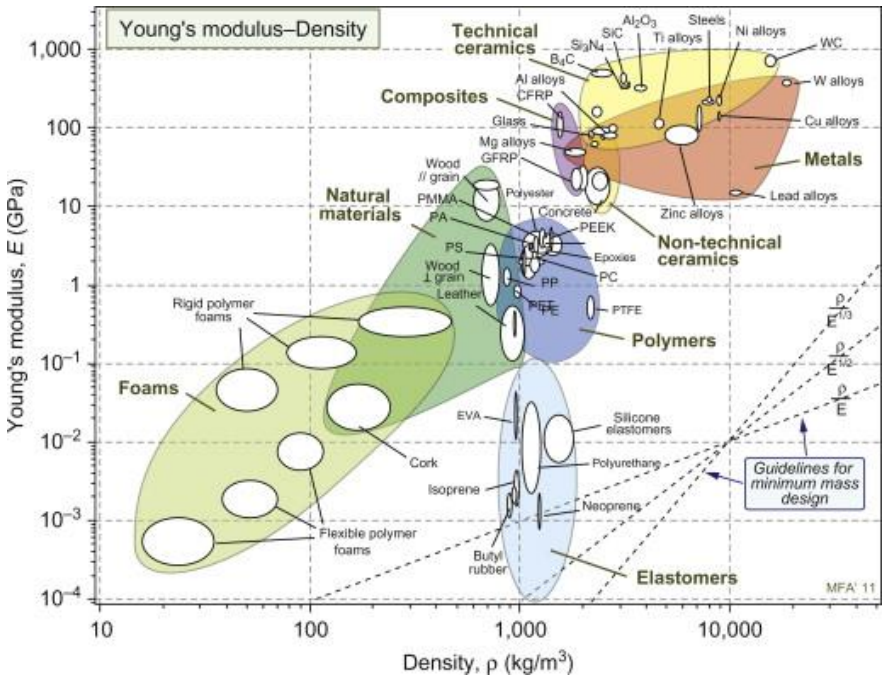

Figure 1.2: Comparison of stiffness of elastomers to foams based on density [20].

1.2 Lattice Generation and Design

Complex models like lattices are much easier to construct with AM compared to most other processes. Within the subset of lattices, there are many different designs with varying properties. Some structures exhibit isotropic properties (for example, they are equally strong in all directions), while others display anisotropic characteristics (stronger in only certain directions). Much of the following research was performed using a Kelvin cell lattice design, which is approximately isotropic [21]. The Kelvin cell design is commonly examined because it is more complex than a simple honeycomb design, while also being isotropic. Isotropy gives a lattice designer more control over the different required gradations and performance capabilities. Kelvin cell lattices display a greater energy absorption capability than most other unit cell configurations [4]. The Kelvin cell design is also categorized as a bending-dominated structure, which absorbs impact energy more efficiently than its counterpart – a stretching-dominated structure [7].

Functionally-graded lattices are easily created from base unit cell designs. The thicknesses of lattice struts and features are slightly varied throughout the structure to

achieve different stiffnesses and energy absorption capabilities. Research shows that the strength of a structure is a strong function of strut thickness [21]. Figure 1.3 displays Kelvin cell lattices in various spatially-graded variations: non-graded, vertically-graded, and side-graded.

Figure 1.3: Common lattice variations; (a) non-graded, (b) vertically-graded, and (c) side-graded. Blue represents thin struts, while red represents thick struts; relative strut sizing is shown under (c).

Lattice generation is usually complex and requires significant computing power. Mithril by Siemens is a robust software that can be used to produce complex systems. Mithril is a unique program for lattice generation that uses Python programming libraries to create extremely compact file sizes. These files can contain up to 1 trillion elements, yet still be much smaller than alternative CAD files. Since the generation is not the same process as current 3D modeling software, C/C++ visualization implementation enables a user to view the generated structure. Using Mithril for lattice generation is helpful in reducing load and render times and file sizes.

n-Topology is another program used for complex lattice generation. The program can "lightweight" an existing model or generate a lattice in a new simple model via its block programming method. Like Mithril, n-Topology allows a user to adjust many different lattice parameters to accomplish functional grading and combined design. Mithril was used for programming the initial test structures and n-Topology for the creation of the later models, which included a cavity for sensors and a modified top and bottom structural conformation for printability.

1.3 Elastomeric Materials

Elastomers have recently become an important class of materials in AM because of their ability to be greatly deformed and still return to their original shape. Some difficulties like stringing and clogging are associated with additively manufacturing elastomeric thermoplastics; however, current technology allows for successful processing using a majority of the ISO/ASTM defined AM techniques [22]. These successful methods include material jetting [23], vat photopolymerization (stereolithography or SLA) [24,25], material extrusion (fused filament fabrication or FFF) [17,26,27], and powder bed fusion (selective laser sintering or SLS) [28].

1.3.1 Resin-Based

The stereolithography process, also referred to as SLA, is a subset of the broader vat photopolymerization (VPP) manufacturing method and is a common way of manufacturing elastomers. These materials begin as resins that can be exposed to a certain wavelength of laser light to be hardened via chemical reaction. The laser exposes small sections of the vat of resin at a time, adhering it to either the build plate or the material directly above it. Stereolithography is a reliable method for processing elastomers with good printing resolution. A diagram of the SLA process is shown in Figure 1.4 [29].

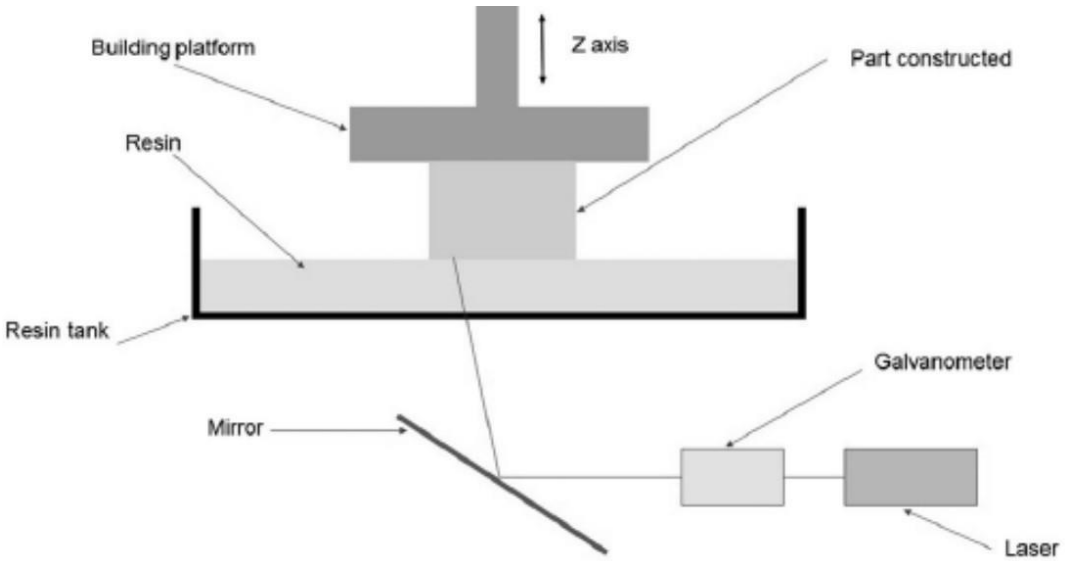

Figure 1.4: Diagram of stereolithography process. Here, the laser cures the resin from the bottom of the tank and the part rises during printing. Some methods of SLA place the laser above the tank and the part sinks into the resin as the layers cure [29].

1.3.2 Filament-Based

Material extrusion, or fused filament fabrication (FFF), is a very common AM method that is used for manufacturing flexible filament materials. The FFF technique is relatively inexpensive, but elastomers are difficult to process due to the feed of filament. Generally, the FFF method consists of a hot nozzle which melts a spool of the polymer into small, extruded layers on a build platform. They are opposite in terms of stiffness, which shows the vast array of properties achievable in a single print method. The FFF method is shown in Figure 1.5 [30].

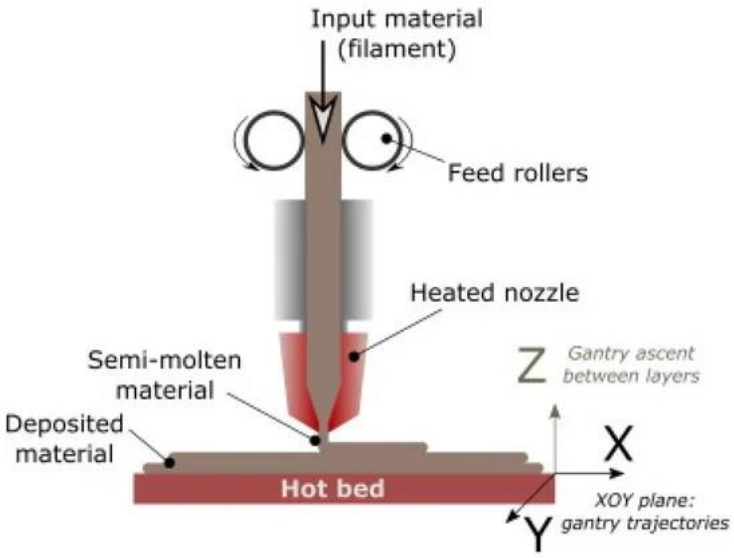

Figure 1.5: FFF printing method. Molten material is laid in layers and built upon via a hot nozzle. Material is commonly fed to the extruder in a filament form; however, other materials like pellets (FGF printing) can be used as well with modified setups [30,31].

1.3.3 Powder-Based

Powder bed fusion, also called selective laser sintering (SLS), is also used to produce elastomeric materials. The SLS manufacturing technique uses lasers to fuse powder together at fine resolutions. Powder bed fusion is comparatively much more expensive than the two aforementioned technologies, but there is significant flexibility in material options beyond thermoplastics. The nature of the SLS AM process allows for recyclability of powder as well, conserving unused material for other parts. An outline of SLS printing can be seen in Figure 1.6 [32].

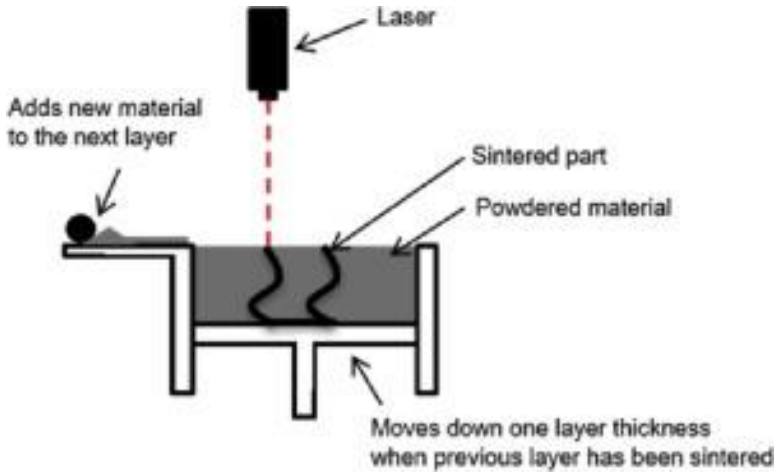

Figure 1.6: SLS process overview. Lasers fuse powdered granules in layers as the part grows downward [32].

1.4 Flexible Sensor Integration

Many commercially-available solutions for pressure sensing units are stiff and can easily break on impact. Researchers are currently exploring new avenues with soft, flexible sensors that can still transmit signals while significantly deformed. One of these sensor types uses ionic liquids (ILs), which can be mixed with a prepolymer resin and used to form a pressure-sensitive layer inside a thin silicone shell [33]. Signals can then be transmitted through carbon nanotube (CNT) traces into wires. Another design of flexible sensor uses a resistive fabric strain sensor layer between PDMS elastomer layers. Finally, phosphorescent materials can be used by measuring induced light output from impact. To protect the sensor, the system must be seamlessly integrated. Solid protection reduces points of failure during repeated impacts and allows the system to function for a longer period. Placing the sensing element inside a printed cavity during printing allows for seamless incorporation.

1.5 Motivation for Thesis

Current integration of elastomeric lattices into protective padding is not widespread. Research has shown that functionally-graded lattices absorb energy more efficiently and are extremely customizable [9]. Use-case flexibility of certain materials is limited due to

printing constraints or basic material properties. For example, all AM methods have a lowest possible resolution, meaning the material cannot be reliably formed into a usable part. Since some materials are so stiff, the thinnest possible strut thickness can be a limiting factor when attempting to make a comfortable lattice. Also, some materials are extremely soft and rubbery; these cannot become any stiffer than they are in solid form. Therefore, problems arise when a lattice needs to be stiffer than physically possible for these materials. Combining multiple materials into one system solves versatility problems. Normal AM with one elastomeric material is extremely customizable but adding different materials to elicit different impact responses increases the tailorability substantially. Greater flexibility can be achieved by the combination of lattice structures with different elastic moduli.

Additively manufactured elastomeric lattices can also house electronic sensors between struts [3]. Lattices can be generated with voids and chambers for different sensors and the structure can be thickened around the sensitive components for protection. These sensors can record and transmit data wirelessly about impact forces experienced in real-time. Therefore, flexible sensor technology could be very useful in athletics and injury prevention. A combination of these ideas could create lattice structures for a vast number of applications in military and athletics wearables to improve safety and data collection.

1.6 Objectives

Most research performed to date examines elastomeric lattices from an FEA modeling perspective or as a simple single material analysis. This research presents data from many different materials under low velocity impact and quasi-static compression conditions; it also focuses on how different materials can be combined into one system to protect against a large range of impact energies. Finally, this research assembles a lattice system with an integrated flexible sensor for data collection without an external load cell.

Specific goals:

- Test various elastomeric thermoplastic materials based on Kelvin cell lattice configurations under quasi-static compression conditions to analyze energy absorption behavior.
- Test lattices under low velocity impact conditions to observe strain-rate dependency and compare densification specific energy absorption.
- Combine two systems based on different rigidities into one structure to test and analyze the performance compromise.
- Incorporate a flexible electrolyte-based sensor into a 3D printed hybrid material design to gather data about impacts without an external load cell.

1.7 Organization

This thesis will be presented in the following order:

1. A review containing a brief overview of elastomeric lattice structures and impact attenuators is presented in the current chapter; included is the significance, purpose, and benefit of the present work.
2. A review of the current experimental research is presented in Chapter 2.0.
3. The experimental setup and techniques are presented in Chapter 3.0.
4. Results and discussions are presented in Chapter 4.0
5. Conclusions of this work are addressed in Chapter 5.0.

1.8 Scope of Work

The designing and testing of lattice structures consisted of six main phases. First, the Kelvin cell design was selected and made with n-Topology and Mithril. Second, elastomeric materials were sourced from various companies to create the designed lattice structures. Next, the lattices were mounted and tested in a universal quasi-static testing machine. The lattices were then tested in a vertically-oriented impact tower with a load cell, amplifier, oscilloscope, and high-speed camera. Results from these tests were

compiled to examine the performance of the individual lattices and combinations of these lattices as “hybrid” structures.

As an expansion of the previous work, the impact tower was modified to accommodate an American football helmet shell with lattice padding. Tests were performed with various materials and combinations inside the industry-standard helmet shell. Also, flexible sensors were obtained for testing from the University of Akron. These sensors were placed inside printed lattice padding to examine the feasibility of real-time data acquisition. All results from the aforementioned tests are summarized in this thesis.

2.0 Literature Review

Considerable research has been performed on the pros and cons of elastomeric lattice structures; however, studies regarding flexible sensor integration and multi-material components are relatively missing from the existing literature. These items can improve comfort and data collection associated with existing additively manufactured protective padding systems. This chapter presents the current literature related to elastomeric lattices, protective equipment, existing lattice design, common elastomeric materials used in AM, and flexible sensors for use inside protective padding.

2.1 Elastomeric Lattices

2.1.1 Applications

Lattices are complex cellular structures made of struts or planes in various combinations to elicit different physical properties [34]. They can be constructed in many ways depending on the use scenario. Common applications include the sports, military, and packaging industries. Substantial research into elastomeric lattices has been performed from the viewpoint of athletic safety improvements. Clough et al. [9] has shown that elastomeric lattices can exhibit a number of improvements compared to existing football or military helmet foams. Elastomers are commonly multi-hit attenuators, meaning that they do not degrade much in impact performance over repeated tests. Multi-hit capabilities are desirable when designing helmet padding that will be reused many times before replacement, like in an NFL football helmet or combat helmet. Lattices can also be designed to perfectly curve with the helmet design, which is ideal for the wearer's comfort and leads to increased ability to absorb energy effectively. Since lattices are constructed of numerous voids in the material, they are also considered to offer improved breathability when compared to existing closed-cell foams. Clough et al. [9,35] found that ordered lattice structures were able to achieve a higher densification strain and specific strength than stochastic foams.

Researchers have also examined the feasibility of incorporating lattices into bicycle helmet design. The currently-used EPS (expanded polystyrene) helmet foam only protects against single-hit scenarios, while a firm elastomer can be reused in multi-hit situations

[36]. Studies estimate that wearing a helmet while riding a bicycle can reduce the risk of a severe head or brain injury by up to 88% [37]. Models produced with lattice-lined helmets show that impacts can be mitigated more safely than EPS foam by reducing peak translational accelerations and spreading out the overall impact time [36]. These features, coupled with the ability to design helmets that are customized to a cyclist's head, make elastomeric lattice padding a viable and more comfortable alternative to traditional protective foams in many different scenarios.

Hexr, a UK-based company, produces additively manufactured bicycle helmets with honeycomb lattices out of Polyamide 11 (PA 11) via powder bed fusion [38]. These helmets are custom fit for comfort and safety purposes. Willinger of Strasbourg University performed impact testing of the helmet [39,40]. According to the results, the Hexr helmet design reduced the risk of brain injury by 30% more than any other EPS helmet. The brain injury risk reduction is due to its superior impact energy mitigation and oblique impact performance. Ultimately, the helmet received its European Certification from the British Standards Institute in 2019 with adequate performance in linear acceleration testing [40]. The helmet design is pictured below in Figure 2.1.

Figure 2.1: Hexr helmet with PA 11 honeycomb lining. The simple lattice design greatly reduces the rotational acceleration effects of an oblique impact [39,40].

2.1.2 Protective Impact Foams

Ashby [18,20] has performed significant research into the behaviors of foams and lattices as mentioned previously. Figure 2.2 shows a graph of relative modulus versus relative density of various experimentally-studied materials. The ability to modify the bending or stretching nature of a lattice through design and AM enables certain areas of the chart to be filled. The slopes shown are ideal behaviors and restrict conventional materials to these spaces. Lattices made with AM can help bridge these gaps based on application and desired performance.

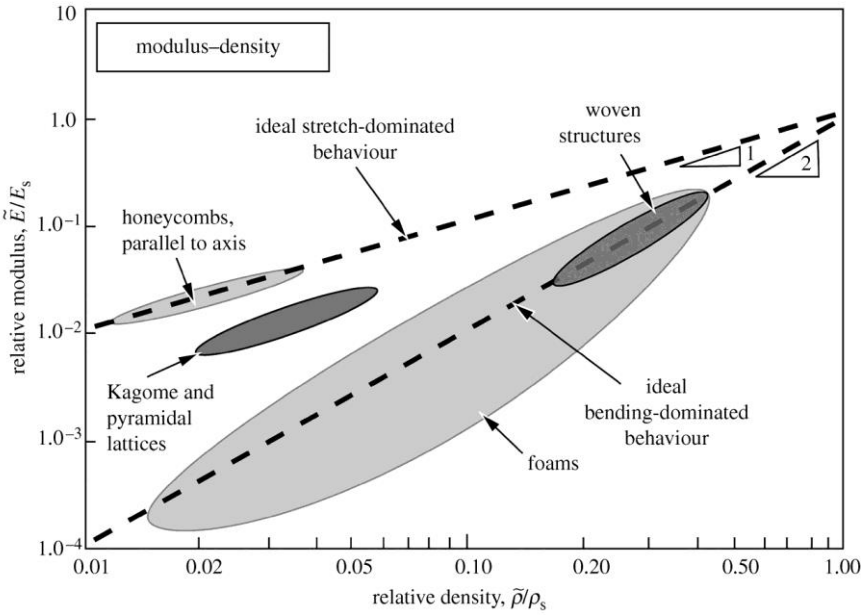

Figure 2.2: Relative modulus versus relative density for lattice structures, including foams. The labeled slopes represent the restrictions based on failure behavior. These boundaries are challenged with AM-based designed lattices [18].

Some foams can achieve a partial grading of density to mitigate high and low energy impacts. Conehead helmets were invented in 2010 by Don Morgan to combine the properties of two types of EPS foam in bicycle and motorcycle helmets [41]. See Figure 2.3 for a cross-section of the graded foam system. EPS foam is one of many types of cushioning found in helmets and is the most common in bicycle and motorcycle helmets. EPS is single-use, cheap to manufacture, and reliable at absorbing an impact. Alternatively,

EPP (expanded polypropylene) foam is multi-use and is more expensive to manufacture [42]. EPP foam – along with stiff vinyl nitrile foam and occasional air bladders – is used in football helmets for its repeated impact properties [43].

Figure 2.3: Conehead EPS foam designed with low density (grey) and high density (white) sections. The functionally-graded approach is like what is easily achievable with additively manufactured designed lattices [41].

Other types of foams also exist for various uses. Expanded polyurethane (EPU) is like EPS in that it crushes on impact. EPU is heavier and more solid than EPS, which raises concerns about head safety for low velocity impact protection [42]. EPU is also not particularly environmentally-friendly so manufacturing is restricted to Taiwan, resulting in a limited supply [44]. Ethylene vinyl acetate (EVA) is commonly used in midsoles of athletic shoes for its energy return, longevity, and flexibility. Brückner et al. examined the feasibility of implementing polyurethane (PU) foam into athletic shoe midsoles in place of normal EVA [45]. The study was performed because PU possesses great long-term stability and impact resistance and is currently only used in some casual shoe midsole designs. Researchers showed that PU foam can be made to closely compare in performance to conventional EVA midsoles. Since the long-term degradation of PU foam is well-documented, it may be a reliable material for use in athletic shoes [45].

2.2 Lattice Design

2.2.1 TPMS and Rod-and-Ball Lattices

There are many lattice designs manufacturable via AM. Research has been performed on both triply periodic minimal surface (TPMS) structures and on conventional rod-and-ball lattice geometries. TPMS structures have very high relative surface areas and porosities [46,47], and exhibit a non-complex functional grading [48] when compared to normal lattices. These types of structures already have many uses in heat exchangers, bodily implants, other biological fields [49–51]. Al-Ketan et al. [4] tested numerous cellular designs, including TPMS structures, and compared them using density, Young's modulus, peak stress, and toughness. The associated designs can be seen in Figure 2.4. Based on the study, the sheet-diamond design exhibited the best overall compression performance because of its high stiffness and toughness – even at low densities.

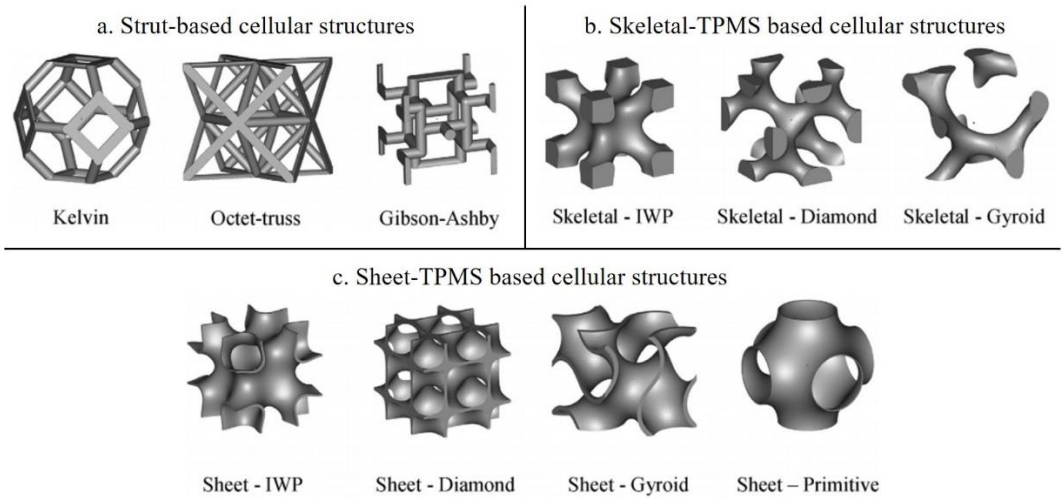

Figure 2.4: Unit cells of various lattice designs [4].

Pictured in Figure 2.5 is the Young's modulus, or stiffness, of various structures at 10% and 25% relative densities (considered relatively low and high, respectively), which shows a substantial difference in performance of the sheet-diamond design versus all the other designs at 10% density [47]. The stiffness of the lattice is almost double that of the next highest design. The sheet-diamond design's stiffness lead over the other lattice models is reduced significantly with increase in density. The Kelvin cell design displays an

increase in stiffness of almost 4 times when the density is increased. These graphs show that the sheet-diamond structure's performance is not as dependent on relative density as the Kelvin cell design. Figure 2.5 also supports the authors' conclusion that sheet-TPMS structures are generally superior to strut-based structures from a performance perspective.

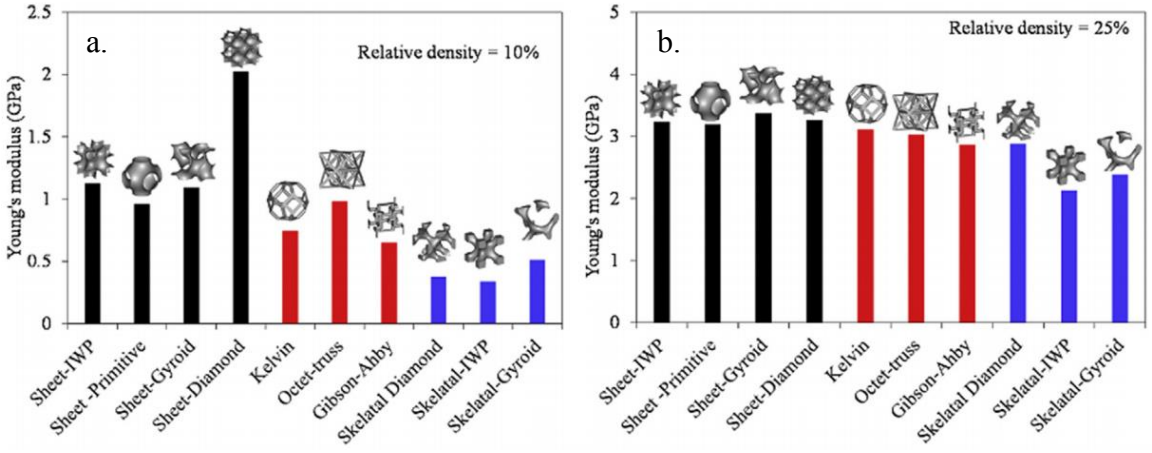

Figure 2.5: Young's modulus for various lattice geometries at (a) 10% relative density (considered to be relatively low), and (b) 25% relative density (considered to be relatively high) [4].

2.2.2 Origami-Derived Lattices

Another type of lattice designs that researchers have analyzed are origami-derived structures [52]. Robinson et al. [53] performed an impact analysis on the Miura-Ori (MO) geometry, which mainly resembles a stacked folded cellular structure. The design was initially used as an efficient method of stacking solar panels for space travel and appears in many natural examples like leaves [54]. An MO lattice was made of elastomeric powder via AM and trimmed to match the size of existing football helmet padding. The lattice design can be seen in Figure 2.6 [53]. In these tests, a 4.7 kg platen was dropped onto the sample from various heights, with data being recorded through a single-axis accelerometer. Tests were performed in succession, with the MO lattice showing superior multi-hit stability when compared with the foam pads; there was 10% rise in peak acceleration for the MO lattice compared with 19-40% rise in peak acceleration with the helmet foam. Overall calculations show that accelerations were reduced by 15% with the MO origami-

based lattice design over the existing foam padding [53]. These are promising results for future AM-based solutions to attenuate multi-hit impact events.

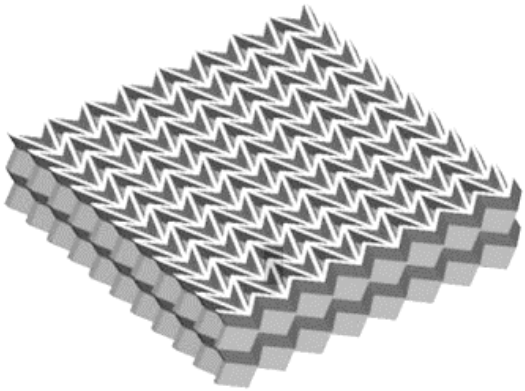

Figure 2.6: Miura-Ori lattice model exhibiting a stacked folded origami-like arrangement [53].

2.2.3 Prism Structures

Prism-based lattices are relatively simple structures constructed out of hollow geometric prisms. Hexagonal prisms, cylinders, rectangular prisms, and triangular prisms have also been tested as lattices. These structures most often do not vary in the z-axis, making them considerably more simplistic than the previously mentioned lattice designs. Some examples can be seen in Figure 2.7 [55].

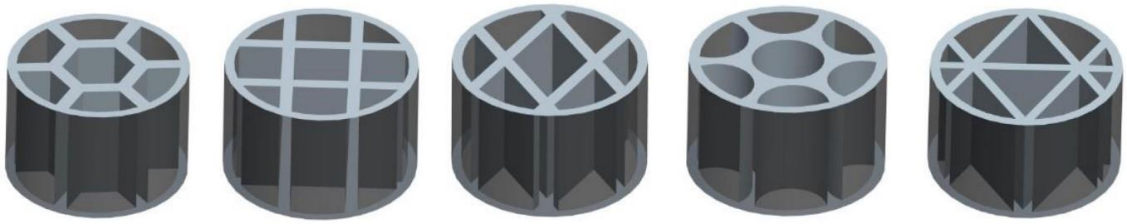

Figure 2.7: Various prism lattice designs. From left to right: hexagonal, square, diamond, circular, triangular [55].

Hexagonal prism-based lattices, also called honeycombs, are a very common simple lattice design. These lattices were used in the Hexr bicycle helmet liner mentioned in section 2.1.1. They protected the wearer's head oriented in an axial direction, which is a

similar approach to that of the popular Purple Grid mattress [56]. Unlike the helmet, however; the Purple Grid is made of a soft rubbery polymer which easily compresses and conforms to a sleeper's body in various positions. The helmet is made of stiffer plastic that is meant to absorb energy in a single-use fashion.

Bates et al. [57] tested TPU honeycomb lattices in a different direction. They studied the effects of functionally grading the lattice by modifying the honeycomb wall thicknesses throughout the part during AM. Their samples were made of NinjaFlex elastomer, which is highlighted in section 2.3.2. These lattices were compressed from the sides of the honeycomb rather than from the top. They then tested the compression and impact performance of three types of honeycomb lattices: uniformly-graded, multiple stage graded, and continuously-graded. Unsurprisingly, the uniformly graded lattice transmitted significant energy after densification, or complete compression. When subjected to lower energy impacts, the non-graded sample performed extremely efficiently, using all the cells to absorb the impact energy; the graded samples have specific regions for various energies resulting in less efficient absorption [57]. Graphs of these various impact energies and gradations can be seen in Figure 2.8.

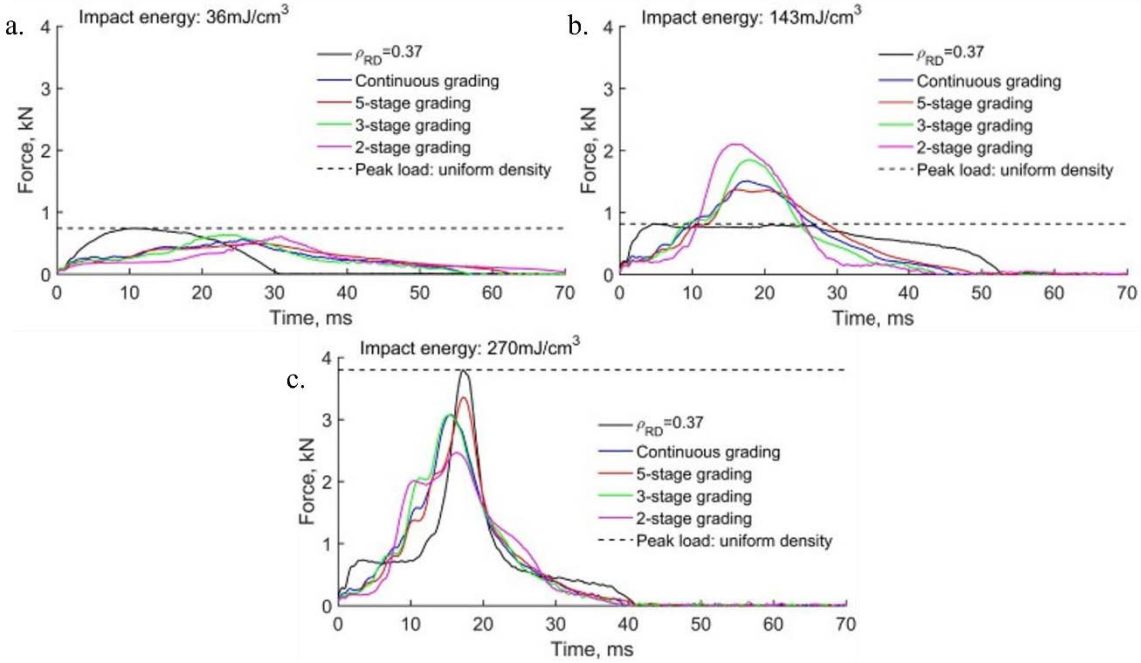

Figure 2.8: Honeycomb lattices subjected to various impact energies. Notice the high efficiency of the uniformly dense sample (black line) in (b). The efficiency is later traded

for increased transmission due to early densification in (c). The functionally-graded honeycombs exhibit a wider working range at the expense of lower efficiency [57].

2.3 Common Elastomers and Flexible Materials

2.3.1 Stratasys Tango Black Plus

Many elastomers are available commercially for various 3D printing methods. One of these printing methods is material jetting (MJ), also called PolyJet by Stratasys [58]. MJ produces extremely accurate and precise parts without the need for post-curing. A wide range of resins are available for use in these MJ printers, with Tango and Tango Black Plus as some of the more common elastomers offered by Stratasys [59]. These materials are thermosets, meaning they cannot be remelted like traditional 3D printed thermoplastics [60]. With Tango Black Plus and a Kelvin cell lattice design, Ge et al. [60] tested the energy absorption performance in a universal testing machine and a vertical drop tower. According to their findings, the Tango Black Plus material was "capable of absorbing close to 100% of the impact energy from the platen drop tests." Full recovery of the 3D printed system was also noted after each impact. The research team concluded that the stickiness of the thermoset elastomer likely contributed to the high energy absorbance ability [60]. A more complete list of the material properties of Tango Black Plus can be seen in Table 2.1 [59].

Table 2.1: Material properties of Stratasys Tango Black Plus elastomer [59].

Property	*Tango Black Plus*
Tensile Strength (MPa)	0.8-1.5
Elongation at Break	170-220%
Shore Hardness	27A
Density (kg/m^3)	1125

2.3.2 NinjaTek NinjaFlex and SemiFlex

There exist quite a few filament options for FFF 3D printers. Considerable variation in material properties can be found with the wide range of flexible filaments available.

Bates et al. [61] tested NinjaFlex and SemiFlex honeycomb lattices in compression situations to analyze the behavior of the materials (the honeycomb design that was tested can be seen in Figure 2.9a). NinjaFlex is a significantly softer material than SemiFlex with an 85A shore hardness rating for the former versus a 98A rating for the latter [62,63]. The honeycomb samples analyzed in the cited research showed a maximum energy absorption efficiency of 0.36, similar to that of most EPU foams. Another interesting finding by the research team was that both materials exhibited a reduction in the specific energy absorption (SEA) after multiple compression cycles. According to Bates et al. [61], the SemiFlex material lost 24.5% of its absorption capability from the first to the second cycle; NinjaFlex performed slightly better, losing 15.3%. Stress-strain curves and the SEA values can be seen in Figure 2.10 for the SemiFlex material over five compression cycles. Also, material properties for both NinjaFlex and SemiFlex can be found in Table 2.2 [64,65].

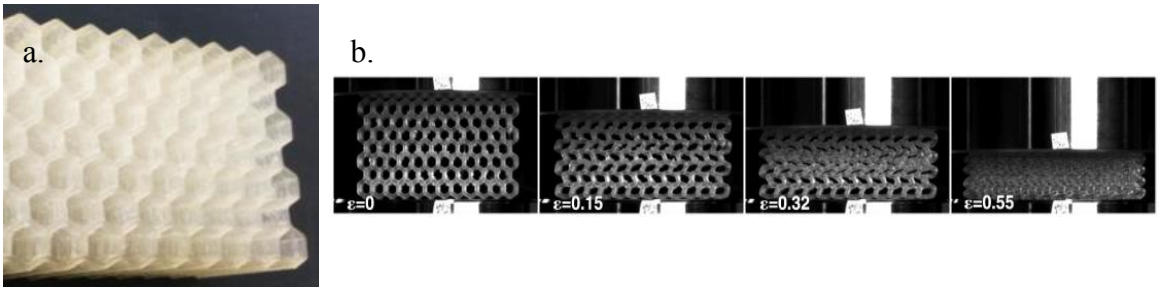

Figure 2.9: Honeycomb lattice printed from SemiFlex. Photo (a) shows a closeup of the cells and (b) shows the compression response at various strains (ε) [61].

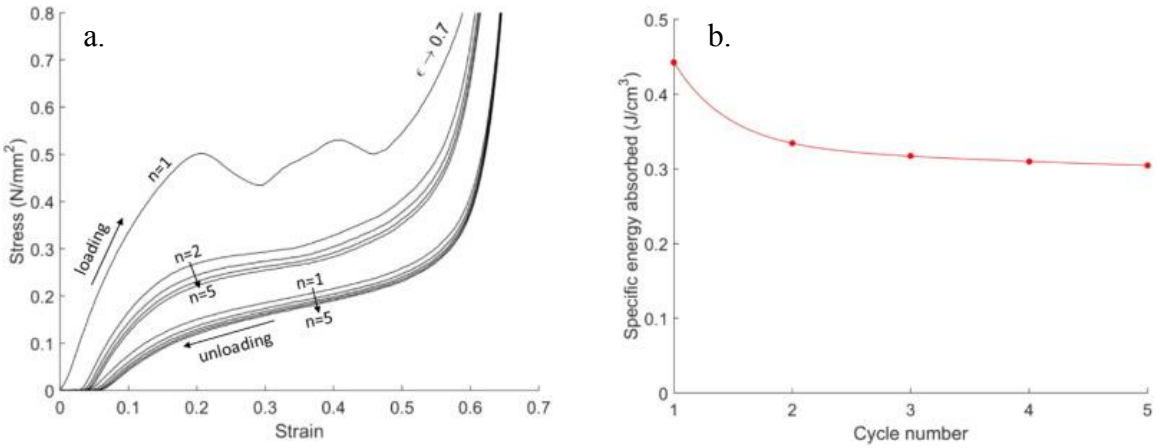

Figure 2.10: (a) Stress-strain curves for five compression cycles, n, for the SemiFlex honeycomb samples with a relative density of 0.34. (b) SEA values for cycles 1-5. Note the decrease in performance as the number of compression cycles increase [61].

Table 2.2: Material properties of NinjaTek NinjaFlex and SemiFlex elastomers [64,65].

Property	*NinjaFlex*	*SemiFlex*
Tensile Strength (MPa)	26	43
Elongation at Break	660%	600%
Shore Hardness	85A	98A
Density (kg/m^3)	1190	1230

2.3.3 Ultimaker TPU 95A

Ultimaker produces a flexible filament for use in its FFF 3D printers called TPU 95A. Named for its high stiffness, TPU 95A holds its shape very well and reversibly deforms only under relatively high velocity impacts. The material's stiffness contributes to its ease of printing when compared to other flexible filaments. Most are soft and stretchy enough to jam up an extruder feed, but TPU 95A stays stiff like ABS [66]. The elastomer exhibits high elongation at break – up to 580%. Ultimaker markets the material as a possible solution to flexible joints and living hinges. More properties can be seen in Table 2.3 [67].

Table 2.3: Material properties of Ultimaker TPU 95A [67].

Property	*Ultimaker TPU 95A*
Tensile Strength (MPa)	39
Elongation at Break	580%
Shore Hardness	95A
Density (kg/m^3)	1220

Researchers have used the flexible TPU 95A filament in applications like simple ventilators. Ahmed et al. [68] additively manufactured a ventilator to combat the shortage due to the COVID-19 pandemic. In their ventilator design, hard plastic was used for attachment points and structural components, while the TPU 95A was used for the balloon, the mouthpiece, and some valves. One of the advantages of manufacturing ventilators via AM is that the sizing can be completely customized for different types of people. Some patients may require larger mouthpieces or balloons. Different sizes of the research team's ventilator design can be seen in Figure 2.11a [68]. The various printed parts for these ventilators can be seen below in Figure 2.11b. The large white part is the balloon, which pumps air into a patient's lungs for breathing assistance. The balloon is flexible to allow for the pumping action to take place. Flexible filaments and materials have many different uses and are easily accessible due to the relatively low cost of FFF AM machines.

Figure 2.11: Ventilator designed by Ahmed et al. [68] in response to the COVID-19 pandemic. Photo (a) shows the different sizing possible with additive manufacturing and (b) shows the 3D printed parts from differently-colored TPU 95A. The large white vessel is the balloon for the pumping of air into a patient's airways.

2.3.4 Carbon FPU 50 and SIL 30

Vat photopolymerization is one additive manufacturing technique that encompasses a broad subset of printing categories. One of these categories is digital light synthesis (DLS). DLS is a method introduced by Carbon to expose resin more continuously to projected light, resulting in isotropic properties, faster production, and smooth surface finishes [69]. A few flexible materials are offered by Carbon: FPU 50 (flexible polyurethane) [70], SIL 30 (silicone) [71], and others. FPU 50 is a flexible and durable plastic that performs well in repeated bending situations. Its elongation at break approaches 300%, which is significantly more than most flexible materials on the market [72,73]. More material properties can be seen in Table 2.4 [72]. Using a material like FPU 50 in a repeated

impact situation may allow for more long-term performance than other elastomers which tend to wear down and break during bending cycles of lattice struts.

SIL 30 is another interesting elastomer offered for DLS. In its green state (prior to curing), the part is stiff. The stiffness allows for more complex designs to be manufactured. Most flexible resins print flexible, meaning they may move or shift when not anchored properly. Since SIL 30 does not require extra support due its solid printing properties, designs can be made considerably more complex and consistent [71,74]. As shown in Table 2.4, SIL 30's elongation at break is 350%, which is extremely high and useful for applications like lattices and complex engineered structures. SIL 30 is also cited as being biocompatible; comfort is increased when in contact with skin like in various wearables. Carbon [74] claims that biocompatibility, along with flexibility and durability, lends well to uses in "headphones, wristbands, and various attachments in wearables." A specific application, as demonstrated by Imbrie-Moore et al. [75], was to rapidly develop and manufacture customizable N95 mask silicone seals in response to the COVID-19 pandemic. The SIL 30 elastomer was used to seal the N95 filter effectively and comfortably against the face as demonstrated in Figure 2.12 [75]. Many diverse applications exist for SIL 30.

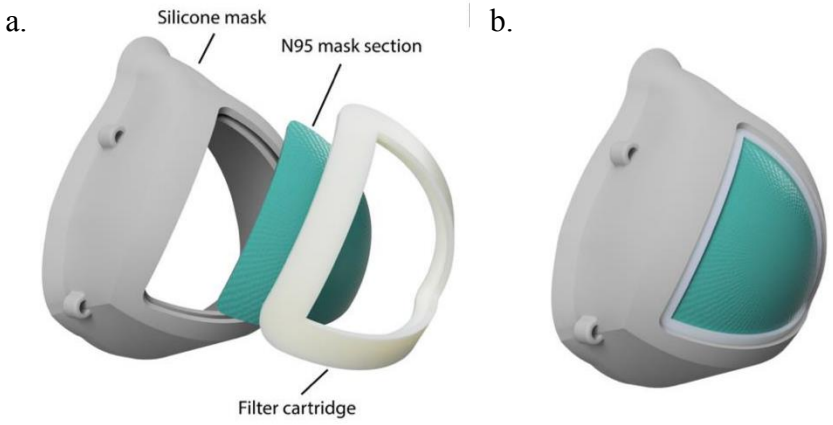

Figure 2.12: Application of SIL 30 additively manufacturable silicone. (a) Exploded view of COVID-19 customizable N95 mask with silicone seal and (b) assembled mask [75].

Table 2.4: Material properties of Carbon FPU 50 and SIL 30 flexible plastics [72,74].

Property	*FPU 50*	*SIL 30*
Tensile Strength (MPa)	25	3.5
Elongation at Break	200%	350%
Shore Hardness	71D	35A
Density (kg/m^3)	1050	1070

2.3.5 FormLabs Rebound, Flexible 80A, and Elastic 50A

The vat photopolymerization 3D printing category also includes SLA as mentioned in section 1.3.1. FormLabs is an AM company that produces SLA printers and resins. Included in their lineup are three flexible materials: Rebound, Flexible 80A, and Elastic 50A. Rebound is a proprietary material made in partnership with New Balance for their running shoes and is currently inaccessible to consumers. Rebound possesses 300% elongation at break and 86A hardness, making it fairly stiff [76]. Material properties are shown in Table 2.5. The New Balance shoes that use Rebound exhibit 57% energy return from the lattice midsole [77]. Figure 2.13 shows these shoes with the sections of Rebound in the midsole for customized impact absorption.

Figure 2.13: New Balance shoes made with FormLabs Rebound resin-based lattices [78]. Athletic footwear is a common application of 3D printed lattices.

FormLabs also produces Flexible 80A and Elastic 50A materials for their SLA printers for consumer use. Flexible 80A is marketed as the stiffer elastomer between the two with a Shore hardness of 80A. Elastic is much more pliable, with a Shore hardness of 50A. Flexible 80A has an elongation at break of 120% compared to 160% for the Elastic 50A material [79,80]. Elongation at break is important to monitor when selecting the proper material because small pieces may tend to break rather than stretch with low elongation abilities. More material properties for these elastomers are listed in Table 2.5. Based on these properties, it would seem that Rebound would perform better in a lattice configuration than the other two, due to its elongation ability and ultimate tensile strength.

Table 2.5: Material properties for FormLabs Rebound, Flexible 80A, and Elastic 50A elastomers [76,79,80].

Property	*Rebound*	*Flexible 80A*	*Elastic 50A*
Tensile Strength (MPa)	22	8.9	3.23
Elongation at Break	300%	120%	160%
Shore Hardness	86A	80A	50A

2.3.6 EOS TPE 300, TPU 1301, and PA 11

SLS additive manufacturing is a more expensive technique than FFF or VPP with very fine resolution capabilities. EOS, a company involved in SLS printing, is credited with the invention of Digital Foam – lattice structures generated out of their powdered material [81]. With Digital Foam, designers and researchers can functionally-grade different parts of objects to be denser and more supported than others. The company has reportedly seen a sizable increase in users of Digital Foam for applications like footwear and headwear [82]. A helmet liner made with the patented Digital Foam is shown in Figure 2.14 [83]. EOS produces TPE 300 and TPU 1301, both of which are soft-touch, white elastomers. TPE 300 has an in-plane elongation at break of 267%, with TPU 1301 at 250%. A larger difference is seen in elongation at break in the print direction (z-axis), which is 180% for TPE 300 and 90% for TPU 1301; more of these materials' properties are listed

in Table 2.6 [84,85]. Based on both elongation at break and ultimate tensile strength, TPE 300 exhibits superior properties for lattice construction and longevity.

Figure 2.14: EOS Digital Foam helmet liner. Digital Foam technology allows for mass customization of protective foam products [83].

EOS also produces Polyamide 11 (PA 11), which is a flexible polymer with high material strength and impact resistance. Bicycle helmets by Hexr were discussed previously in section 2.1.1 which use PA 11. Its elongation at break is 45%, making it useful for high energy, single-event impacts [86]. More properties are included in Table 2.6 [87]. The material is partially made from castor oil, making it more environmentally-friendly than most conventional hard foams. The design of a latticed part coupled with the strong material make for a lightweight and effective heat-dissipative system [88]. Another possible application for the PA 11 material is in shin guards for soccer. The breathable design keeps an athlete cool while protecting their legs from high energy impacts [89]. See Figure 2.15 for the shin guard design studied by EOS.

Figure 2.15: Shin guard designed by EOS with PA 11 material [86,89]. The lattice design allows for increased air circulation, while effectively protecting the shins.

Table 2.6: Material properties for EOS TPE 300, TPU 1301, and PA 11 flexible plastics [84,85,87].

Property	*TPE 300*	*TPU 1301*	*PA 11*
Tensile Strength (MPa)	15-20	5-7	48
Elongation at Break	180-267%	90-250%	28-45%
Shore Hardness	88A	86A	75D
Density (kg/m^3)	1042†	1110	990

†Based on in-lab experimental testing.

2.4 Flexible Sensors

Sensors have been developed by multiple researchers around the world with the goal of improving comfort and sensing ability near skin. Flexible pressure sensors are created using a few different approaches. Wang et al. [90] have examined a type of device called a resistive fabric strain sensor (FSS). A sensing layer combined with polydimethylsiloxane (PDMS) composite elastomers forms a robust sensor design capable of handling significant strain levels (see Figure 2.16) [90,91].

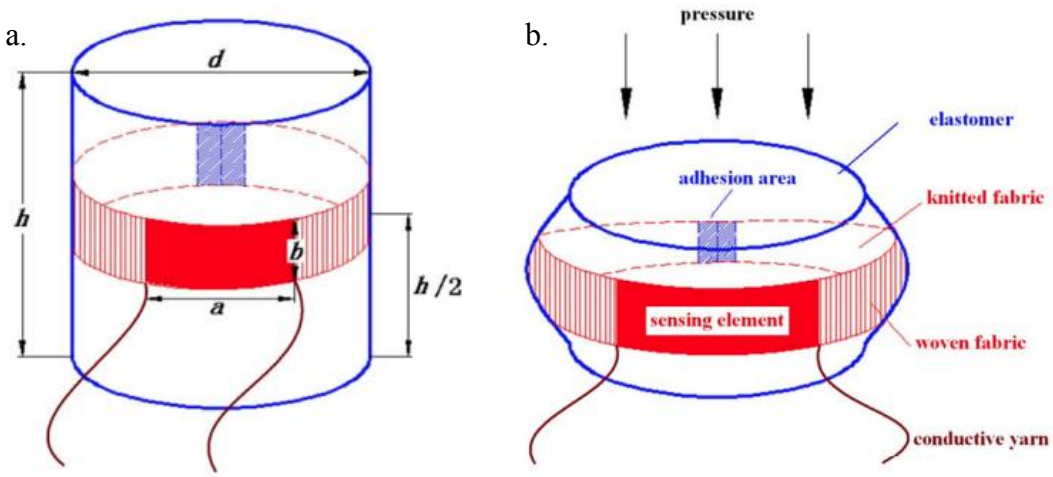

Figure 2.16: Flexible sensor design consisting of PDMS elastomer and fabric strain sensor (a) in its initial state, and (b) under impact [90].

Another approach to the creation of flexible impact sensors uses a flexible mechanoluminescence (ML) film made from mixing $SrAl_2O_4$:Eu,Dy and PDMS [92]. $SrAl_2O_4$:Eu,Dy refers to strontium monoaluminate doped with europium and dysprosium, which forms a phosphorescent material [93]. Piyush Jha and Ayush Khare performed impact testing with a steel ball on the ML sensor. The intensity of the light emission increased "linearly with the square of the impact velocity of the steel ball" [92]. Jha and Khare also found that repeated impacts did decay the ML response over time. The ability to generate impact data from light emission is an interesting development and could be useful in dark locations like packaging or inside protective equipment.

The type of sensor used in this research was made from an ionic liquid (IL) layer with embedded CNTs surrounded by a flexible plastic shell [33]. A diagram of the sensor can be seen in Figure 2.17. The taxel (or "tactile pixel" where CNT traces overlap) outputs a change in voltage which can be translated to force via experimental scaling. As outlined in section 1.4, IL-based flexible sensors can accurately measure low and high velocity impacts. These types of sensors have been used in a variety of circumstances including inside tires for pressure analysis and inside shoe midsoles [94,95].

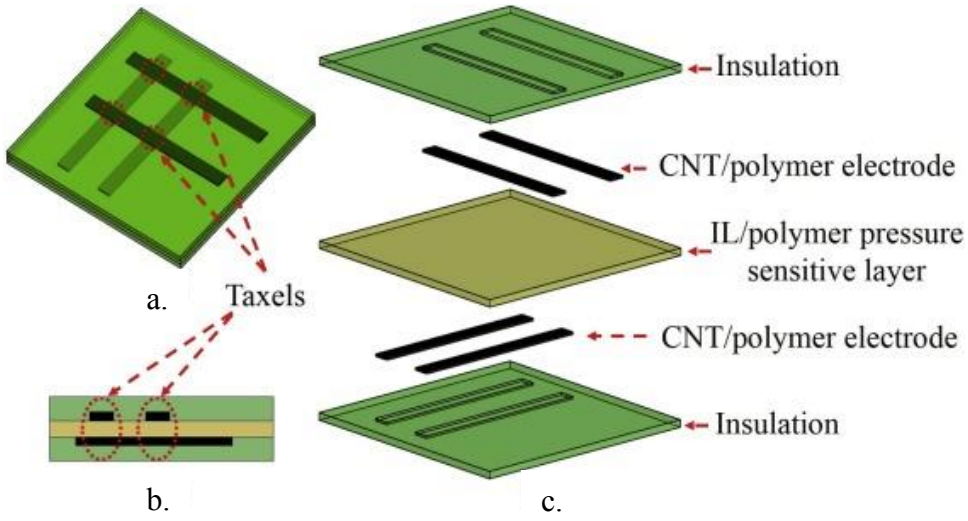

Figure 2.17: Flexible sensor design using IL layer and CNT traces showing (a) 3D model, (b) side view of sensor, and (c) layer-by-layer construction of sensor [33].

2.5 Head and Helmet Safety

Head injuries can occur with nearly any physical sport or impact. Researchers increasingly agree that off-axis impacts cause more damage long-term than straight on impacts to the head. Oblique impacts result in large shear forces inside the brain, which according to Aare et al. [96], "has been proposed as a cause of traumatic brain injuries like diffuse axonal injuries (DAI)." DAI results from rapid deformation of axons in the brain which cause them to become brittle rather than flexible. Eventually, the damage to axons disconnects them and hinders neuron interaction [97]. Current helmet requirements and head injury measuring techniques do not properly account for any sort of rotational acceleration [98]. According to Fernandes et al. [98], these testing requirements consist of peak translational acceleration and HIC.

The Head Injury Criterion (HIC), defined in 1972 by NHTSA, is a measure of head injury based on the translational acceleration experienced by crash test dummies and can be seen in Equation 1 [98–100]. The relatively simple HIC metric produces a number without any significant injury-related meaning. NHTSA designated certain thresholds for various dummy sizes in 2000 [101]; however, the dummies used during testing do not exhibit properties that simulate a head impact accurately. According to Brian G. McHenry

[99], "the head structure for the whole dummy family . . . is essentially a padded rigid aluminum shell that does not deform as the human skull does deform under loading."

$$HIC = \left(\left[\frac{1}{t_2 - t_1} \int_{t_1}^{t_2} a(t)dt \right]^{2.5} (t_2 - t_1) \right)_{max} \quad (1)$$

Another similar metric used to determine the severity of head impacts is the Head Impact Power (HIP), which was proposed by Newman et al. [102] for football impacts. The HIP calculation treats the head as a "one-mass structure" and is therefore limited in its prediction of certain neurological injuries [103]. The equation used to compute HIP is shown in Equation 2, where $C_{1\text{-}3}$ coefficients are mass of a 50th percentile human head (4.5 kg), $C_{4\text{-}6}$ coefficients are moments of inertia for a human head, $a_{x\text{-}z}$ are linear accelerations, and $\alpha_{x\text{-}z}$ are angular accelerations [103]. Therefore, the HIP metric does account for oblique accelerations unlike the previously mentioned HIC.

$$HIP = C_1 a_x \int a_x dt + C_2 a_y \int a_y dt + C_3 a_z \int a_z dt + C_4 \alpha_x \int \alpha_x dt + C_5 \alpha_y \int \alpha_y dt + C_6 \alpha_z \int \alpha_z dt \quad (2)$$

According to Marjoux et al. [103], "HIP was designed only for brain injury and not for [subdural hematoma] or skull fracture." These types of injuries are much rarer in football impacts than in automobile accidents. In fact, out of all the injuries examined by Marjoux et al. [103], all skull fractures occurred in pedestrians who would not be wearing helmets. Also, only one subdural hematoma was recorded for a motorcyclist accident and none for football impacts. HIP is similar to the Viscous Criterion, proposed by Lau et al. [104]. The Viscous Criterion establishes a probability of injury given compression and rate of compression of a viscous organ [99]. Due to the rotational acceleration component and the increased attention given to oblique impacts and their severity in sports, the HIP calculation more accurately predicts the probability of injury to sports players than the more basic HIC.

Even more accurate than these models is the Louis Pasteur University finite element head model (ULP FEHM) [103,105]. The ULP computer simulation model takes into account items like skull deformation, skin, face, and brain matter in its impact and injury calculations. These features and the overall model produces the most accurate predictor of injury based on comparisons performed by Marjoux et al. [103]. Based on their comparisons, it was determined that the HIC and HIP calculations were not able to correctly account for intracranial movement. More research is needed for better methods of predicting injury severity in head impacts. FEA models open the door to a complex method of solving and testing new helmet designs that protect against linear and rotational accelerations properly. By using these computer simulations, helmet designers and manufacturers can engineer head protection to increase safety and rapidly test new designs with additive manufacturing.

3.0 Experimental Methodology

In this research, five elastomeric materials were manufactured into Kelvin cell lattices for low velocity impact testing and quasi-static compression testing. Testing of the lattices was completed in two phases; the first phase consisted of two materials and two types of functional grading, and the second phase consisted of three materials and three types of functional grading. Both testing divisions included a hybrid setup with two combined materials, which explored versatile designs. Also, an industry-standard helmet shell made of polycarbonate was used with a modified impact tower to test the performance of the best lattices in application. Finally, the performance of a flexible sensor provided by the University of Akron was evaluated to determine the feasibility of its application to contact sports helmets. A small flexible IL-based pressure sensor was enveloped by an Elastic 50A lattice during printing in a Form 2 SLA machine.

3.1 Materials and Methods

Five elastomers were tested and consisted of 2 resin-based materials, 2 filament-based materials, and 1 powder-based material. FormLabs Rebound and Carbon SIL 30 were used as the two resin-based elastomers; these are shown in Figure 3.1. Rebound was additively manufactured on a FormLabs SLA printer with default settings and normal conditions [76]. Rebound is a black elastomer with high stiffness. SIL 30 was processed with a Carbon printer that employs their proprietary Digital Light Synthesis (DLS) [74]. The DLS method projects light from underneath the resin in a similar way to that of the SLA manufacturing method. SIL 30 is very compliant and soft. These materials are opposite stiffnesses and both are classified under the VPP additive manufacturing umbrella.

a. b.

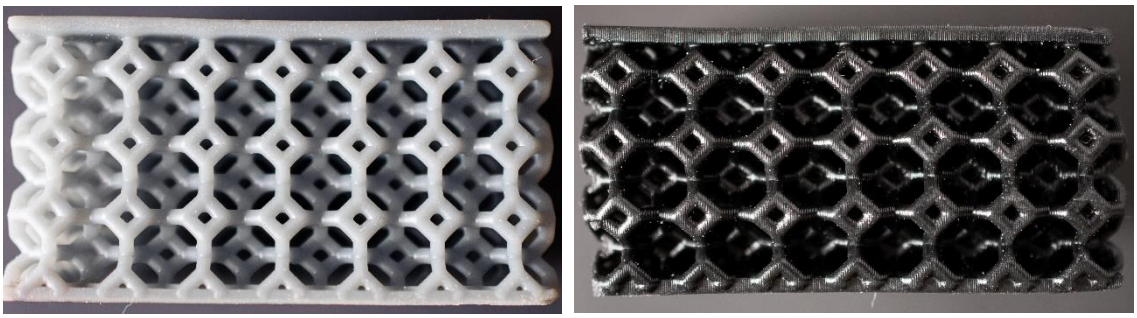

Figure 3.1: Non-graded samples of (a) Carbon SIL 30 and (b) FormLabs Rebound.

The two filament-based materials used were NinjaTek NinjaFlex and Ultimaker TPU 95A, shown in Figure 3.2. NinjaFlex filament was manufactured on a FFF 3D printer and is relatively soft when compared with TPU 95A [62]. TPU 95A was processed on an Ultimaker 3 Extended FFF printer with a 0.4 mm (type AA) nozzle. TPU 95A was printed with a Bowden-tube feed design with adjusted print speed, no retraction, bridging and coasting settings on, and a reduced fan speed [67]. TPU 95A is very stiff and resides on the highest end of the Young's modulus spectrum of tested materials. The non-graded lattice had a Young's modulus of 2.168 MPa, which is almost 400% greater than the stiffness of the equivalent NinjaFlex lattice (0.557 MPa).

a. b.

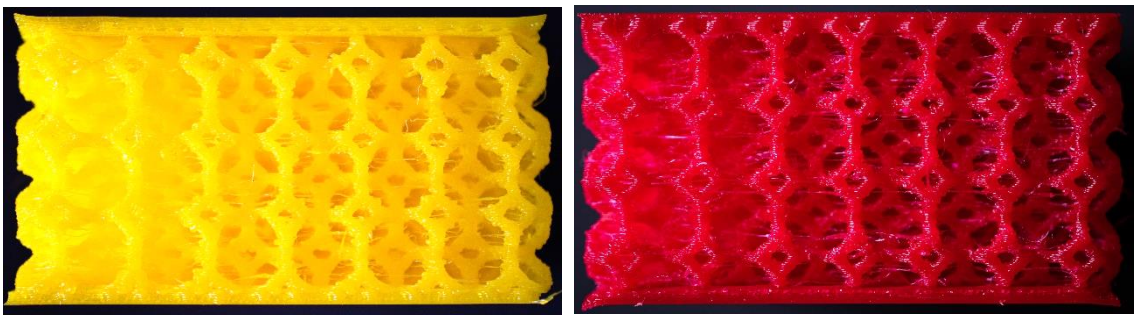

Figure 3.2: Non-graded samples of (a) NinjaTek NinjaFlex and (b) Ultimaker TPU 95A.

The last material tested was EOS TPE 300 powder, which was processed with an EOS P 770 SLS printer. These lattices were produced at EOS with default laser settings in an x-y orientation. Post-processing of these parts included manual depowdering. TPE 300

is soft to the touch and has mid-range stiffness properties [84]. TPE 300 displayed good performance during the various tests with little to no degradation. More material specifications are given in Table 3.1, and structural stiffness ranges are compared in Figure 3.4.

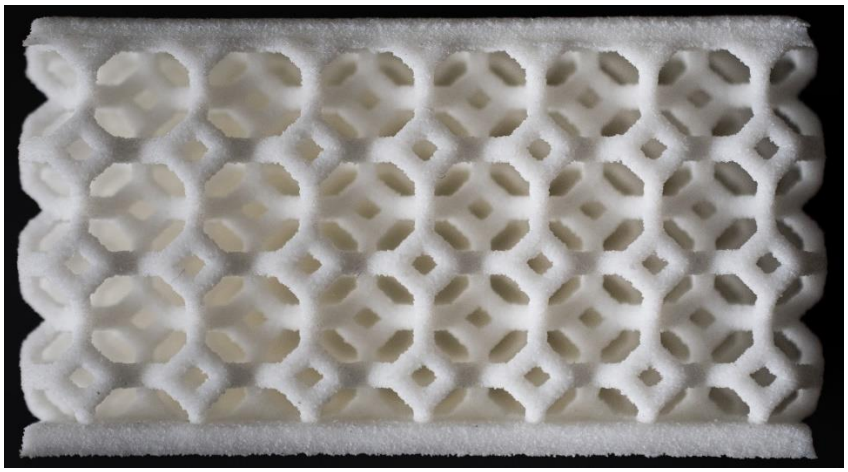

Figure 3.3: Non-graded sample of EOS TPE 300.

Table 3.1: Elastomeric thermoplastic material physical properties.

Material	*AM Process*	*Material Density* kg/m^3	*Structural Stiffness MPa*	*Shore Hardness*
Carbon SIL 30	SLA	1070	0.018-0.144	35A
EOS TPE 300	SLS	1042	0.634-0.858	88A
FormLabs Rebound	SLA	984	0.823-1.212	86A
NinjaTek NinjaFlex	FFF	1187	0.110-0.557	85A
Ultimaker TPU	FFF	1220	0.998-2.168	95A
FormLabs Elastic 50A[†]	SLA	—	—	50A
FormLabs Flexible 80A[†]	SLA	—	—	80A

[†]Material density and structural stiffnesses for these materials were not tested.

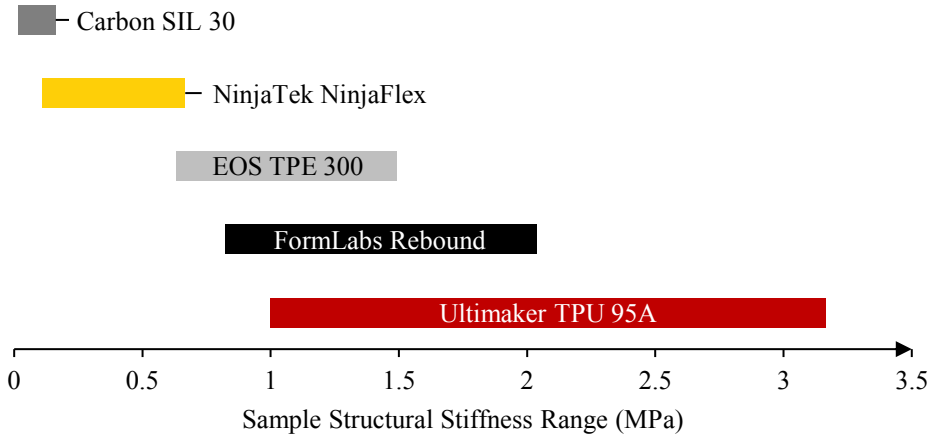

Figure 3.4: Comparison of range of elastic Young's modulus values for various samples and materials.

Three types of functional grading were explored in this research. Non-graded lattices consisted of a uniform strut thickness throughout the entire lattice sample. Vertically-graded models exhibited normal thickness toward the top of the lattice and 50% thinner struts toward the bottom; the gradient is smoothly modeled in programs like nTopology and Mithril by Siemens. Finally, side-graded specimens were generated in a similar way to vertically-graded except the gradient is from side-to-side rather than top-to-bottom. All types of the functional grading tested can be seen in Figure 1.3.

3.2 Quasi-Static Compression Testing

Compression testing of the various lattice samples was completed on an Instron 4206 universal testing machine. The machine was outfitted with a fixed bottom platen and self-aligning top platen to compensate for stiffness irregularities. The top platen became slightly angled when testing the side-graded lattices, as one side is much stiffer than the other. The 12° angle found during compression testing was used in the design of the low velocity impact testing of the side-graded samples. Data obtained during quasi-static, or extremely slow, compression testing consisted of extension in millimeters and load in Newtons. For the lattice compressions, an extension rate of 2 mm/min was used. By processing the raw data in Excel with the surface area in contact with the compression platens, stress and strain

can be produced for each lattice setup. From the stress-strain curve, elastic Young's modulus and absorbed energy can be calculated for each sample. The elastic Young's modulus is shown by the slope of the "plateau" found in a stress-strain curve of elastomeric material [4]. Also, the absorbed energy has been shown to be the area under the curve with bounds at zero and the densification point; as illustrated by equation 3 [17]. Both of these features are shown below in Figure 3.5. In the following example, the Young's modulus is 0.858 MPa and the absorbed energy is 2.96 J.

$$e = \int_0^{\varepsilon} \sigma(\varepsilon) d\varepsilon \qquad 3$$

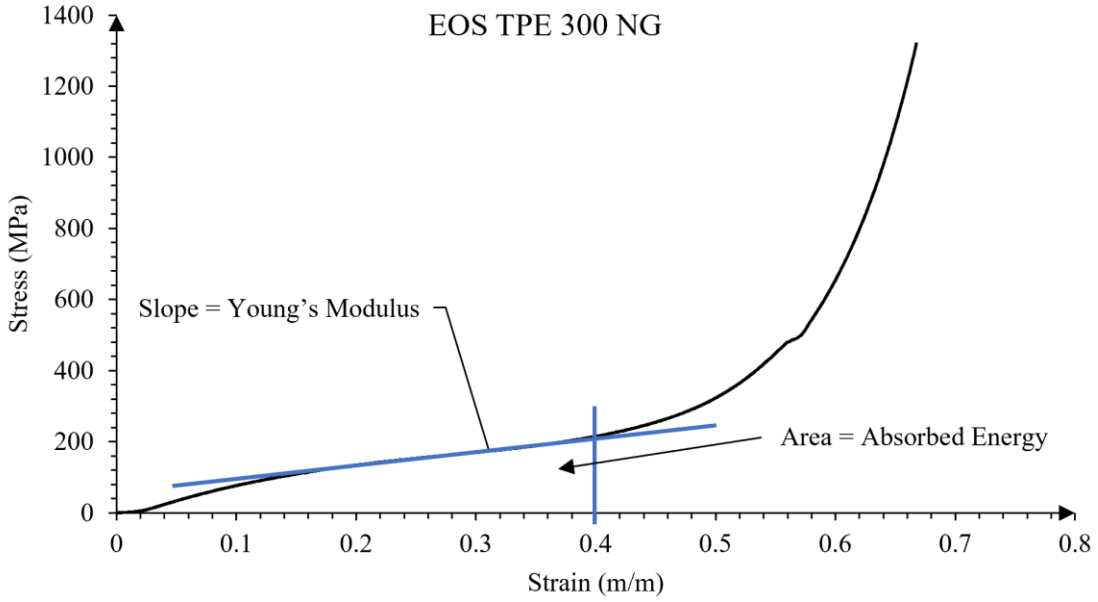

Figure 3.5: Stress versus strain curve for non-graded (NG) EOS TPE 300 lattice during quasi-static compression. Features listed are the elastic Young's modulus and absorbed energy.

3.3 Low Velocity Impact Testing

Dynamic performance of the samples was tested using a custom-built vertical impact tower. The tower consisted of two steel poles with linear ball bearings mounted to a wooden board which supported the load cell and upper steel platen. A fixed lower platen was

mounted to the floor of the impact tower structure and was used to hold each sample during testing. A model of the impact setup can be seen in Figure 3.6. Connected to the load cell were both a Type 5018A Kistler charge amplifier and a GW Instek GDS-1074B Oscilloscope. An Olympus i-Speed 3 high-speed camera and video light were also used to capture each impact in slow motion (10,000 frames per second). With the shown setup, multiple variables were gathered: force (newtons), time (seconds), and displacement (millimeters).

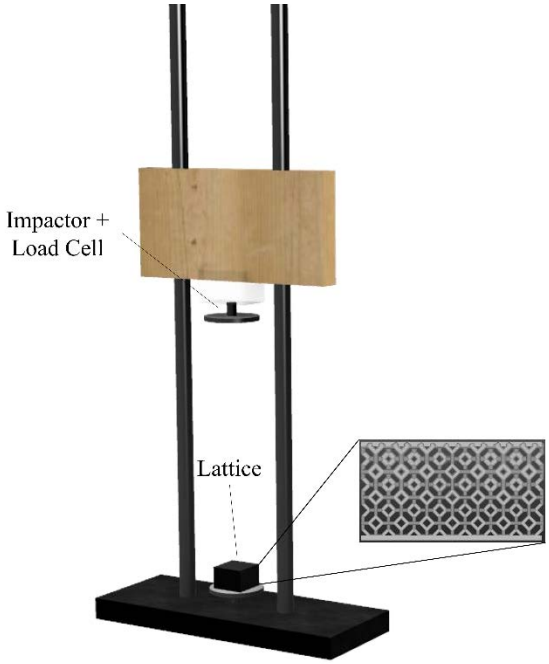

Figure 3.6: Vertical impact tower setup containing impactor with load cell, fixed bottom platen with sample, and vertical columns for linear ball bearings.

3.3.1 Lattice Testing

Initially, individual lattice samples were tested in the low velocity impact tower. The wooden board suspending the load cell combined with the upper platen and linear bearings weighed 4.66 kg, which closely resembled the weight of a human head [106]. For side-graded lattices only, the bottom platen was not horizontal; instead, it was fixed at an angle of 12° to simulate an oblique impact rather than a head-on collision. The 12° position was experimentally derived as the resultant average incline of the self-aligning

compression platen in the Instron universal testing machine. Because of the different testing method, it is difficult to compare raw results between the side-graded lattices and the two other types of lattices.

3.3.2 Helmet System Testing

In addition to the normal lattice testing, a full-scale helmet setup was analyzed. The impact tower was modified to conform to a larger impact system consisting of a polyester sphere (acts as the "head" for a helmet shell and lattice padding) mounted to the linear bearings via a polycarbonate beam. The new setup weighed 15.9 kg, which matched the testing weight set by the NFL helmet testing protocol [107]. The load cell was placed underneath the bottom platen to track the impact in a similar way as before. Also, the oscilloscope, charge amplifier, and camera system remained the same to gather identical variables. Due to the increased weight over the previous impactor, significantly more impact energy was induced here than in the previous single lattice tests. The helmet impact testing apparatus is shown below in Figure 3.7.

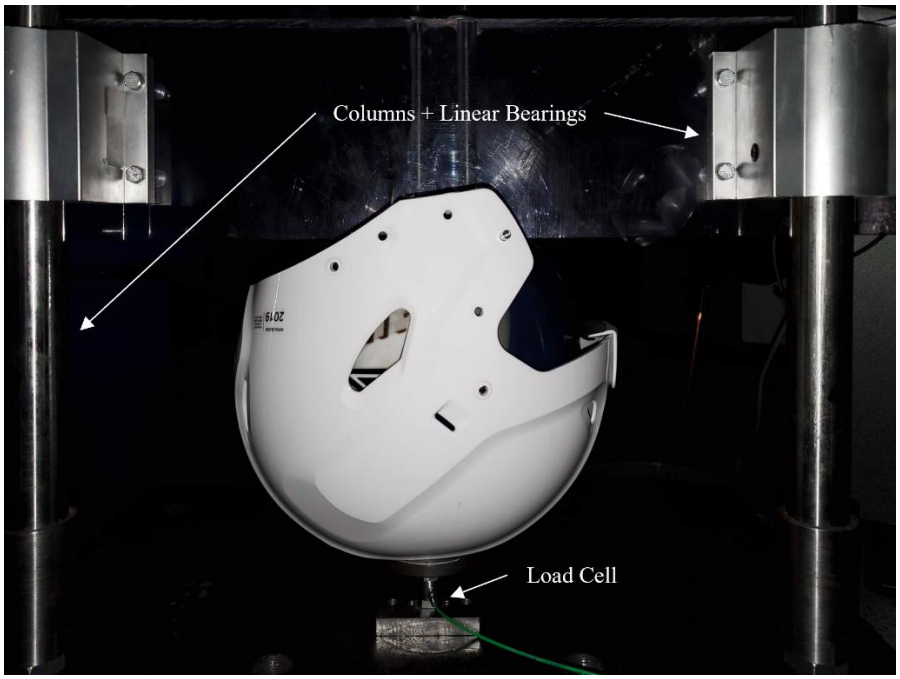

Figure 3.7: Helmet impact setup including vertical columns, linear ball bearings, and the modified load cell position. For the impacts, lattices are contained inside a polycarbonate helmet shell to act as padding.

3.3.3 Data Analysis and Processing

Data collected from each low velocity impact consisted of voltage, displacement, and time. Voltage was converted to force using conversion factors given by the amplifier. Computer programs like Microsoft Excel, Tracker, and Origin 2020 assisted in the processing of data. First, Tracker generated position-time data from the high-speed video footage. Using Microsoft Excel, all variables were combined to yield force-displacement graphs for each sample. These curves were integrated with Origin 2020 to find the enclosed area prior to densification of the sample, known as absorbed impact energy. Also, Origin 2020 was used to differentiate the position data, yielding velocity and acceleration information.

3.4 Side-Graded Lattice Modeling

Side-graded lattices were designed to effectively mitigate angled, or oblique impacts instead of direct linear hits. Due to the previously mentioned differing test method used to analyze the side-graded lattice performance, it was difficult to compare side-graded samples to non- and vertically-graded samples. Thus, finite element analysis (FEA) modeling was employed by José Angel Diosdado-De la Peña of the Materials Science department at Youngstown State University to bridge the gap in data. Material properties were gathered from tensile testing of EOS TPE 300 samples according to ASTM D638 [108]. TPE 300 was elongated over 300% of its original length before breaking. The average stress-strain curve from the testing of five samples is shown in Figure 3.8.

Further curve fitting and modification was necessary to correctly model the properties of TPE 300 in ANSYS Mechanical software. HYPERFIT 2.181 was utilized to perform the curve fitting by isolating certain parameters based on the behavior of rubber-like materials. The common predictors of properties for rubber materials consist of the Arruba-Boyce, Ogden 3rd order, Mooney-Rivlin, Neo-Hooke, and Yeoh material models [109]. The various models are optimized to fit specific types of rubber-like property curves For example, the Mooney-Rivlin model was created for natural rubber up to 100% tensile strain [110]. Also, the Ogden 3rd order model was designed for carbon-black reinforced rubber up to 600% strain [111,112]. Based on research by numerous material scientists, the

Ogden 3rd order material model is a good all-around model when only tensile data is available [113–115]. Thus, the stress-strain curve in Figure 3.8 was converted to Ogden 3rd order parameters displayed in Table 3.2 and fitted to the curve shown in Figure 3.9.

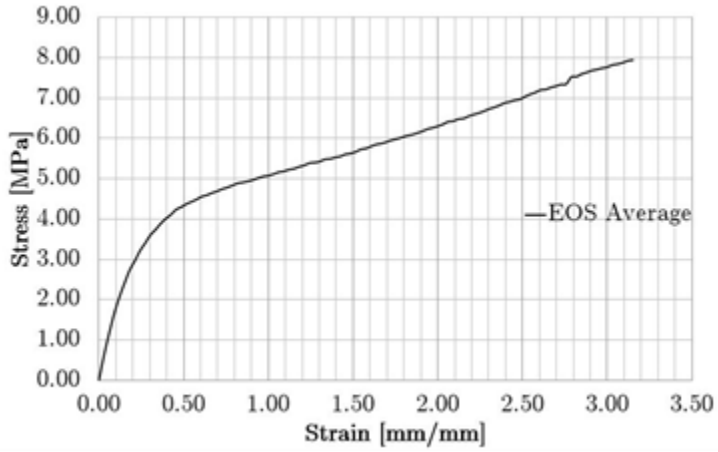

Figure 3.8: Average stress-strain curve of five tensile tests of EOS TPE 300 samples. Over 300% elongation at break is observed in these results.

Table 3.2: Ogden 3rd order material model parameters based on the average tensile test data of EOS TPE 300.

Parameter	*Value*	*Unit*
λ_1	2.502	MPa
α_1	-0.463	-
λ_2	-14.542	MPa
α_2	-2.237	-
λ_3	-158.713	MPa
α_3	0.103	-

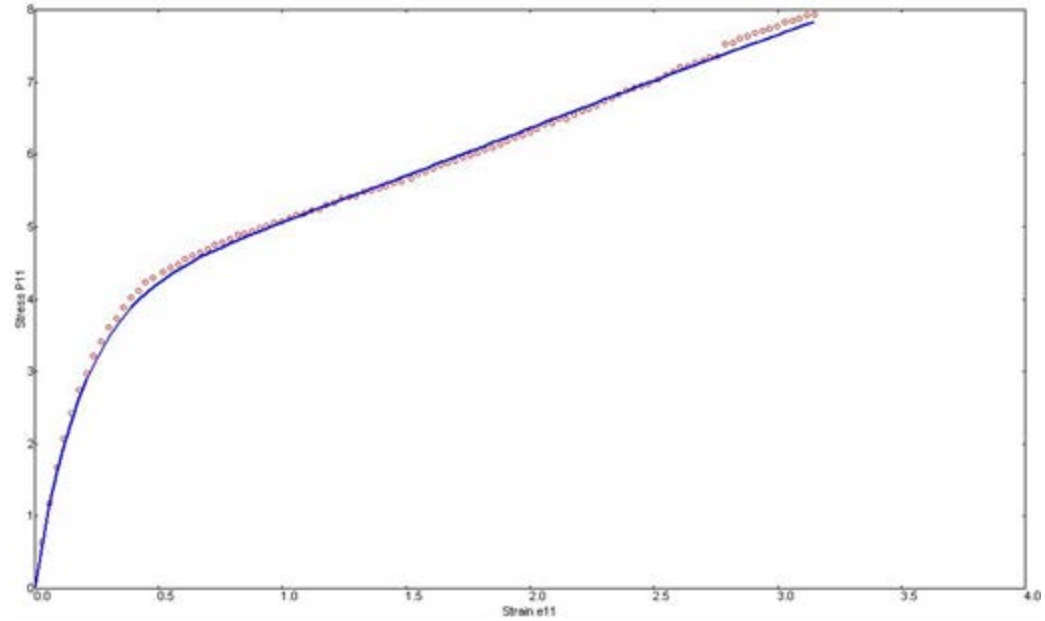

Figure 3.9: Final stress-strain curve for TPE 300 fitted with HYPERFIT 2.181 and Ogden 3rd order parameters. The curve was used for modeling the material properties of the TPE 300 elastomer.

After the initial material tensile data was found, FEA software was able to utilize the properties to create a baseline behavior. Once the lattice model was loaded into ANSYS, impact results could be obtained for various trials that were not performed in the actual low velocity impact testing. Material modifications did need to be made due to the effects of TPU load softening [116–124] and strain-rate hardening [118,125,126]. New Ogden 3rd order material model parameters were calculated based on work performed by Andena et al. [127], Shepherd et al. [128], and Smith & Duris [129]. These modified parameters are displayed in Table 3.3.

Table 3.3: Updated Ogden 3rd order model parameters with inclusion of load softening and strain-rate hardening.

Parameter	*Quasi-Static*	*Impact*	*Unit*
λ_1	1.904	3.929	MPa
α_1	-0.151	0.113	-
λ_2	-12.342	-11.520	MPa
α_2	-2.060	-2.236	-
λ_3	189.499	-101.145	MPa
α_3	-0.080	0.144	-

3.5 Lattice Sensor Testing

The sensors used in this research were provided by the University of Akron's Mechanical Engineering department for evaluation inside elastomeric lattice structures. A Texas Instruments CC2650 microcontroller equipped with a Bluetooth module was used to send data from the sensor to a cell phone and computer. Impacts were sensed from remote access points and data was collected in real-time. The IL-silicone sensor pad was integrated inside a lattice during printing to seamlessly envelop the sensing device without adhesives, which promotes increased robustness and flexibility of the entire unit [130]. To enclose the sensor completely, a modified Kelvin cell lattice was designed in nTopology with a sensor sized (30 x 30 mm) cavity and wiring holes. The flexible sensor was outfitted with solid-core wires connected to the ends of CNT traces which fit snugly through the designed holes. Elastic 50A was printed in a FormLabs Form 2 SLA printer. The model was allowed to progress to the completion of the cavity and then paused. The flexible sensor was then inserted into the cavity with signal wires being pushed through the holes. Printing continued until the lattice was complete and the sensor was then fully enclosed, with wiring protruding from all sides. Figure 3.10a shows the lattice at half-completion with the embedded sensor, and Figure 3.10b shows the full lattice with encapsulated wiring.

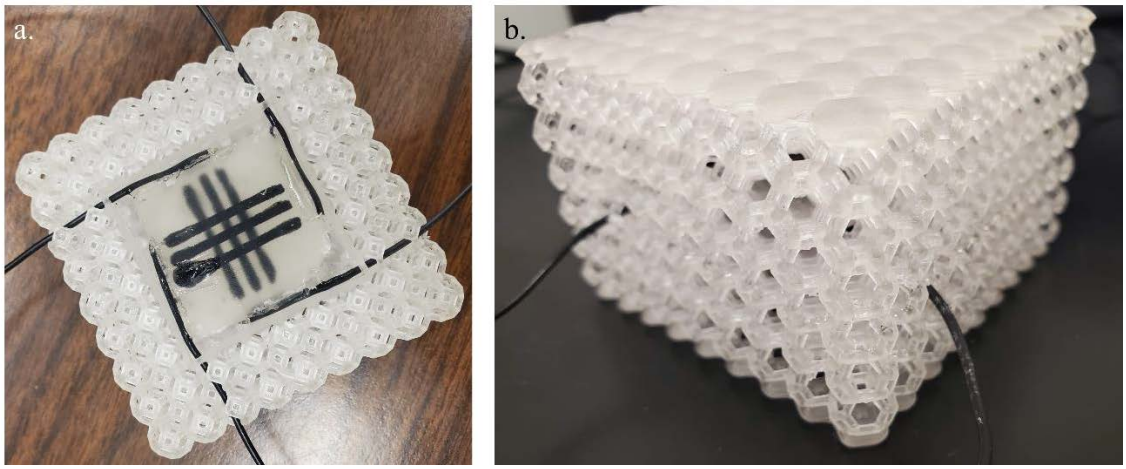

Figure 3.10: (a) Half lattice with sensor inserted and (b) full lattice with visible signal wiring.

A circuit schematic for the sensing system is shown in Figure 3.11 and a photo of the entire testing setup is shown in Figure 3.12. In the schematic, the lattice is displayed on the left and the signal then travels through multiple filters before being amplified by an operational amplifier. The power supply is located toward the top of the figure and the microcontroller is labeled MCU on the right side. In the photo, the lattice is located on top and is connected to a breadboard for easy modification of wires. The breadboard was wired to a circuit board with the MCU and a power supply, which provided 3 volts.

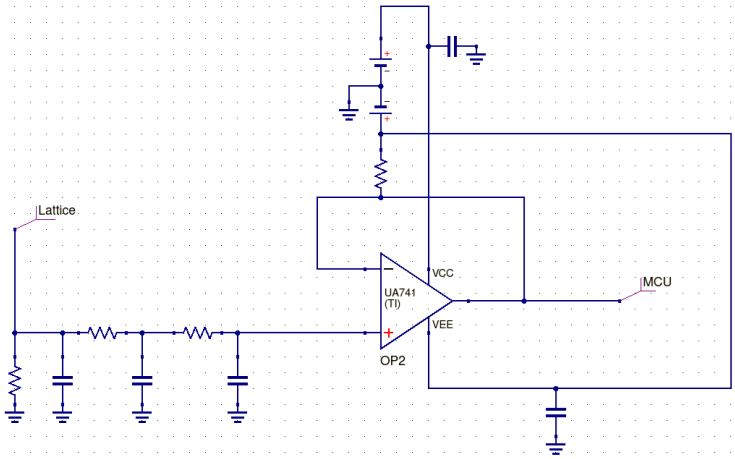

Figure 3.11: Circuit schematic of the embedded sensor lattice system. The lattice itself is shown on the left side of the figure, while the microcontroller, labeled MCU, is shown on the right.

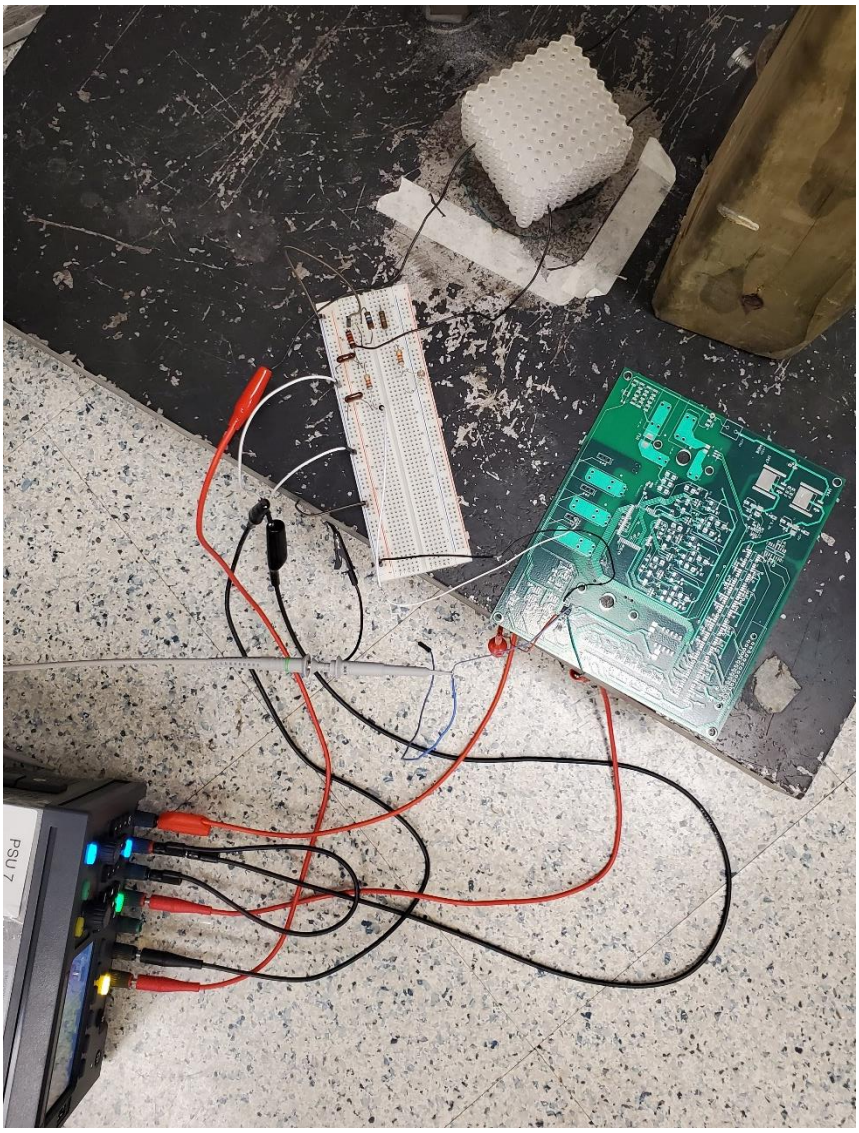

Figure 3.12: Photo showing complete setup of sensor testing. Included are the power supply (bottom left), breadboard (middle), circuit board (right), and lattice on steel platen for impacting (top).

Testing on the lattice-sensor system was performed in a similar manner to the previous low velocity impact analysis. After the wiring was completed and verified to be working correctly, impacts ranging from 3.20 J to 28.34 J were recorded using the 4.66 kg platen from the initial individual lattice tests. Data was compared to load cell and oscilloscope results from the same impact to scale the MCU voltage output properly. Testing was performed with both a wired and wireless data connection.

4.0 Results and Discussion

This section presents the testing results and data analysis findings from lattice experimentation. Overall, this research examines the impact performance and energy absorption performance of elastomeric additively manufactured lattices. Multiple materials and functionally-graded designs of a Kelvin cell lattice were used. Combinations and modifications to these lattices were made to analyze their performance in different scenarios which include a hybrid system, a helmet apparatus, and an embedded flexible sensor setup.

4.1 Individual Lattices

Testing on individual lattices was completed in two phases as mentioned above. The first phase consisted of impact testing of Carbon SIL 30 and Ultimaker TPU 95A (ULTI) lattices in vertically-graded and non-graded orientations. These materials were tested prior to the testing of the remaining samples from phase 2. The latter phase consisted of EOS TPE 300, NinjaTek NinjaFlex, and FormLabs Rebound along with three different spatial variations: non-graded, vertically-graded, and side-graded. With the 4.66 kg impact platen, different impact heights corresponded with different impact energies. Experimentally-derived values for corresponding drop heights to velocities and energies can be seen in Table 4.1 below.

Table 4.1: Impact heights and corresponding energies and velocities as determined from experimental results.

Height (cm)	*Impact Energy (J)*	*Mean Velocity (m/s)*
5	3.20	0.98
10	5.49	1.44
15	7.77	1.68
20	10.06	1.91
30	14.63	2.29
40	19.20	2.70
50	23.77	3.15
60	28.34	3.26

4.1.1 SIL 30 and TPU 95A Lattices

Low velocity impact and basic quasi-static compression testing was performed on the SIL 30-NG (non-graded), SIL 30-VG (vertically-graded), ULTI-NG, and ULTI-VG lattices for phase 1. Densification of lattice structures is reached once the struts are collapsed and the padding is fully compressed [4]. At the densification point, the material may be soft enough to still absorb some of the impact; however, the lattice structure itself is unable to continue attenuating the force. The densification point is represented in quasi-static stress-strain curves by the sudden increase in strain [131]. Densification is also observed in low velocity impact force-displacement graphs as the curve spikes in force without increasing much in displacement. The densification point is important to consider in lattice testing because fully compressed padding is ineffective at absorbing any meaningful amount of energy. SIL 30 samples experienced densification after approximately 7.77 J, and ULTI samples began to densify around 14.63 J of impact energy.

Due to low velocity impact densification occurring at the 7.77 J impact for the SIL 30 lattices, graphs with force contain the initial three impacts (up to the 7.77 J impact) for clarity. Also, the first five impacts are shown for the ULTI lattices due to its increased stiffness and ability to mitigate higher energy impacts without reaching densification. Figure 4.1 shows force versus time data for the four initial lattices. Much of the beginning tests for these lattice samples were performed by Jose G. Carrillo under Dr. Pedro Cortes at Youngstown State University. An oscilloscope connected to a load cell and amplifier was utilized to collect force information throughout each impact. Results were subsequently analyzed using Excel.

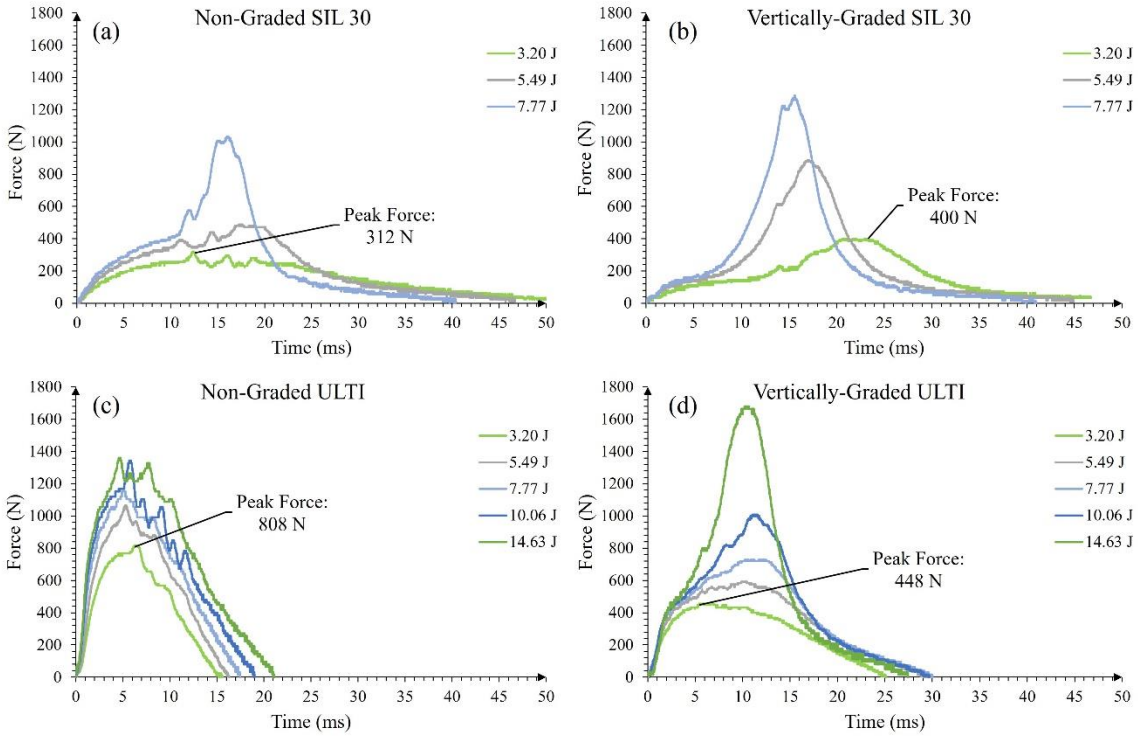

Figure 4.1: Force versus time curves for SIL 30 and TPU 95A (ULTI) lattices at various impact energies (corresponding to 5, 10, 15, 20, and 30 cm heights).

In Figure 4.1, both variations of SIL 30 seem to experience lower peak force than ULTI for the 3.20 J impact. A low peak force resulting from low impact energies is caused by a softer attenuation nature; the SIL 30 material is significantly more pliable than the ULTI lattices. Note the drastic increase in peak force as the impact energy increases for SIL 30. By 7.77 J of impact energy, the peak observed force is approaching that of the ULTI lattices at higher impact energy levels. The stiffness of the ULTI material contributes to its ability to absorb higher energy impacts. Another conclusion drawn from these curves is that the vertically-graded orientation exhibits a longer attenuation time. Even though the peak force increases on the vertically-graded configuration more rapidly than the non-graded version of each lattice, for lower energy impacts, the vertically-graded setup seems ideal. The thinner struts on bottom of the lattice buckle and fail before the thicker struts are bent under impact. Therefore, even though the lattice is overall weaker, it produces a more tuned and customizable impact profile.

By combining the above data with information from the high-speed video camera, force versus displacement graphs can be produced. Figure 4.2 shows these graphs for the four tested lattices of phase 1.

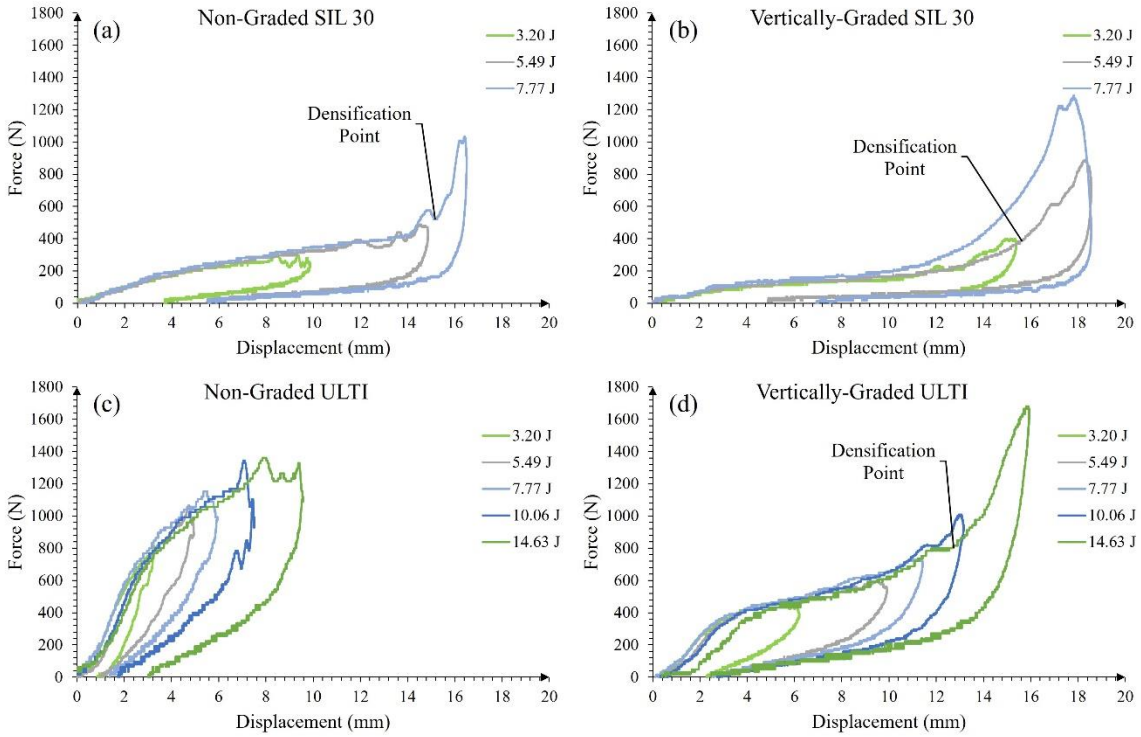

Figure 4.2: Force versus displacement curves for SIL 30 and TPU 95A lattices at various impact energies with densification points labeled.

Figure 4.2 shows these force-displacement combined data sets for multiple impacts per lattice. Densification points are labeled at the initial upturn in force; note that densification is not observed in non-graded ULTI in the selected impacts. To show the densification point in Figure 4.2c, higher energy impacts would have to be shown. SIL 30 was shown to be a significantly softer material by the low force and high displacement required to produce densification. Since the absorbed energy is the integration of the force-displacement graph with bounds at zero and the densification point like in Equation 3, high absorbed impact energy is shown by the large curve-enveloped area.

The absorbed energy until the densification point is shown in Figure 4.3. Here, the samples were impacted until full densification, at which the absorbed energy was

calculated by Equation 3. Absorbed energy was then normalized by lattice mass to produce a scalable absorption capability, also called specific densification energy, and is measured in units of J/kg. The chart is overlaid with Young's Modulus, or stiffness, for each combination. SIL 30 shows lower stiffness and specific densification energy than ULTI, which means the TPU 95A material is capable of absorbing more energy before densification per unit mass. The superior performance of ULTI in specific densification energy can largely be attributed to its high densification energy.

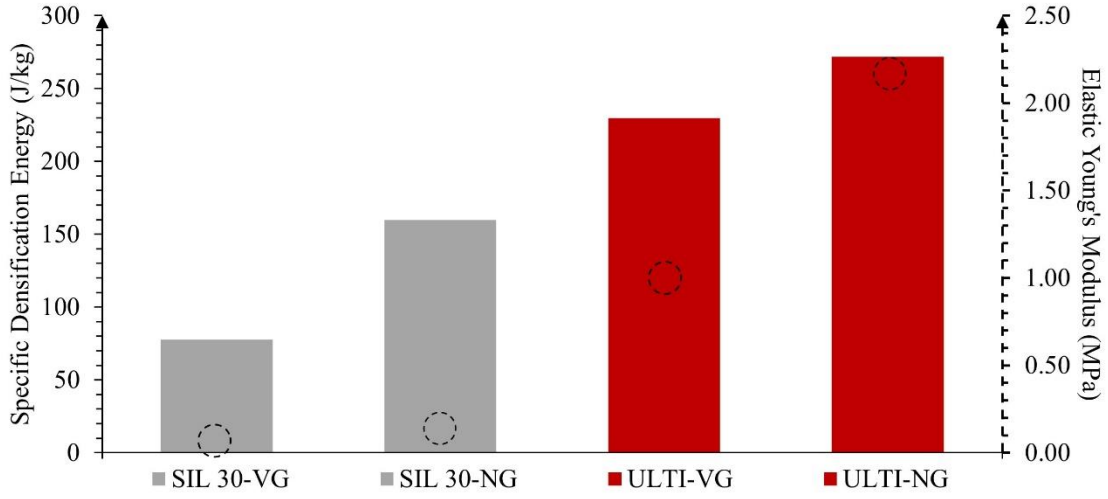

Figure 4.3: Absorbed energy at densification for each material and gradation combination, normalized by mass.

The difference in performance of the materials in different situations leads to the possibility of further profile tuning by combination of the lattice materials themselves. Rather than only designing the model to have thicker and thinner struts, two materials can have a significantly wider gap in usable energy ranges. For example, no matter how thick the SIL 30 lattice struts are designed, it will likely not ever achieve the level of stiffness of UTLI, and vice versa. Lattice combinations can produce a wider range of application and lead to higher tailorability. Blending of materials and lattice configurations will be discussed in detail later.

4.1.2 Quasi-Static Compression of TPE 300, NinjaFlex, and Rebound Lattices

In-depth compression testing was completed with EOS TPE 300 NG, VG, and SG (side-graded), NinjaTek NinjaFlex NG, VG, and SG, and FormLabs Rebound NG, VG, and SG lattices for phase 2 of the individual analysis. Data collected from quasi-static Instron testing was used to calculate densification energy and energy absorption efficiency of the lattices. Energy required to reach lattice densification is shown in Figure 4.4 for the non- and vertically-graded configurations with all three materials (side-graded lattice testing will be discussed later and was not directly comparable to the other gradations). Here, NinjaFlex is the lowest for all three combinations due to its softness. Rebound is significantly stiffer and requires high force compression to fully densify. Note the non-graded version of TPE 300 and NinjaFlex having higher densification energies compared to their other combinations. Rebound was found to have been poorly post-processed, resulting in filled lattice voids (these can be seen in Figure 4.5). Thus, vertically-graded Rebound exhibits a greater densification energy due to its increased stiffness from the extra material versus the default non-graded model. Thinner struts reduce the stiffness of the lattice, which would normally cause the densification energy to be lower.

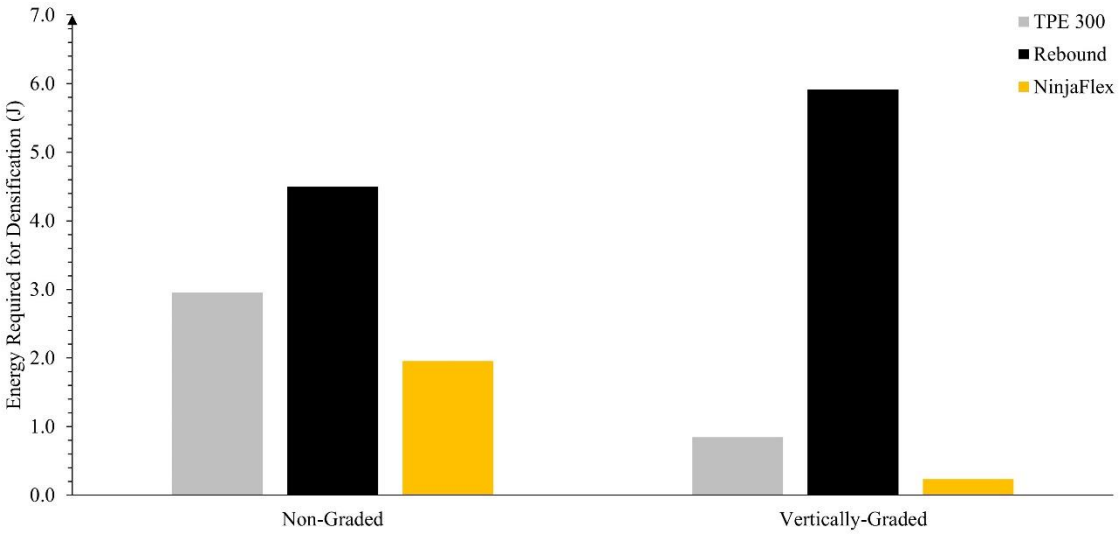

Figure 4.4: Densification energies for all tested lattice combinations from phase 2. Stiffer materials require more energy to fully compress all struts, which translates to a higher densification energy.

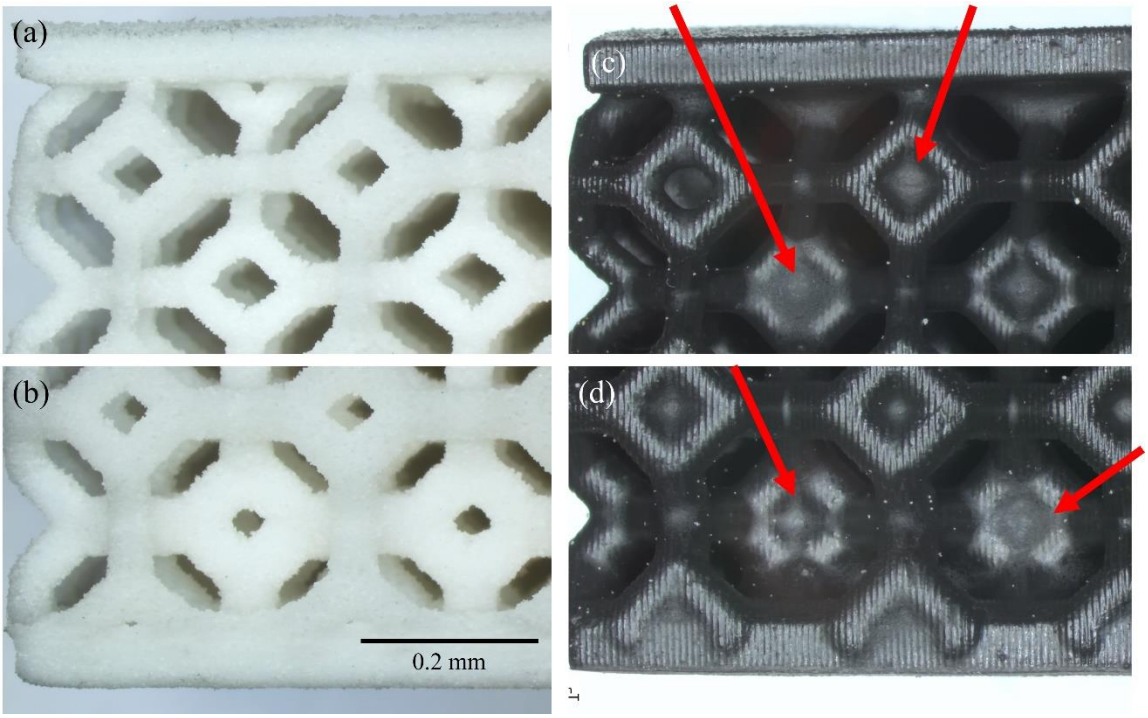

Figure 4.5: Microscope images showing (a) thin struts of VG TPE 300, (b) thick struts of TPE 300, (c) thin struts of VG Rebound, and (d) thick struts of VG Rebound. Note the incorrectly filled voids on the Rebound sample (shown by red arrows), which resulted in increased stiffness.

Energy absorption efficiency (EAE) is another metric that can be calculated from quasi-static compression testing. Equation 4 shows the calculation required to produce EAE. Efficiency curves help to display where the absorption profile of each lattice is most effective. These curves are shown below in Figure 4.6. In these graphs, vertically-graded lattices are shown to be more efficient with low displacement, likely due to the thin struts that are specifically designed for these low energy impacts. Alternatively, non-graded lattices peak in efficiency later in compressive displacement and then decrease rapidly. The vertically-graded conformation decreases much more linearly, eventually returning to the efficiency levels of the NG variation. In fact, for NinjaFlex in Figure 4.6c, the vertically-graded lattice surpasses the efficiency of the non-graded towards the extreme end of the displacement scale (70%+).

$$EAE = \frac{\int_0^{\varepsilon} \sigma(\varepsilon) d\varepsilon}{\sigma\varepsilon} \quad (4)$$

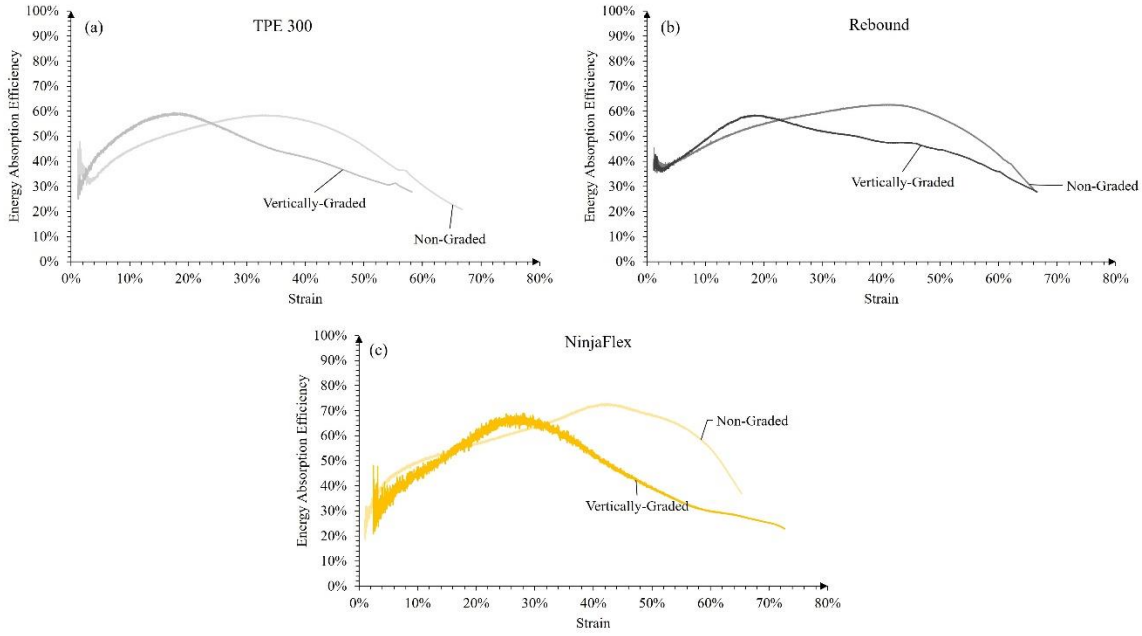

Figure 4.6: Energy absorption efficiency for each lattice combination. Optimal lattice configurations can be determined for different levels of displacement.

4.1.3 Low Velocity Impacting of TPE 300, NinjaFlex, and Rebound Lattices

Low velocity impact testing was also performed with these TPE 300, NinjaFlex, and Rebound lattices. The non-graded and vertically-graded lattices were tested in the same way as previously done. The first data collected and analyzed from the low velocity impact testing was force-time information from the load cell and oscilloscope, as shown in Figure 4.7. Here, optimal impact performance is shown by a wide peak and low peak force. Densification is easily observed at high impact energy levels by the sudden increase in force. In these graphs, vertically-graded lattices show a less drastic increase between energy levels than non-graded samples. Also, TPE 300 exhibits a peak force less than Rebound or NinjaFlex for both its non-graded and vertically-graded configurations. Lower peak force contributes to less opportunity for head injury on impact.

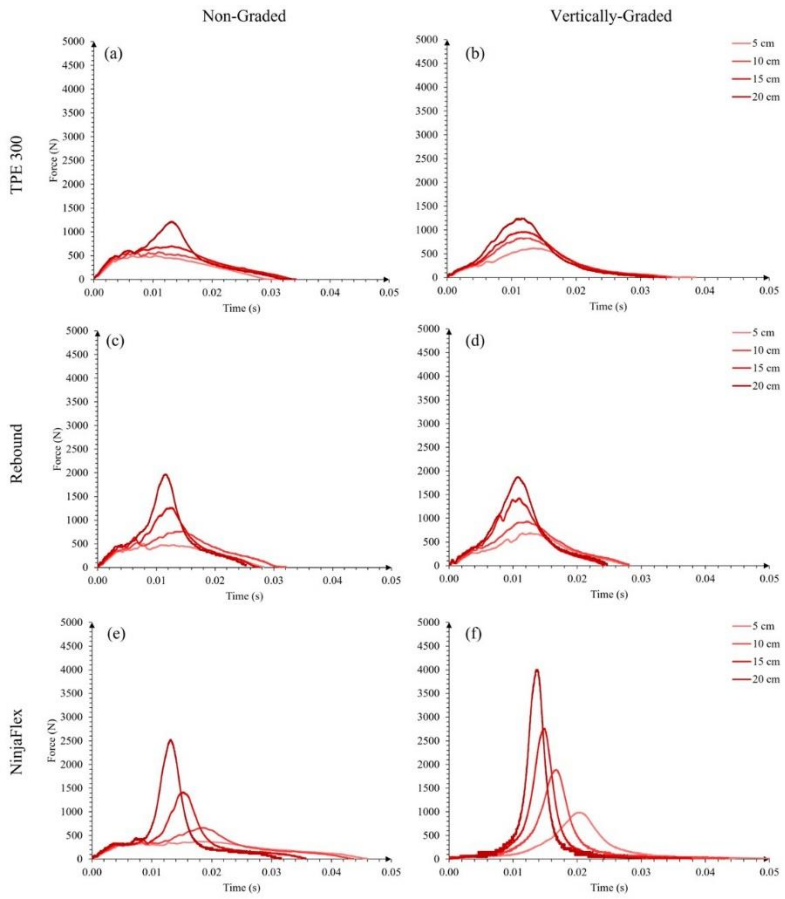

Figure 4.7: Force-time curves for the first four impacts of each material and spatial gradation. Densification is shown by the sharp peak of a force curve.

Figure 4.8 shows force versus displacement data for the first four impacts. The data shown was collected by combining information from the load cell setup and the high-speed video camera. Figure 4.8a-b shows the TPE 300 system exhibiting lower displacement than NinjaFlex (Figure 4.8e-f) due to the stiffness of TPE 300. Rebound, as shown in Figure 4.8c-d, performs similarly to TPE 300; slightly higher stiffness led to more pronounced peaks for Rebound rather than rounded peaks for TPE 300.

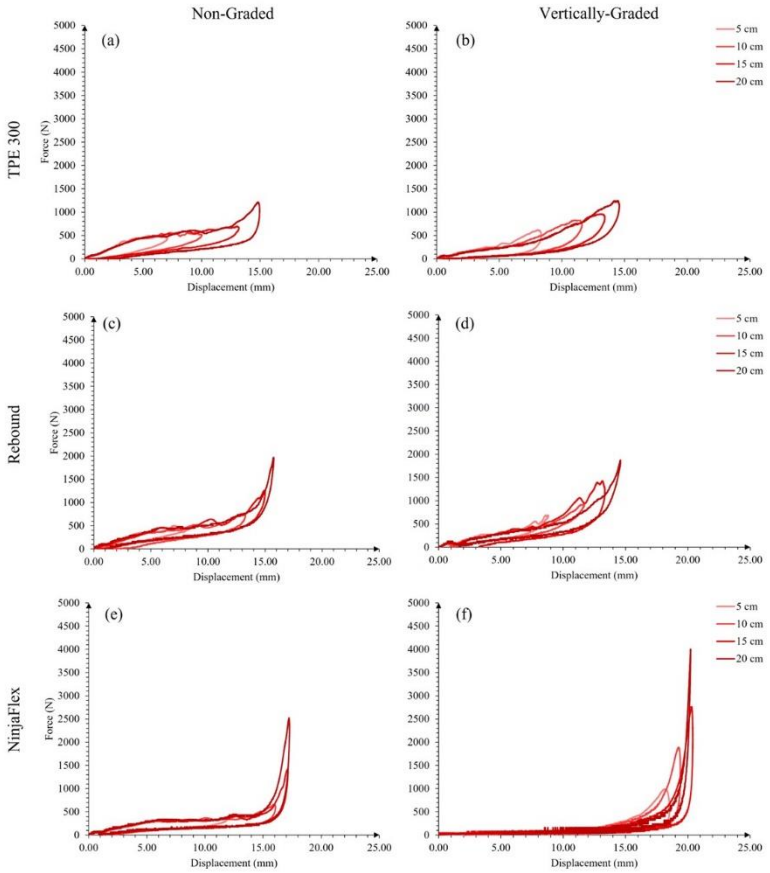

Figure 4.8: Force-displacement curves for the first four impacts of each material and spatial gradation. Densification is shown by the sharp increase in force without increase in displacement.

Since densification energy plays an important role in determining the absorption range and capability of lattices, Figure 4.9 was created to compare the absorbed energy ability of each combination. Integrating the force-displacement curve for each impact and material yields absorbed energy. Setting bounds at zero and the densification point produces actual absorbed energy by excluding energy transmitted through the lattice into the fixed bottom platen of the impact tower. In Figure 4.9, both vertically-graded and non-graded TPE 300 performed well, with only non-graded NinjaFlex outperforming TPE 300 at very low impact energies. The wide range of impact energy applications for TPE 300 contribute to its superior performance and selection for use in a hybrid system for further analysis. Also, the NinjaFlex displayed good cushioning performance at low energy impacts, which is also important in the comfort of wearable protective systems. Therefore,

non-graded NinjaFlex and vertically-graded TPE 300 were selected to be combined into a hybrid lattice to analyze the compromise in performance by combining two materials with different properties and energy absorption capabilities.

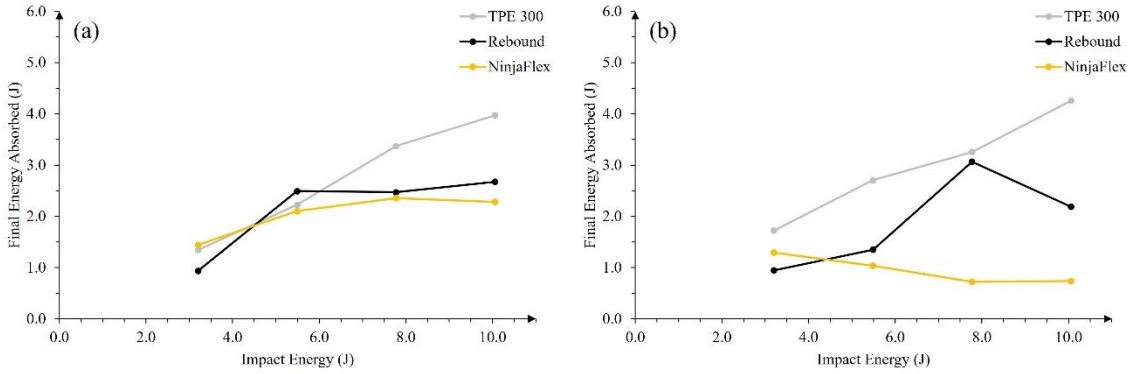

Figure 4.9: Absorbed energy at densification of each lattice material for (a) non-graded and (b) vertically-graded configurations.

4.2 Hybrid Lattices

Single material lattice properties are ultimately confined by the extremes of the material and the printing process. For example, a solid block of one very pliable elastomer may be still less stiff than a normal lattice of another tough elastomer. Also, that same tough elastomer may not be able to be successfully printed with thin enough struts to make its stiffness as low as that of the pliable material. Thus, multiple materials may be needed to expand the applicable energy absorption range of a lattice structure. By combining two different materials with different properties and strengths, it was found that there is a compromise occurring. While the new hybrid system exhibits usefulness at a wider range of impacts, the performance may be limited across that range in exchange for the broadened performance. The compromise when lattice materials are combined into a hybrid system is examined in this section.

4.2.1 VG ULTI and VG SIL 30

Phase 1 of the low velocity impact testing consisted of non- and vertically-graded SIL 30 and ULTI. VG SIL 30 and VG ULTI were combined into a hybrid lattice (Hybrid

1) due to the interesting spatially-varying nature of the individual lattices. For the following testing, double-stacked versions of VG SIL 30 and VG ULTI were tested to make direct property comparisons with comparable dimensions to Hybrid 1. Hybrid 1 was formed by fixing ULTI to the top of the SIL 30 sample. A snapshot of the impact situation can be seen in Figure 4.10. Here, the stiffness of ULTI is very clear; SIL 30 compresses instantly and ULTI only begins to absorb the impact after SIL 30 densification, which is a great example of the improved energy range of applicability that hybrid lattices produce.

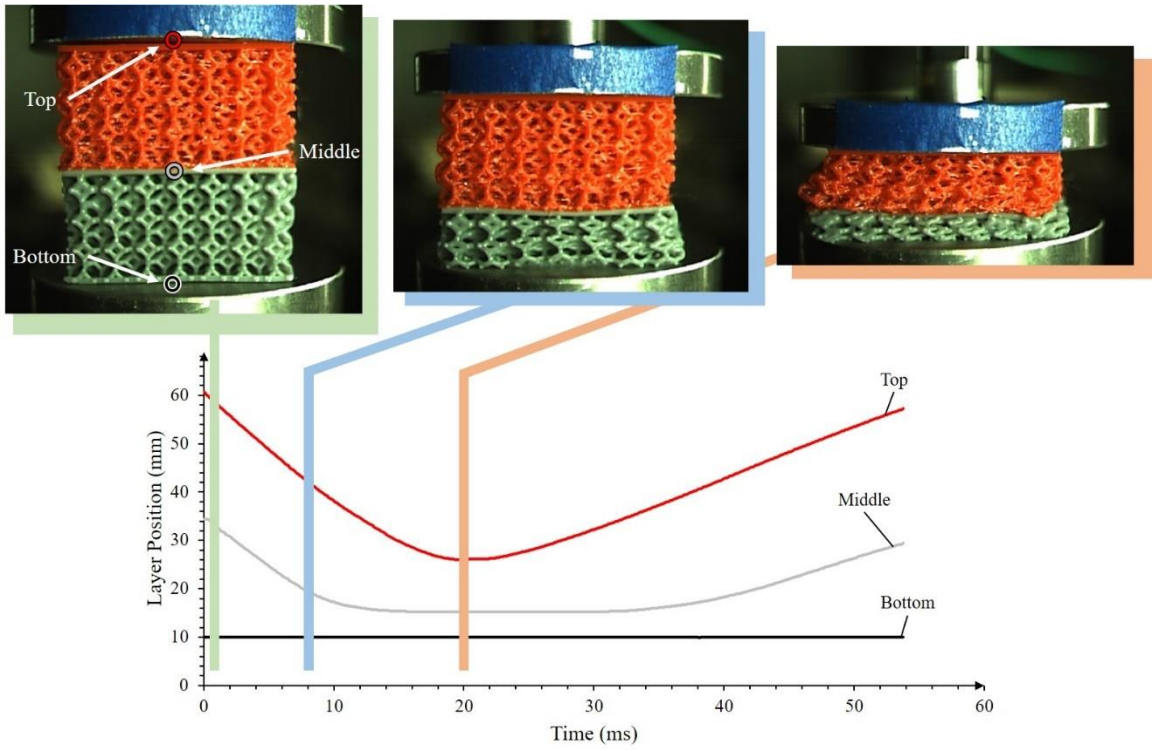

Figure 4.10: Snapshots of Hybrid 1 impact during the 14.63 J test. Note the immediate densification of SIL 30 and the stiffness of ULTI until the end of the compression.

In the low velocity impact testing, a few different energies were tested. A low (3.20 J) and a high (10.06 J) energy impact were selected for analysis in the figures below. Here, wide curves with low peak forces are desired. Figure 4.11a shows the excellent performance of SIL 30 compared to the other samples because of its 212 N peak force and long 80+ millisecond impact duration. Figure 4.11b shows the good performance of ULTI at a higher energy impact compared to the softer SIL 30, which experiences densification.

Also, Hybrid 1 performs as expected; in both graphs, the combined system is not excellent in either, but rather acceptable in both.

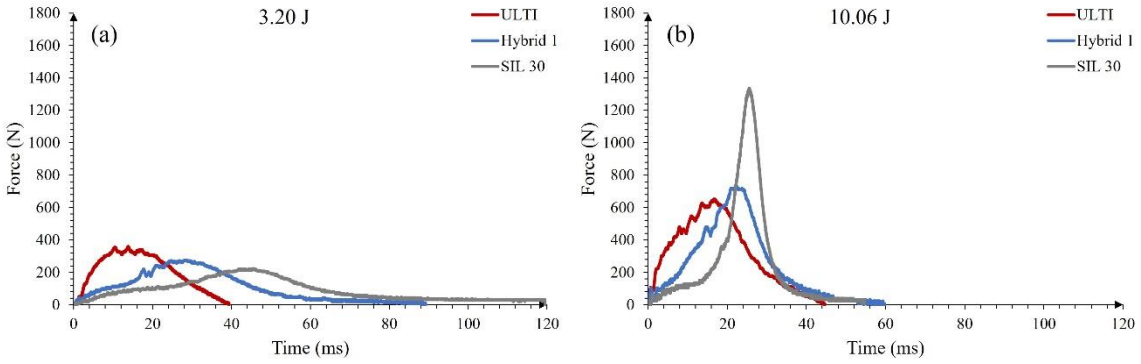

Figure 4.11: Force-time curves for VG ULTI, VG SIL 30, and Hybrid 1.

Since SIL 30 possesses a softer feel and is densified relatively easily, its absorbed energy at densification is not high compared to the other materials. Alternatively, the damping nature of the soft SIL 30 lattice increases the impact time to densification over the other options, Hybrid 1 and ULTI. Figure 4.12a displays the useful energy absorption capability of each lattice system, which corresponds to the energy absorbed at densification. Also displayed in the figure are the impact times associated with the densification points; longer impact attenuation before densification is reached would be desirable in a protective padding situation. Figure 4.12b shows mass-normalized energy absorption capability (specific impact energy, or SIE) for each lattice. Since these structures are being tested for utilization in protective equipment, mass is a factor that cannot be ignored. SIL 30 is a dense material and does not perform as well as ULTI, which has a high energy absorption ability per unit mass. These two figures show that properties can be modified with the use of different materials. Hybrid 1 continues to produce results in between its constituent systems.

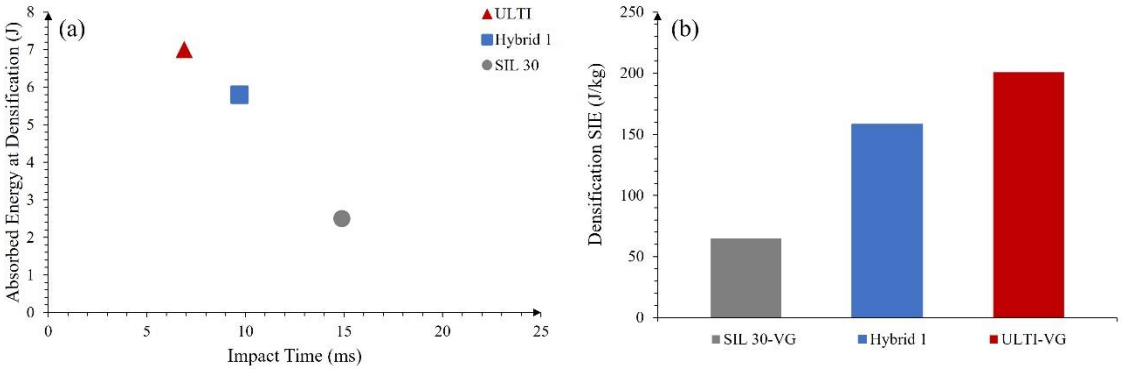

Figure 4.12: Graphs showing (a) absorbed energy at densification for constituent systems and Hybrid 1, and (b) densification SIE for all tested systems.

Figure 4.13 shows the peak energy observed for each impact versus the time until that peak energy was observed. The figure highlights the balance between the different materials and different attenuation techniques employed. Peak energy during ULTI impacts occurred in about half the amount of time when compared with SIL 30. Also, the impact time decreases significantly from test to test for SIL 30 due to the softness. Each increase in impact energy results in much quicker compression than the previous test. These behaviors make sense, as the soft profile of SIL 30 is drastically different from the stiff nature of ULTI. Once again, Hybrid 1 exhibits properties in between SIL 30 and ULTI. By combining both systems, the total Hybrid 1 lattice is able to have a similar usable energy range as ULTI and a longer energy absorption time frame like SIL 30.

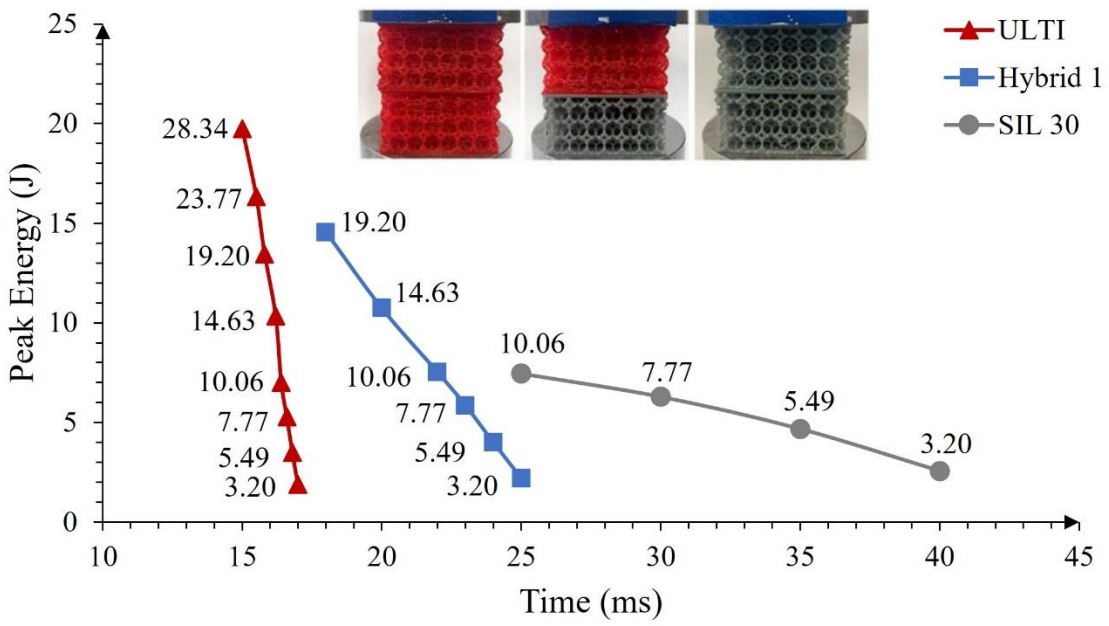

Figure 4.13: Peak energy absorbed at various impact energies versus time until peak energy was observed.

The high-speed video camera was used to calculate displacement as well as velocity and acceleration. An acceleration analysis was performed with the Hybrid 1 structure and its constituents to determine the peak accelerations experienced by the load cell. In the testing, lower peak accelerations are necessary for head safety because of the reduced risk for TBI [36]. Figure 4.14 shows the acceleration curves for each lattice system: double-stacked ULTI VG, Hybrid 1, and double-stacked SIL 30 VG. In Figure 4.14a, Hybrid 1 exhibits a much longer impact time than ULTI (almost 3 times longer). That lengthening contributes to a much less abrupt change in velocity. SIL 30 displays a lower peak acceleration and long impact time, which supports the notion that the soft material is best in low energy impact scenarios for cushioning and dampening the impact. Also, Figure 4.14b shows a higher energy impact where Hybrid 1 reduced the peak acceleration from almost 35 g for SIL 30 to 17 g for ULTI and Hybrid 1. By combining properties of both SIL 30 and ULTI, once again Hybrid 1 performs relatively good in multiple scenarios, when the single materials would have performed great in only one of the two situations.

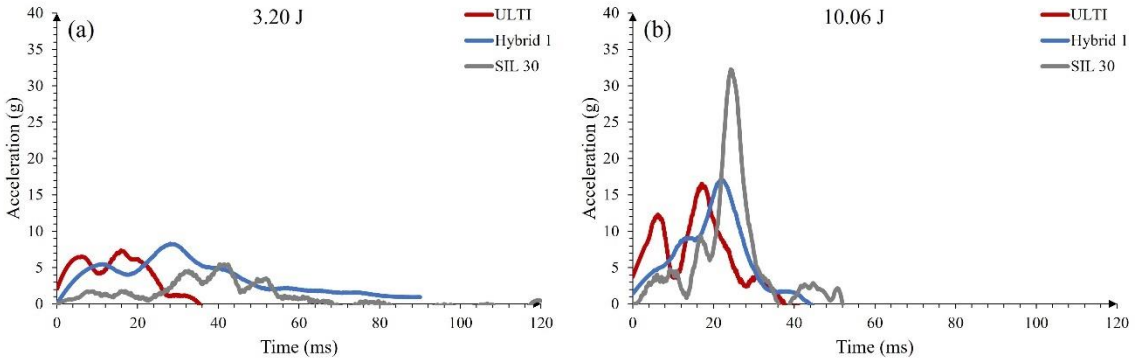

Figure 4.14: Acceleration responses of all three lattice configurations. Lower peak accelerations translate to safer impact attenuation.

4.2.2 VG TPE 300 and NG NinjaFlex

Phase 2 of the lattice testing resulted in vertically-graded TPE 300 and non-graded NinjaFlex being selected for combination into a hybrid lattice called Hybrid 2. The selection was based on the good all-around energy absorption ability and high absorption efficiency of vertically-graded TPE 300 and the softer nature of non-graded NinjaFlex. Once again, double-stacked versions of the constituent lattice materials were tested alongside Hybrid 2, which had TPE 300 fixed on top and NinjaFlex on bottom.

Efficiency testing was performed on these double-stacked lattices and Hybrid 2 during quasi-static compression like in Figure 4.6. The new curves, found in Figure 4.15, show how the lattice systems absorb energy as they are compressed. Since NinjaFlex is less stiff than TPE 300, 50% strain may be achieved with significantly less compression energy. TPE 300 peaks in efficiency and decreases in a linear fashion, a feature of its vertically-graded design. NinjaFlex increases to a peak of over 70% efficiency at 40% compression and then rapidly falls off. Hybrid 2 combines features of both efficiency curves by showing two peaks: one at around 12% strain and the other at about 38%. Interestingly, these peaks correspond with the peaks of the individual materials, making the Hybrid 2 system relatively efficient through a wider range of compression than either of the two individual lattices.

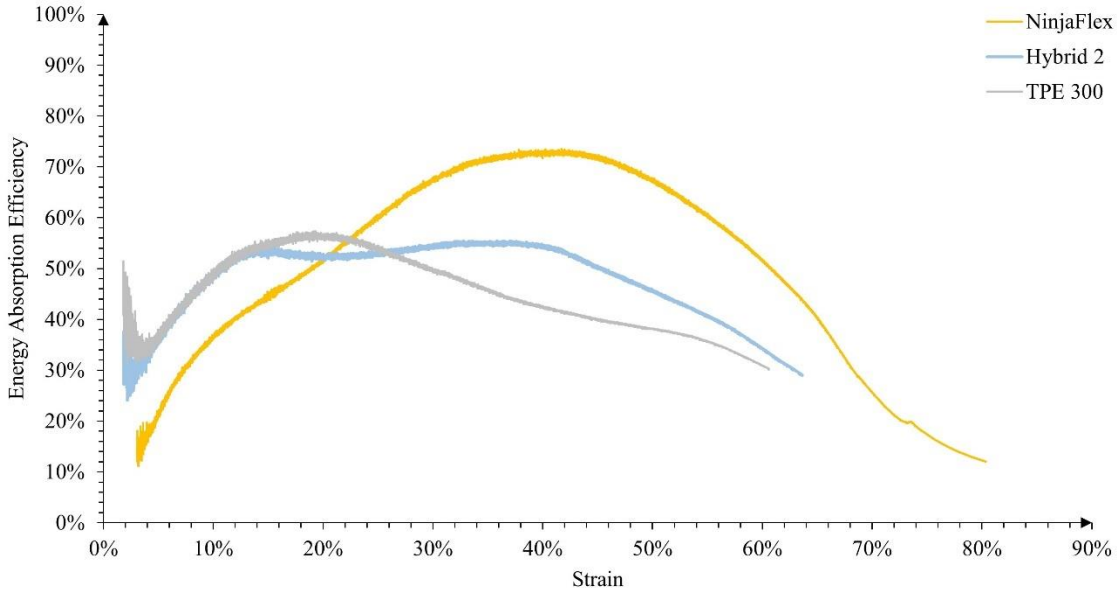

Figure 4.15: Energy absorption efficiency from quasi-static compression testing of double-stacked lattices and Hybrid 2.

Low velocity impact testing was performed on the double-stacked VG TPE 300, NG NinjaFlex, and Hybrid 2 from various impact heights as outlined in Table 4.1. A few frames from the 10.06 J impact (20 cm height) are shown below in Figure 4.16. Here, the weak struts of TPE 300 collapsed easily upon impact, while NinjaFlex and strong struts of TPE 300 remained supportive. As Hybrid 2 is compressed, NinjaFlex and TPE 300 begin to collapse until densification. The modular approach to impact mitigation used in Hybrid 2 contributes to its broad efficiency range during collisions.

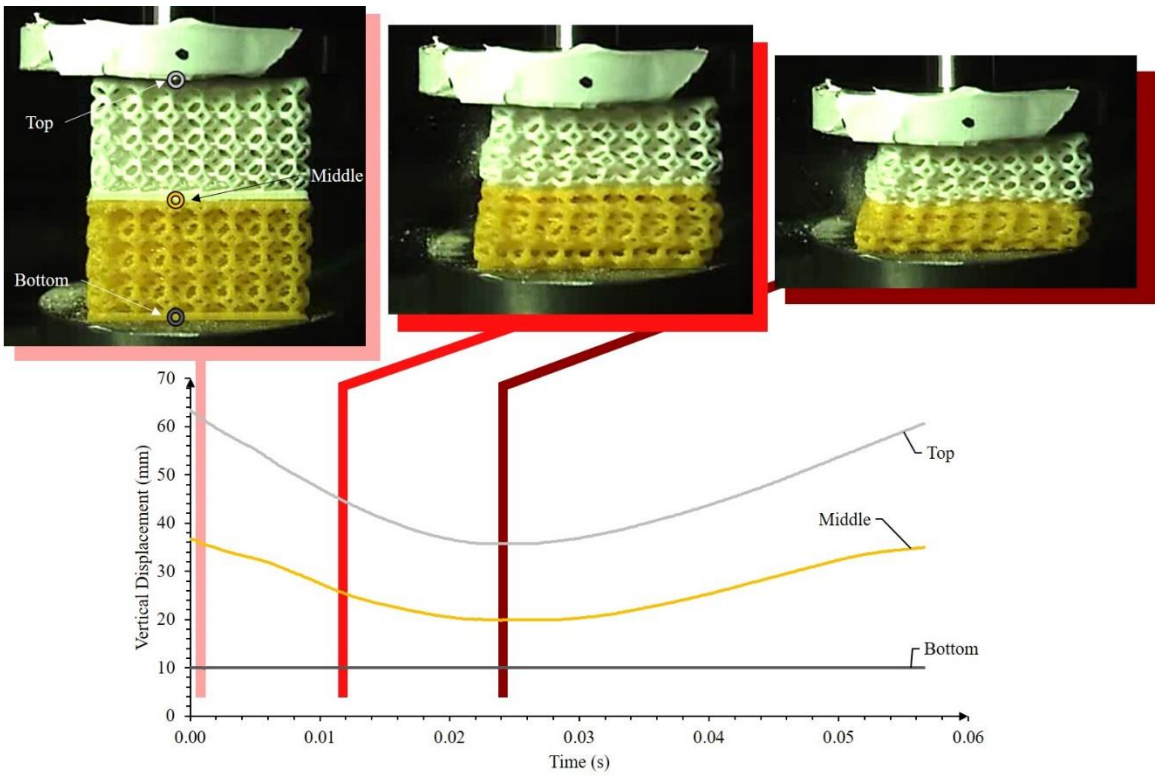

Figure 4.16: 10.06 J (20 cm) impact of Hybrid 2 from high-speed video footage. TPE 300 is the white lattice on top and NinjaFlex is shown in yellow on the bottom.

In a similar manner to previous testing, force versus time data was recorded via the load cell and oscilloscope combination. Double-stacked VG TPE 300 and NG NinjaFlex were tested alongside Hybrid 2 in the vertical impact tower under various drop heights. Select tests (10.06 J and 28.34 J) are shown in Figure 4.17, where the different strengths of each material are apparent. NinjaFlex performs well under a 10.06 J (20 cm) impact by lengthening the total time and reducing the peak force observed. NinjaFlex exhibits an impact time of over 30% greater than TPE 300 and 20% greater than Hybrid 2 for the 10.06 J trial. Also, its peak force is approximately half that of the TPE 300 and Hybrid 2 samples for the same impact. Alternatively, NinjaFlex shows signs of earlier densification than the other two samples, with its peak force in Figure 4.17b spiking to almost 3000 N compared to 1500 and 2000 N for the TPE 300 and Hybrid 2 samples, respectively. Performance of the Hybrid 2 falls in between the components for both tests as expected.

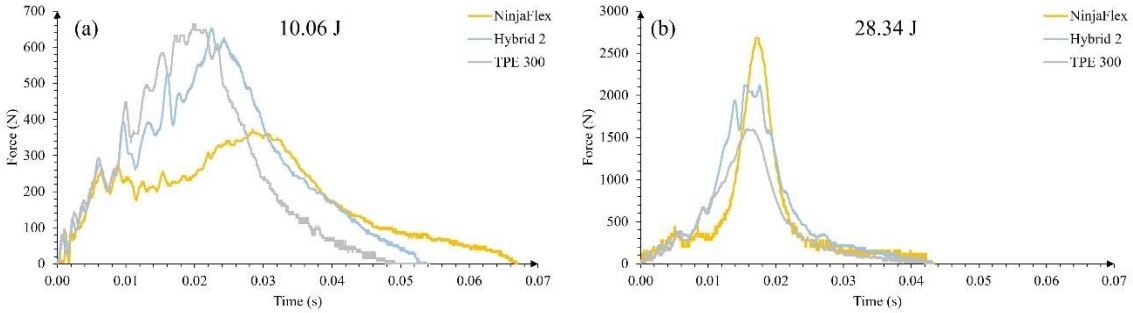

Figure 4.17: Force versus time data for two selected impact energies from Hybrid 2 testing. Also shown are double-stacked NG NinjaFlex in yellow and VG TPE 300 in grey.

An expanded view of the peak force performance was constructed to more easily view densification data. Figure 4.18 shows the percent displacement of the double-stacked samples versus the peak observed force during low velocity impacts. The impact energies for each point are labeled and the rough densification point for each sample is also identified. For reference, the peak force from both impacts shown in Figure 4.17 are depicted in Figure 4.18 by the corresponding point. Densification is characterized by a sudden increase in peak force without any significant increase in displacement. NinjaFlex, as the softest material, exhibits an early densification point – accomplished by about 400 N of force. TPE 300 and Hybrid 2 display later densification points that are much less obvious. These points could be anywhere from the 7.77 J impact to the 14.63 J impact. Peak force continues to increase past densification due to energy transmission through the lattice into the solid bottom platen. Since there is no more absorption past densification and the amount of induced impact energy rises with each increase in impact height, the peak force continually increases without any subsequent increase in lattice displacement.

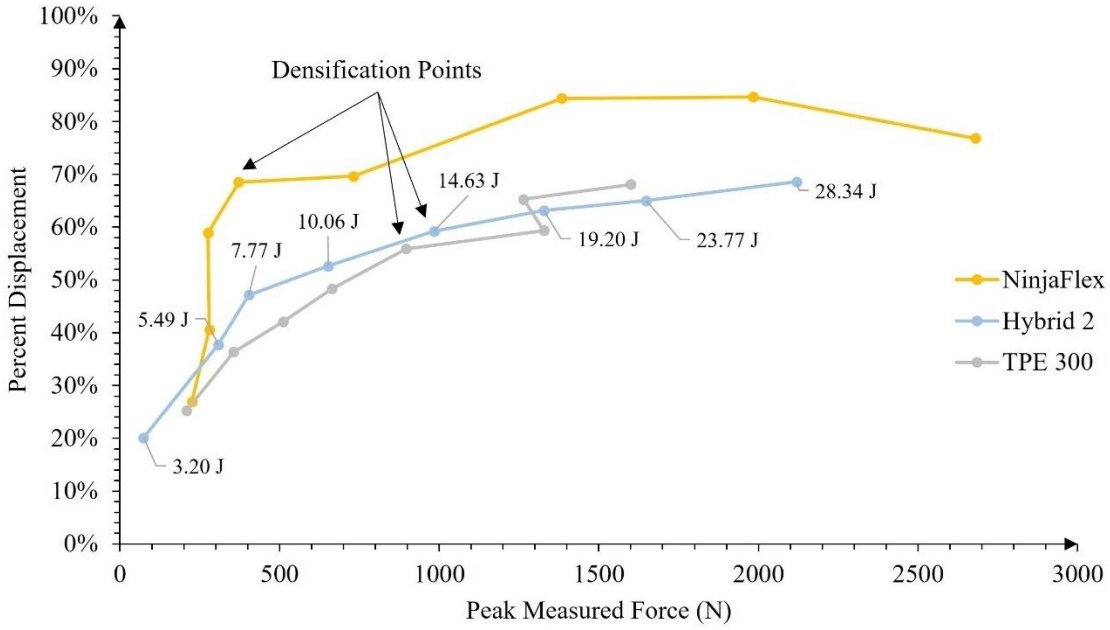

Figure 4.18: Percent displacement versus peak measured force during low velocity impacts of double-stacked NG NinjaFlex, VG TPE 300, and Hybrid 2.

Various metrics exist to compare different materials and their energy absorbing capability. One of these is specific impact energy (SIE), which is the energy absorbed at densification normalized by the lattice model density. The density referred to here uses the mass and volume of the lattice including air pockets. Densification SIE is essentially a normalized total energy absorption ability per unit density and is a useful tool to utilize when deciding between certain materials. Double-stacked TPE 300, NinjaFlex, and Hybrid 2 densification SIE values are shown in Figure 4.19. Some elastomers, like NinjaFlex, excel at absorbing energy in a relatively lightweight form factor. Other materials are denser but absorb more energy, resulting in a lower densification SIE. Padding application and type of energy absorption may require different cushioning materials.

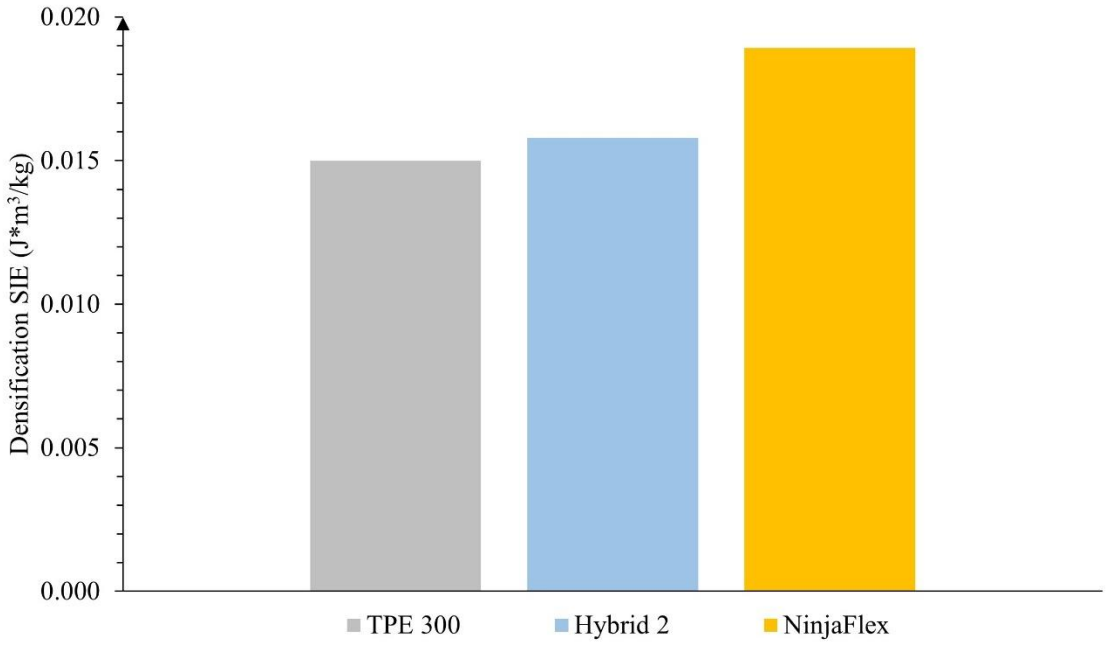

Figure 4.19: Densification specific impact energy (SIE) for each double-stacked lattice and Hybrid 2. SIE is density-normalized energy absorbed at densification.

Acceleration is also an important value to measure on these low velocity impacts. As stated previously for SIL 30, ULTI, and Hybrid 1, accelerations during collisions are one of the leading causes of TBI [36]. Here, acceleration data was calculated from multiple smoothed differentiations of position-time results. NinjaFlex exhibited a superior acceleration profile during the 3.20 J impact mitigation, likely due to its "softness". Peak acceleration of 4 g was documented, while the other samples recorded peak accelerations of almost 15 g. Alternatively, for the 10.06 J impact, all lattices registered accelerations of between 15 and 20 g. According to common head injury metrics, a human head can withstand 42 g of acceleration for a couple tens of milliseconds before injuries result [6]. Therefore, none of the impacts from the testing shown would have caused brain injuries as predicted by legacy calculations. The results here are promising for the application of AM elastomers as padding replacements.

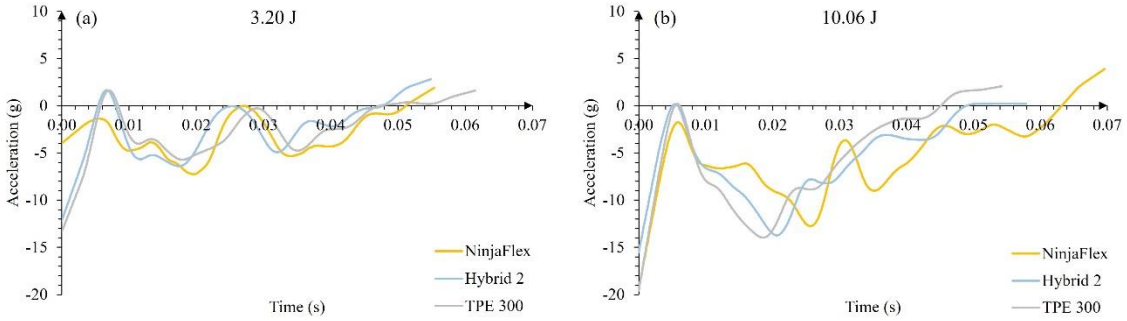

Figure 4.20: Acceleration results from (a) 3.20 J impact and (b) 10.06 J impact for double-stacked NinjaFlex, TPE 300, and Hybrid 2.

4.3 Side-Graded Lattices

Since side-graded lattices were manufactured for a different purpose than to absorb only linear impacts, they were hard to compare to the non-graded and vertically-graded samples in different tests. To compare side-graded lattices properly, finite element analysis (FEA) computer simulations were performed by José Angel Diosdado-De la Peña of the Materials Science department at Youngstown State University. These simulations compared the performance of side-graded lattices to non-graded lattices in oblique impact situations.

Before modeling was performed, side-graded lattices were tested under quasi-static compression and low velocity impacts on a 12° incline. 12° was determined from the angle of the self-aligning platen outfitted on the Instron universal testing machine. As the lattice densified during the compression, the top platen was allowed to tilt to accommodate the stronger and weaker sides of the lattice appropriately; the observed angle was averaged to be 12°. Figure 4.21 shows the experimental method used to determine the approach angle for low velocity impacts. Side-graded lattices were designed to absorb oblique impacts more effectively. Thus, off-axis impact absorption was tested by offsetting the weak side of the sample and subjecting the lattice to an oblique impact as shown in the Figure 4.24 cross-sections.

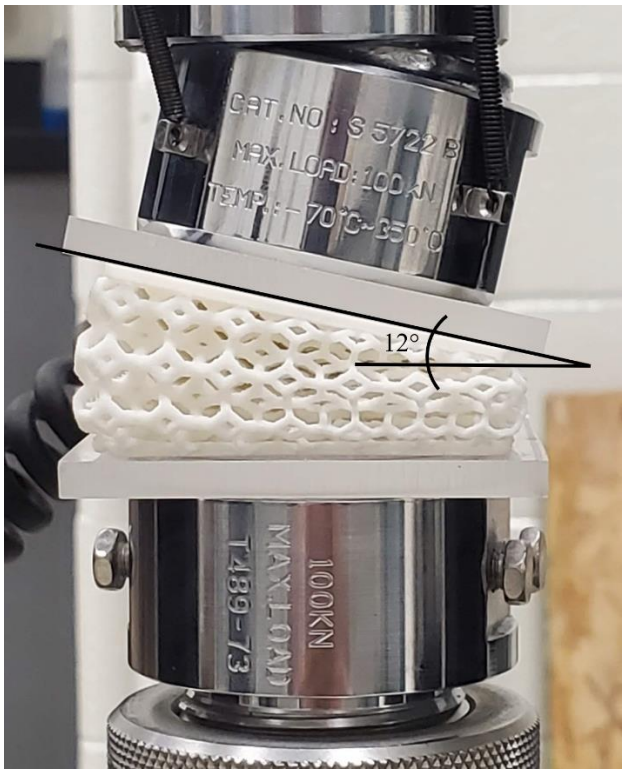

Figure 4.21: Self-aligning platen on the Instron universal testing machine compressing a side-graded TPE 300 lattice. The angle was found to be 12°.

For the initialization and verification of the FEA model, impacts with existing data were repeated in ANSYS. A modeled 5 cm impact is shown below in Figure 4.22 with the overlaid non-graded TPE 300 real impact data. The Ogden 3rd order modified parameters increased model accuracy considerably, which enabled the use of FEA to predict the behavior under various new circumstances.

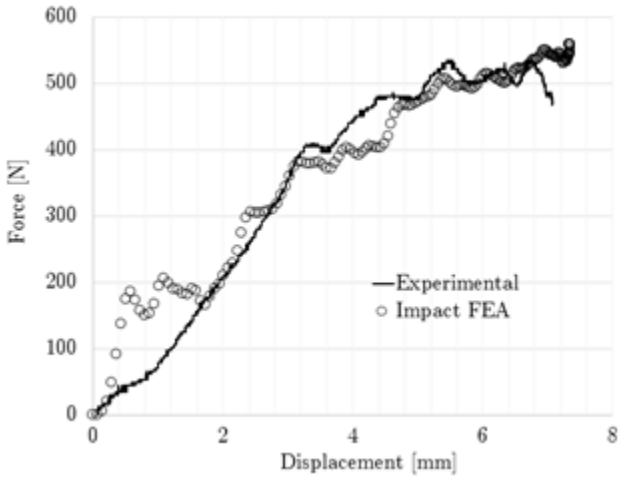

Figure 4.22: FEA model and experimental data for a 5 cm impact on non-graded TPE 300.

After the FEA model was verified against an existing data set, the platen was angled to induce an oblique impact, like in real testing. Here, non-graded and side-graded lattices were placed in the impact zone to absorb the energy. A frame-by-frame impact of side-graded TPE 300 is displayed in Figure 4.23. Red shows struts under compression, while blue shows struts unaffected by the impact. The side-grading is apparent in Figure 4.23, where the orientation of the lattice during the side-graded impacts is shown. Weaker struts are subjected to the impactor first, and the lattice progressively stiffens as the struts thicken.

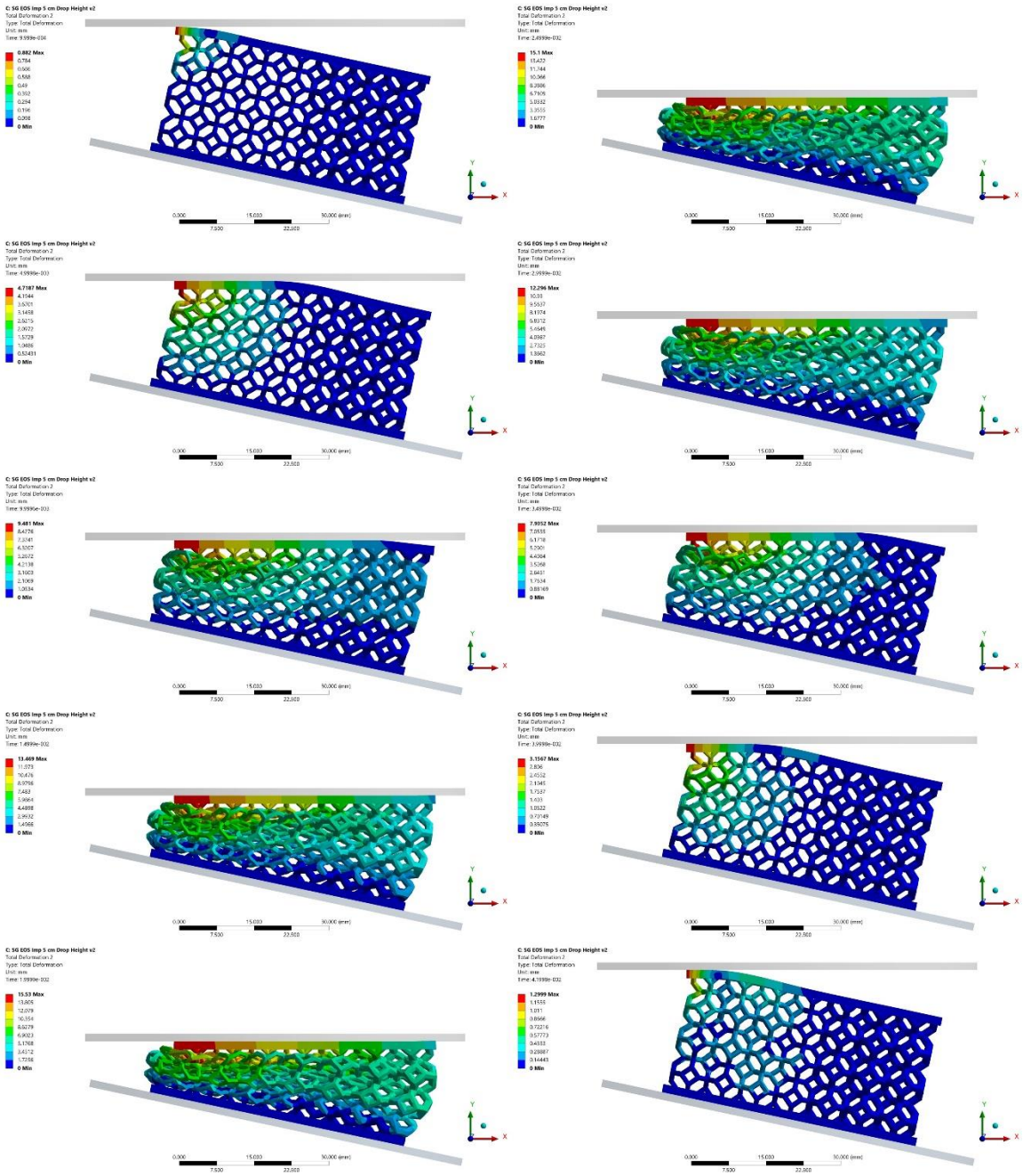

Figure 4.23: Frame-by-frame procession of impact with FEA modeling. Red represents areas of high stress and blue represents areas of low stress.

Figure 4.24 shows the produced force versus time curve from the pictured impact in ANSYS software overlaid with the experimentally derived data from physical impacts. By performing these impact tests with both non-graded and side-graded lattices, the types of grading can be compared with regards to their oblique impact absorption capability. Table

4.2 shows the acceleration results of the testing. Note the lower average acceleration of any side-graded configuration over the non-graded lattices. Even when reversing the direction of the side-graded lattice on the bottom platen by 180°, the side-graded TPE 300 still showed superior absorption capability.

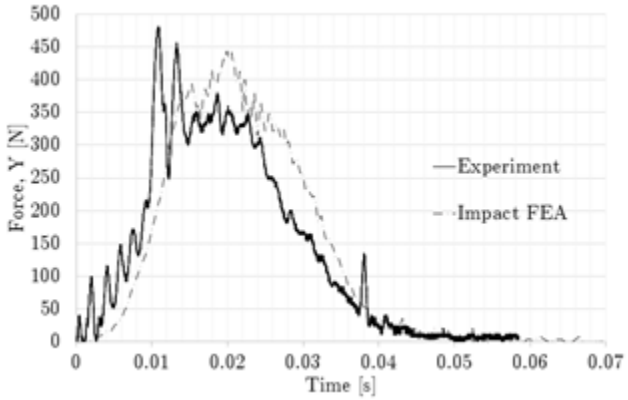

Figure 4.24: Force-time curves for SG TPE 300 experimental impact and FEA impact.

Table 4.2: Average accelerations from assorted impacts and spatial variations.

Impact Scenario	*Average Acceleration (x1000 m/s^2)*
NG Linear	82.7
NG Oblique	74.1
SG Oblique	28.0
Inverse SG Oblique	35.6

4.4 Helmet System

Individual lattices can give a snapshot of the performance ability during some impacts, but sometimes a full model is needed for more accurate testing. The Hybrid 2 configuration was tested in a more robust manner with a full helmet setup. The testing apparatus consisted of the modified low velocity impact tower, a polyester sphere to act as a "head", and an industry-standard polycarbonate helmet shell. The helmet was layered with Hybrid 2 padding between the shell and the sphere. Overall, the entire impacting

system weighed 15.9 kg, which coincides with the weight of the impactor in the official NFL helmet testing protocol [107]. The 15.9 kg impactor combined with a drop height of 40 cm resulted in an impact velocity of about 2.8 m/s and an impact energy of 62.39 J. The lattices were arranged in such a way to provide comfort to the wearer and reduce oblique accelerations. The arrangement chosen, outlined in Figure 4.25, consisted of vertically-graded TPE 300 along the shell with the stiff side facing outwards and non-graded NinjaFlex along the inside of the padding where the "head" contacts the cushioning. The softer NinjaFlex was oriented towards the head to improve comfort and low energy absorption.

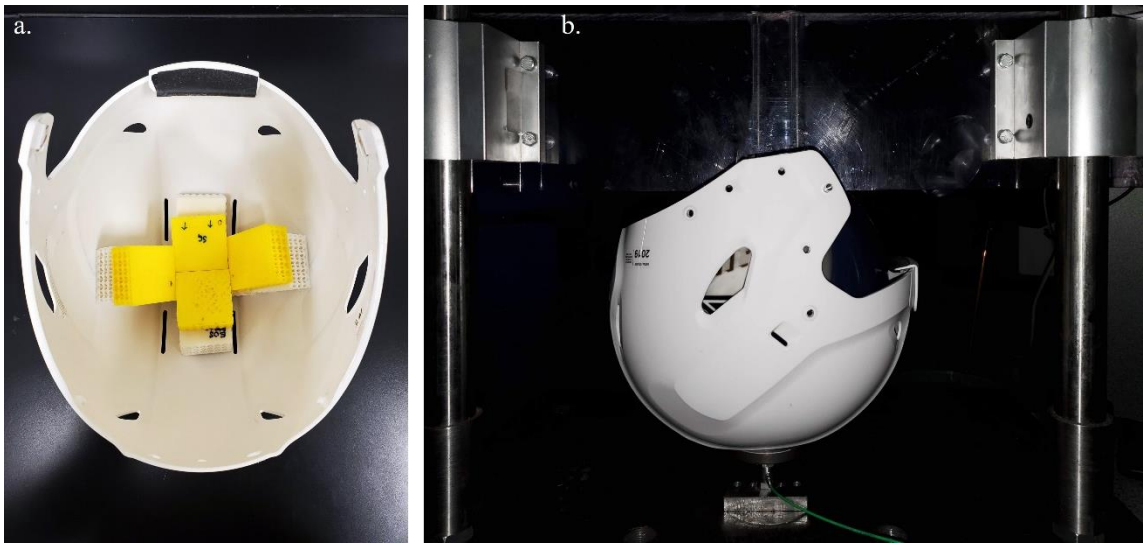

Figure 4.25: Inside view of helmet shell containing VG TPE 300 and NG NinjaFlex lattices (from the Hybrid 2 arrangement). Also, (b) shows the full helmet apparatus mounted to the linear ball bearings from Figure 3.7.

The full helmet system was tested in a similar manner to the previous lattice arrangements and analyzed in the same way. Both force-time and force-displacement curves were generated for the 62.39 J impact and are pictured in Figure 4.26 below. Also included in the figure is a sample curve generated from impacting a traditional helmet padding in the same manner. Due to the extremely high impact energy, the amplifier sensitivity was adjusted to fit the entire curve in one graph, causing the low end of the impact to disappear into the oscilloscope digital noise. Therefore, force looks to be a flat

zero line until the impact begins to be significantly absorbed. Integrating the force-displacement graph until densification yields absorbed energy, which amounts to 4.86 J. The low absorbed energy of the helmet system is explained by bouncing of the helmet system after impact. Rebounding of the apparatus is not desirable as it could cause head or neck injuries on impact. Traditional helmet padding tests did not produce much bouncing and almost instantly absorbed the entire impact. Further tuning of the lattices may be able to reduce the oscillation observed.

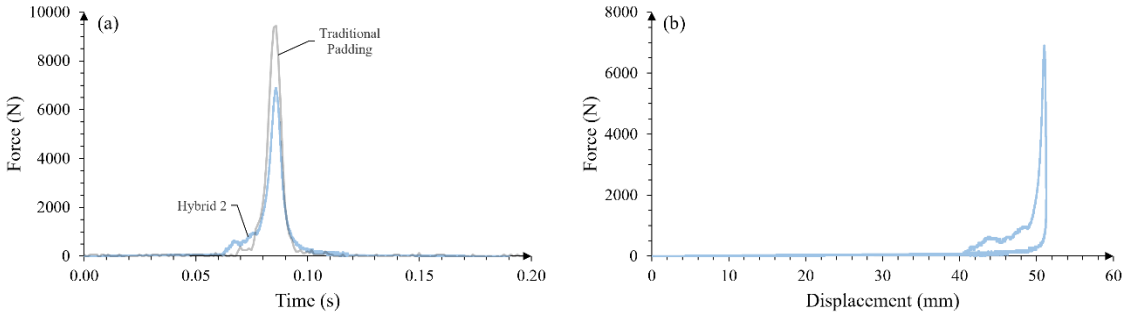

Figure 4.26: Force profiles for the 62.39 J helmet impact (40 cm). The grey curve in (a) shows a traditional helmet foam performance during the same test.

Acceleration of the helmet was also tracked to determine if the impact would have resulted in injury. The acceleration curve can be seen in Figure 4.27 with an oscillatory nature. The bouncing of the helmet likely caused these oscillations and may contribute to different injuries in the neck and spine than brain injuries like concussions. Since the acceleration never exceeded 5 g, the impact should be considered safe with regards to TBI; however, rapid energy return is not a desired result in helmets. As mentioned previously, further lattice tuning, better material selection, and different lattice arrangements may provide a better impact mitigation strategy than the current Hybrid 2 system in a helmet.

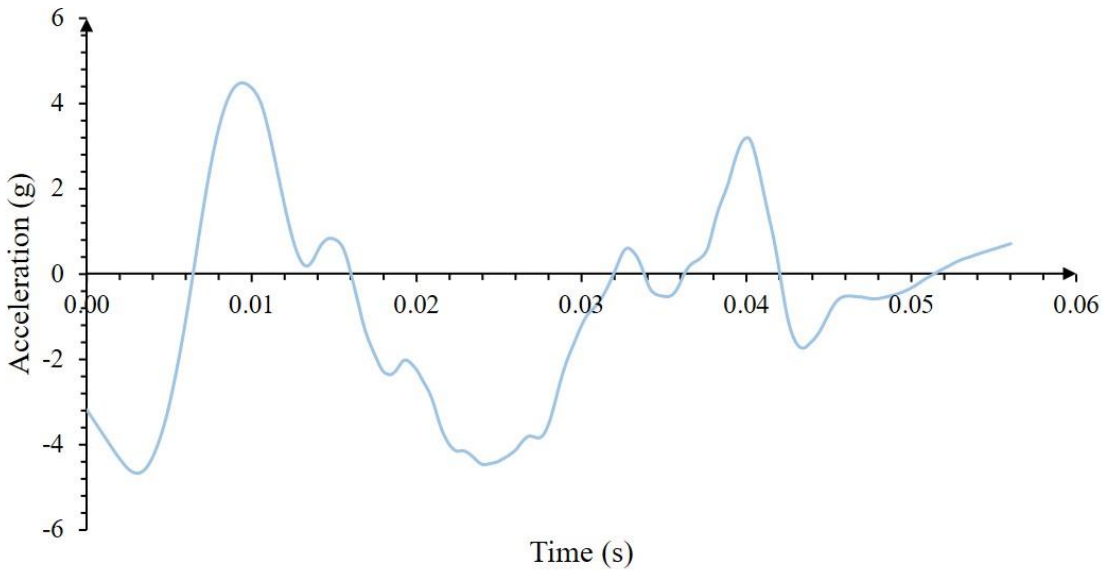

Figure 4.27: Acceleration response of the helmet system outfitted with Hybrid 2 padding. Oscillations are observed due to bouncing of the system after impact.

4.5 Embedded Sensor System

Following the testing of all lattices and hybrid systems, a lattice embedded with a flexible sensor was impacted. The schematic shown in Figure 3.11 outlines how the sensor system was connected to the MCU or oscilloscope. Initial testing combined the use of an MCU with the traditional load cell and oscilloscope setup to compare reliability and performance of the sensor signal. The results of a 28.34 J impact (60 cm with the same 4.66 kg platen) are shown in Figure 4.28. Since the curves follow almost exactly the same path and exhibit no deviation from one another, the MCU data was determined to be accurate and useful for more mobile applications.

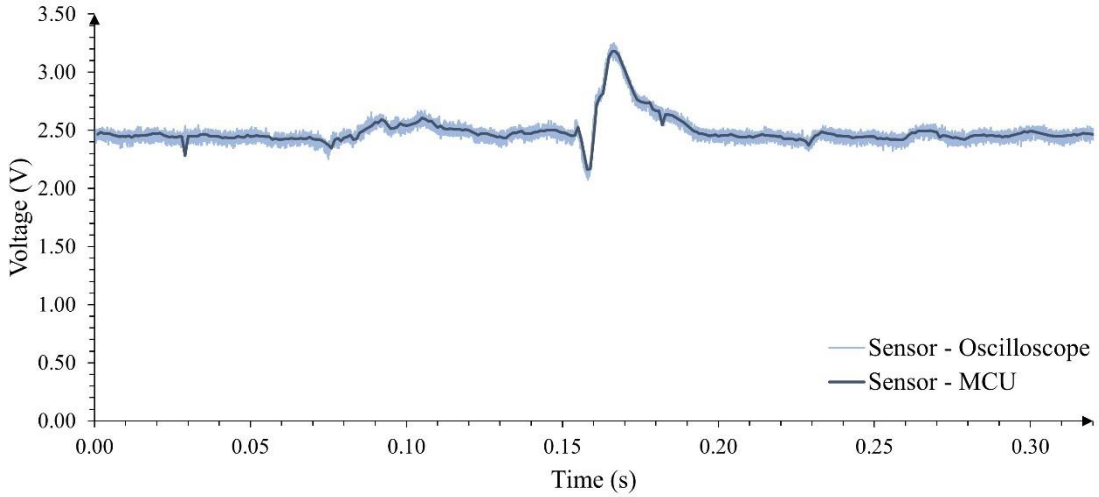

Figure 4.28: Oscilloscope data (light) overlaid with MCU data (dark) to compare accuracy of MCU processing with an existing reliable collection method.

Further testing was performed on the lattice-sensor combination with the oscilloscope for ease of use and known accuracy. The lattice was impacted in the normal low velocity impact tower with the 4.66 kg platen from eight heights (5 cm to 60 cm) to collect data for various impact energies. Load cell information was simultaneously collected in an alternate oscilloscope channel to eventually construct a fitting curve. Figure 4.29 shows 7.77 J and 28.34 J impacts with both load cell voltages and sensor voltages. Since the impact curves shown below are only raw voltage, the actual voltage change observed in the oscilloscope in Figure 4.29b would be four times greater than pictured in the graph. The increase is due to a decrease in sensitivity of the amplifier to fit the entire peak in one frame.

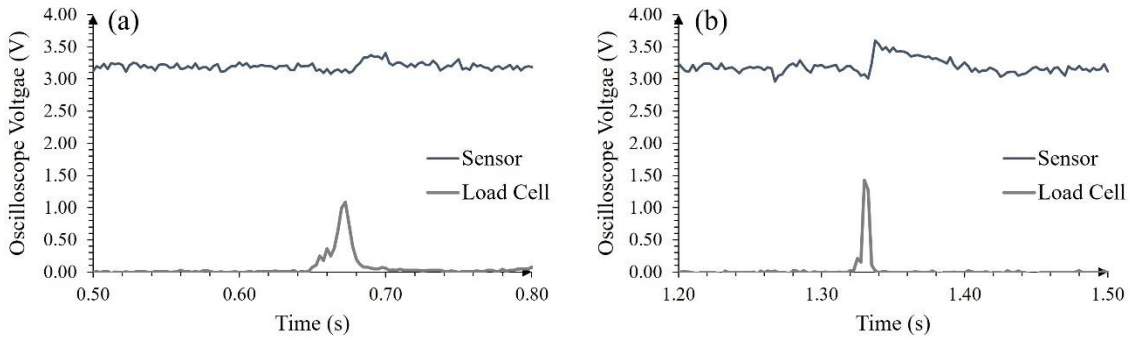

Figure 4.29: Comparison of sensor output voltages and traditional load cell output voltages during the (a) 7.77 J impact and (b) 28.34 J impact.

To compare the peak voltages from sensor data and load cell data, a baseline was established for both. The sensor voltage held relatively constant at 3.20 V before and after the impact. Alternatively, the load cell held constant at 0.00 V before and after the impact. Peak voltage was calculated as the maximum difference from the baseline voltage. Also, since the amplifier yields a voltage to force conversion (which eliminates the decrease in sensitivity), the maximum voltage from the sensor was charted versus peak force from the load cell to form a fitting curve. The trendline was predicted to be of exponential nature and parameters were determined with Excel. Figure 4.30 shows the points of the eight impacts and their relationship to the fitted curve. Also, Equation 5 shows the formula used to generate the fitting line. Equation 5 can be used to predict peak forces with the sensor voltage information and can be quickly calculated in an MCU to determine severity of impacts.

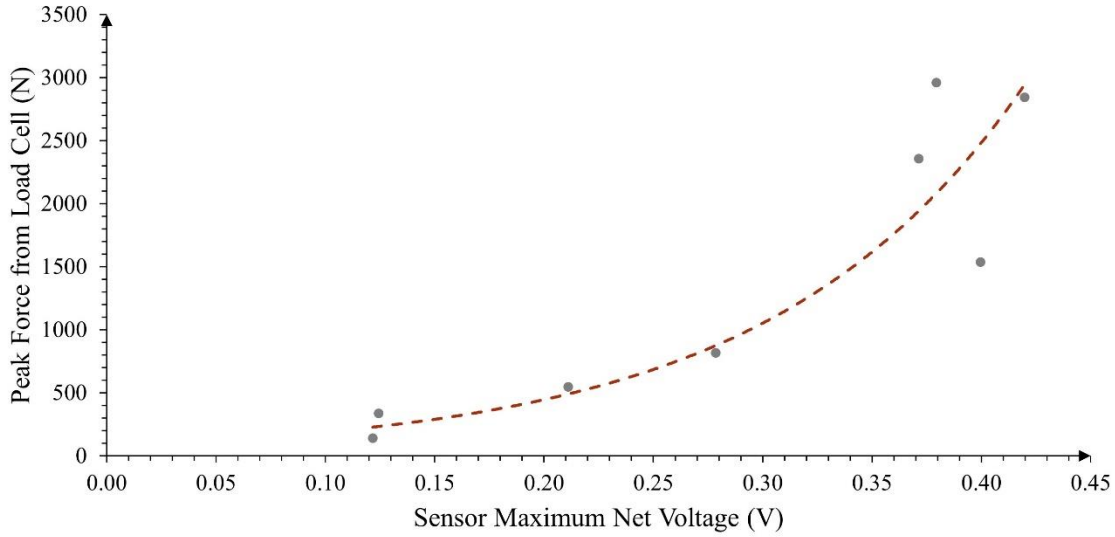

Figure 4.30: Eight impact heights from load cell and sensor data. Force (N) was derived from the load cell amplifier to find a conversion for the sensor data.

$$y = 79.993e^{8.5891x} \quad (5)$$

5.0 Conclusions

Additively manufactured elastomeric materials have many applications in personal protective equipment. Elastomeric lattices combine versatility of materials with the tailorability of additive manufacturing. Different designs are easily tested and rapidly created. In addition, AM allows for variation in strength of lattice supports at specific points to provide more or less cushioning ability. Spatial variation of lattice strut sizes contributes to efficient energy absorption in general impact situations and more effective acceleration reduction in oblique impacts.

Five elastomers were tested extensively in this research: Carbon SIL 30, Ultimaker TPU 95A, EOS TPE 300, FormLabs Rebound, and NinjaTek NinjaFlex. Kelvin cell lattices were printed with these materials in three types of spatial grading: non-graded, vertically-graded, and side-graded. All lattice samples were subjected to quasi-static compression testing for stiffness and efficiency analysis and low velocity impact testing for dynamic energy absorption capability quantification. Also, two hybrid combinations were formed and tested to analyze how lattice materials interact upon impact. Hybrid 1 consisted of vertically-graded SIL 30 and vertically-graded TPU 95A. Hybrid 2 was made of non-graded NinjaFlex and vertically-graded TPE 300. Both hybrid lattices showed results throughout various tests that were consistent with a compromise in performance between the two individual materials. A Hybrid 2 padding arrangement was tested in a polycarbonate helmet shell with a heavier impactor to test the bulk system performance. FEA modeling of side-graded lattices permitted the exploration of oblique impact performance and comparisons with other lattice gradations without much physical testing. Finally, a flexible IL-based sensor from the University of Akron was included in a FormLabs Elastic 50A Kelvin cell lattice to test data collection from a self-contained system.

From the initial compression data, SIL 30 was found to be the least stiff material (over 15 times lower Young's modulus than TPU 95A, the stiffest material tested). Also, quasi-static compression testing yielded interesting EAE curves for each spatial variation. Non-graded lattices peaked in efficiency later in their displacement while vertically-graded samples showed an early efficiency peak with subsequent linear decline due to the weaker

layer of struts. During phases 1 and 2 of impact testing, stiffer materials were found to require greater energy to densify the lattice, and therefore performed better at higher impact energies. These materials include TPE 300, Rebound, and TPU 95A. Alternatively, low stiffness materials were very effective at absorbing extremely small amounts of impact energy, which may be of use in light cushioning and comfort scenarios.

Hybrid 1 and Hybrid 2 showed results falling in between their constituent materials, proving that combinations of lattices could produce a wider range of acceptable performance than just one single material with a varied design. Layering soft and firm lattices yielded a system capable of absorbing low energy and higher energy impacts. Soft materials enabled low energy impacts to be lengthened up to 60 ms, almost a 2 times increase over the stiffer materials. However, firm materials like TPU 95A and TPE 300 contributed to a better performance at the 10.06 J energy level and higher, with peak accelerations never exceeding 17 g (31 g was achieved with the much softer double-stacked SIL 30 sample at this energy level). Varying the materials as well as the lattice designs should yield interesting combination possibilities for future customized protective padding.

Hybrid 2 was employed in a traditional polycarbonate helmet shell mounted to a 15.9 kg impactor. The heavier system subjected the lattice arrangement to 62.39 J of impact energy at 2.8 m/s when dropped from 40 cm. Even though the system bounced off the initial impact, acceleration did not exceed 5 g, which would make TBI extremely unlikely. Further improvements could be made with regards to material selection, lattice design, and arrangement, but initial results show promise for the usage of an AM-based helmet liner.

Side-graded lattices from phase 2 of testing (TPE 300, Rebound, and NinjaFlex) were impacted at a 12° angle to analyze oblique impact absorption capability; these off-axis impacts are a leading cause of TBI. FEA modeling showed that the side-graded lattices were very effective at reducing the impact acceleration when compared to the normal non-graded lattices. In fact, average acceleration was reduced by over half when side-graded lattices were impacted with the same energy compared to non-graded lattices. The result here is important in the reduction of oblique impact-related head injuries.

Finally, the IL-based flexible sensor was seamlessly integrated into an elastomeric Kelvin cell lattice. Wires protruding from the lattice connecting the CNT traces to a circuit carried a voltage. The voltage changed based on the amount of compression the lattice

underwent. By analyzing and comparing voltage data from both the sensor and the load cell with a multi-channel oscilloscope, a fitted curve was created to convert flexible sensor peak voltage to peak force. The equation used here can be integrated with an MCU to repeatedly calculate peak forces during impacts to determine probability of injury. The sensor system combined with a Bluetooth module on the MCU will eventually relay data to a remote crew, where analysis and decision-making will take place. Additively manufactured lattices enable vast customizability, sensor integration, and rapid material modification for personal protective equipment and padding replacements.

References

1. Maheo L, Viot P. Impact on multi-layered polypropylene foams. Int J Impact Eng. 2013;53: 84–93.
2. Rethinking foam - the Carbon lattice innovation. In: Carbon [Internet]. [cited 29 Jan 2021]. Available: https://www.carbon3d.com/resources/whitepaper/rethinking-foam-carbons-lattice-innovation/
3. Carradero Santiago C, Randall-Posey C, Popa A, Duggen L, Vuksanovich B, Cortes P, et al. 3D Printed Elastomeric Lattices With Embedded Deformation Sensing. IEEE Access. 2020;8: 41394–41402.
4. Al-Ketan O, Rowshan R, Abu Al-Rub RK. Topology-mechanical property relationship of 3D printed strut, skeletal, and sheet based periodic metallic cellular materials. Additive Manufacturing. 2018;19: 167–183.
5. Corrales MA, Gierczycka D, Barker J, Bruneau D, Bustamante MC, Cronin DS. Validation of a Football Helmet Finite Element Model and Quantification of Impact Energy Distribution. Ann Biomed Eng. 2020;48: 121–132.
6. W. Johnson, J. Skorecki, S. R. Reid. The Gadd Severity Index and Measurements of Acceleration when Heading an Association Football. 1975; 187–196.
7. Khosroshahi SF, Duckworth H, Galvanetto U, Ghajari M. The effects of topology and relative density of lattice liners on traumatic brain injury mitigation. Journal of Biomechanics. 2019. p. 109376. doi:10.1016/j.jbiomech.2019.109376
8. Alizadeh HV, Fanton MG, Domel AG, Grant G, Camarillo D. A Computational Study of Liquid Shock Absorption for Prevention of Traumatic Brain Injury. Journal of Biomechanical Engineering. 2020. doi:10.1115/1.4049155
9. Clough EC, Plaisted TA, Eckel ZC, Cante K, Hundley JM, Schaedler TA. Elastomeric Microlattice Impact Attenuators. Matter. 2019;1: 1519–1531.
10. RIDDELL DIAMOND TECHNOLOGY. [cited 8 Sep 2021]. Available: https://content.riddell.com/Diamond/
11. Chen X, Zhang C, Ma C, Liu H, Zheng Y, Jiang Y, et al. Evaluation of Helmet Comfort Based on Flexible Pressure Sensor Matrix. Intelligent Human Systems Integration 2019. Springer International Publishing; 2019. pp. 833–839.
12. U.S. Army CCDC Army Research Laboratory Public Affairs. Future Soldiers may get improved helmet padding. In: U.S. Army [Internet]. 19 Feb 2020 [cited 20 May 2021]. Available: https://www.army.mil/article/232871/future_soldiers_may_get_improved_helmet_padding
13. Khosroshahi SF, Tsampas SA, Galvanetto U. Feasibility study on the use of a hierarchical lattice architecture for helmet liners. Materials Today Communications. 2018;14: 312–323.
14. Fernandes FAO, Alves de Sousa RJ. Motorcycle helmets--a state of the art review. Accid Anal Prev. 2013;56: 1–21.
15. Protective Packaging Market Share. In: Grand View Research [Internet]. Nov 2017 [cited 27 May 2021]. Available: https://www.grandviewresearch.com/industry-analysis/protective-packaging-market

16. Soe S, Ryan M, McShane G, Theobald P. Energy absorbing characteristics of additively manufactured TPE cellular structures. InImpact: The Journal of Innovation Impact. 2016;8: 145.
17. Ge C, Priyadarshini L, Cormier D, Pan L, Tuber J. A preliminary study of cushion properties of a 3D printed thermoplastic polyurethane Kelvin foam. Packag Technol Sci. 2018;31: 361–368.
18. Ashby MF. The properties of foams and lattices. Philos Trans A Math Phys Eng Sci. 2006;364: 15–30.
19. Maiti A, Small W, Lewicki JP, Weisgraber TH, Duoss EB, Chinn SC, et al. 3D printed cellular solid outperforms traditional stochastic foam in long-term mechanical response. Sci Rep. 2016;6: 24871.
20. Ashby MF. Materials and the Environment: Eco-informed Material Choice. Elsevier; 2012.
21. Hawreliak JA, Lind J, Maddox B, Barham M, Messner M, Barton N, et al. Dynamic Behavior of Engineered Lattice Materials. Sci Rep. 2016;6: 28094.
22. Principles—Terminology AM. ISO/ASTM 52900. International Organization for Standardization: Geneva, Switzerland. 2015.
23. Moore JP, Williams CB. Fatigue characterization of 3D printed elastomer material. International Solid Freeform Fabrication Symposium. 2012. pp. 641–655.
24. Janusziewicz R, Tumbleston JR, Quintanilla AL, Mecham SJ, DeSimone JM. Layerless fabrication with continuous liquid interface production. Proc Natl Acad Sci U S A. 2016;113: 11703–11708.
25. Tumbleston JR, Shirvanyants D, Ermoshkin N. Continuous liquid interface production of 3D objects. 2015. Available: https://science.sciencemag.org/content/347/6228/1349.abstract?casa_token=9n0B0O0_hAkAAAAA:hU_PyV3JPeVpcYTLUwpOF3-3P3jixOomc2yi1eKqzG1r01MBRRGwzRuKsXkPA2bUZQvBs0dGgmPsPw
26. Herzberger J, Sirrine JM, Williams CB, Long TE. Polymer Design for 3D Printing Elastomers: Recent Advances in Structure, Properties, and Printing. Prog Polym Sci. 2019;97: 101144.
27. El-Helou C, Harne RL. Exploiting functionally graded elastomeric materials to program collapse and mechanical properties. Adv Eng Mater. 2019;21: 1900807.
28. Digital Foam - 3D Printing with Foam. In: EOS [Internet]. [cited 29 Jan 2021]. Available: https://www.eos.info/press/digital-foam
29. Taormina G, Sciancalepore C, Messori M, Bondioli F. 3D printing processes for photocurable polymeric materials: technologies, materials, and future trends. J Appl Biomater Funct Mater. 2018;16: 151–160.
30. Pranzo D, Larizza P, Filippini D, Percoco G. Extrusion-Based 3D Printing of Microfluidic Devices for Chemical and Biomedical Applications: A Topical Review. Micromachines (Basel). 2018;9. doi:10.3390/mi9080374
31. Alexandre A, Cruz Sanchez FA, Boudaoud H, Camargo M, Pearce JM. Mechanical Properties of Direct Waste Printing of Polylactic Acid with Universal Pellets Extruder: Comparison to Fused Filament Fabrication on Open-Source Desktop Three-Dimensional Printers. 3D Printing and Additive Manufacturing. 2020;7: 237–247.

32. Lindberg A, Alfthan J, Pettersson H, Flodberg G, Yang L. Mechanical performance of polymer powder bed fused objects – FEM simulation and verification. Additive Manufacturing. 2018;24: 577–586.
33. Emon MOF, Alkadi F, Philip DG, Kim D-H, Lee K-C, Choi J-W. Multi-material 3D printing of a soft pressure sensor. Additive Manufacturing. 2019;28: 629–638.
34. Fleck NA. An overview of the mechanical properties of foams and periodic lattice materials. [cited 17 Jun 2021]. Available: http://citeseerx.ist.psu.edu/viewdoc/download?doi=10.1.1.507.4009&rep=rep1&type=pdf
35. Wallach JC, Gibson LJ. Mechanical behavior of a three-dimensional truss material. Int J Solids Struct. 2001;38: 7181–7196.
36. Soe SP, Martin P, Jones M, Robinson M, Theobald P. Feasibility of optimising bicycle helmet design safety through the use of additive manufactured TPE cellular structures. Int J Adv Manuf Technol. 2015;79: 1975–1982.
37. Thompson DC, Rivara FP, Thompson R. Helmets for preventing head and facial injuries in bicyclists. Cochrane Database Syst Rev. 2000; CD001855.
38. Hexr 3D Prints Custom Inner Shells For Their Bicycle Helmets. 13 Nov 2019 [cited 29 Sep 2021]. Available: https://3dprinting.com/3d-printing-use-cases/hexr-3d-prints-custom-inner-shells-for-their-bicycle-helmets/
39. Willinger R. Expertise on Helmet Evaluation: Hexr. Universite De Strasbourg; 2020 May. Available: https://cdn.shopify.com/s/files/1/0059/6659/4161/files/Expt_Report-HEXR.pdf?v=1591892735
40. HEXR's breakthrough safety test results. [cited 29 Sep 2021]. Available: https://hexr.com/blogs/all/hexrs-breakthrough-safety-test-results
41. Conehead Helmets. [cited 13 Sep 2021]. Available: http://coneheadhelmets.com.au/
42. Bicycle Helmet Liners: Foam and much more. [cited 13 Sep 2021]. Available: https://helmets.org/liners.htm
43. How Does a Football Helmet Protect a Football Player? 27 Jun 2019 [cited 13 Sep 2021]. Available: https://www.sportsrec.com/football-helmet-protect-football-player-4740646.html
44. Busuttil A, Keeling J. Paediatric Forensic Medicine and Pathology. CRC Press; 2008. pp. 338–339.
45. Brückner K, Odenwald S, Schwanitz S, Heidenfelder J, Milani T. Polyurethane-foam midsoles in running shoes - impact energy and damping. Procedia Engineering. 2010;2: 2789–2793.
46. Shin J, Kim S, Jeong D, Lee HG, Lee D, Lim JY, et al. Finite Element Analysis of Schwarz P Surface Pore Geometries for Tissue-Engineered Scaffolds. Math Probl Eng. 2012;2012. doi:10.1155/2012/694194
47. Yu S, Sun J, Bai J. Investigation of functionally graded TPMS structures fabricated by additive manufacturing. Mater Des. 2019;182: 108021.
48. Maskery I, Sturm L, Aremu AO, Panesar A, Williams CB, Tuck CJ, et al. Insights into the mechanical properties of several triply periodic minimal surface lattice structures made by polymer additive manufacturing. Polymer . 2018;152: 62–71.

49. Yoo D-J. Advanced porous scaffold design using multi-void triply periodic minimal surface models with high surface area to volume ratios. International Journal of Precision Engineering and Manufacturing. 2014;15: 1657–1666.
50. Vijayavenkataraman S, Kuan LY, Lu WF. 3D-printed ceramic triply periodic minimal surface structures for design of functionally graded bone implants. Mater Des. 2020;191: 108602.
51. Peng H, Gao F, Hu W, Itamco 1. Design, modeling and characterization of triply periodic minimal surface heat exchangers with additive manufacturing. [cited 19 Aug 2021]. Available: https://utw10945.utweb.utexas.edu/sites/default/files/2019/194%20Design,%20Modeling%20and%20Characterization%20of%20Triply%20Pe.pdf
52. Fang H, Li S, Thota M, Wang KW. Origami lattices and folding-induced lattice transformations. Phys Rev Research. 2019;1: 023010.
53. Robinson M, Soe S, McShane G, Celeghini R, Burek R, Alves M, et al. Developing Elastomeric Cellular Structures for Multiple Head Impacts. 2017 IRCOBI ConferenceInternational Research Council on Biomechanics of Injury (IRCOBI). 2017. Available: https://trid.trb.org/view/1486037
54. Silverberg JL, Evans AA, McLeod L, Hayward RC, Hull T, Santangelo CD, et al. Applied origami. Using origami design principles to fold reprogrammable mechanical metamaterials. Science. 2014;345: 647–650.
55. Iyibilgin O, Yigit C, Leu MC. Experimental investigation of different cellular lattice structures manufactured by fused deposition modeling. 2013; 895–907.
56. Purple. The Purple Mattress. 13 Sep 2021 [cited 1 Oct 2021]. Available: https://purple.com/mattresses/purple-bed/2
57. Bates SRG, Farrow IR, Trask RS. Compressive behaviour of 3D printed thermoplastic polyurethane honeycombs with graded densities. Mater Des. 2019;162: 130–142.
58. PolyJet – 3D Printing Technologies Simply Explained. 29 Jun 2019 [cited 27 Sep 2021]. Available: https://all3dp.com/2/polyjet-3d-printing-technologies-simply-explained/
59. Tango: A Soft Flexible 3D Printing Material. [cited 27 Sep 2021]. Available: https://www.stratasys.com/materials/search/tango
60. Ge C, Cormier D, Rice B. Damping and cushioning characteristics of Polyjet 3D printed photopolymer with Kelvin model. J Cell Plast. 2021;57: 517–534.
61. Bates SRG, Farrow IR, Trask RS. 3D printed polyurethane honeycombs for repeated tailored energy absorption. Mater Des. 2016;112: 172–183.
62. NinjaTek. NinjaTek Technical Specifications. 2016 Apr. Available: https://ninjatek.com/wp-content/uploads/2019/10/NinjaFlex-TDS.pdf
63. NinjaTek SemiFlex TPU Filament, 3.00mm, .75kg, Water. [cited 27 Sep 2021]. Available: https://3dmakerworld.com/products/ninjatek-semiflex-tpu-filament-3-00mm-75kg-water
64. SemiFlex Technical Data Sheet. Available: https://www.3dmensionals.de/media/pdf/cf/33/7e/SemiFlex-TDS.pdf
65. NinjaFlex Technical Data Sheet. Available: https://ninjatek.com/wp-content/uploads/NinjaFlex-TDS.pdf

66. Hermanson E, Soots K. 3D Printing of Thermoplastic Polyurethane. Estonian University of Life Sciences Institute of Technology XI Master Students Conference. 2017. pp. 69–74.
67. Ultimaker TPU 95A TDS. In: Ultimaker Support [Internet]. 9 Apr 2020 [cited 22 Jul 2021]. Available: https://support.ultimaker.com/hc/en-us/articles/360012664440-Ultimaker-TPU-95A-TDS
68. Ahmed W, Alnajjar F, Gochoo M, Al Jazzar B, Medha MAP. Effectiveness of 3D Printing Technologies for Developing Ventilators. Evolutions of 3D Printing Technology for Fighting COVID-19 Pandemic. 2020.
69. DLS 3D Printing Technology. 19 Jun 2020 [cited 29 Sep 2021]. Available: https://www.carbon3d.com/carbon-dls-technology/
70. Flexible Polyurethane (FPU 50) - 3D printing material. 12 Feb 2020 [cited 29 Sep 2021]. Available: https://www.fastradius.com/resources/flexible-polyurethane-fpu/
71. SIL 30. 5 Nov 2019 [cited 29 Sep 2021]. Available: https://www.fastradius.com/resources/silicone-sil/
72. FPU 50. 23 Jun 2020 [cited 29 Sep 2021]. Available: https://www.carbon3d.com/materials/fpu-50/
73. Thrasher CJ, Schwartz JJ, Boydston AJ. Modular Elastomer Photoresins for Digital Light Processing Additive Manufacturing. ACS Appl Mater Interfaces. 2017;9: 39708–39716.
74. SIL 30 - Carbon3D. In: Carbon [Internet]. [cited 29 Jan 2021]. Available: https://www.carbon3d.com/materials/sil-30/
75. Imbrie-Moore AM, Park MH, Zhu Y, Paulsen MJ, Wang H, Woo YJ. Quadrupling the N95 Supply during the COVID-19 Crisis with an Innovative 3D-Printed Mask Adaptor. Healthcare (Basel). 2020;8. doi:10.3390/healthcare8030225
76. FormLabs. Rebound Material Data Sheet. 2020 Mar. Available: https://formlabs-media.formlabs.com/datasheets/2001344-TDS-ENUS-0_1.pdf
77. Rebound Resin: A Production-Ready Elastic 3D Printing Material. [cited 7 Oct 2021]. Available: https://formlabs.com/materials/rebound/
78. Formlabs & New Balance: The Future of Performance Products With Customized Shoes. [cited 7 Oct 2021]. Available: https://formlabs.com/customer-stories/newbalance/
79. Flexible 80A Technical Data Sheet. Available: https://formlabs-media.formlabs.com/datasheets/2001418-TDS-ENUS-0.pdf
80. Elastic 50A Technical Data Sheet. Available: https://formlabs-media.formlabs.com/datasheets/2001420-TDS-ENUS-0.pdf
81. Gessler M, Galba MJ, Oberhofer J. Method of manufacturing a three-dimensional object having an internal structure. US Patent. 10259041, 2019. Available: https://patents.google.com/patent/US10259041B2/ko
82. EOS. EOS Sees Rise in New Applications Developed with its Flexible Lattice Patent. 10 May 2021 [cited 29 Sep 2021]. Available: https://www.prnewswire.com/news-releases/eos-sees-rise-in-new-applications-developed-with-its-flexible-lattice-patent-301287793.html
83. AM Staff. EOS' Digital Foam Flexible Lattice Polymer Enables Mass Customizations. In: Additive Manufacturing [Internet]. 21 Jun 2021 [cited 1 Oct

2021]. Available: https://www.additivemanufacturing.media/products/eos-digital-foam-flexible-lattice-polymer-enables-mass-customizations
84. TPE 300 Material Data Sheet. Available: http://alm-llc.com/wp-content/uploads/2021/05/TPE-300-Data-Sheet-2021.pdf
85. EOS TPU 1301 Technical Data Sheet. 2019 Nov. Available: https://www.eos.info/03_system-related-assets/material-related-contents/polymer-materials-and-examples/tpu-1301/material_datasheet_eos_tpu_1301_core_en.pdf
86. PA 11 (Polyamide 11) for Industrial 3D Printing. [cited 29 Sep 2021]. Available: https://www.eos.info/en/additive-manufacturing/3d-printing-plastic/sls-polymer-materials/pa-11-nylon-abs-pa6
87. PA 11 Technical Data Sheet. Available: https://www.3dpartsunlimited.com/wp-content/uploads/2018/05/3D-Parts-Unlimited-Nylon-11.pdf
88. HEXR Helmet Review - Could Your Next Lid Be 3D Printed? 12 Dec 2019 [cited 29 Sep 2021]. Available: https://titaniumgeek.com/hexr-helmet-review-could-your-next-id-be-3d-printed/
89. Additive Manufacturing for Sports Articles. [cited 29 Sep 2021]. Available: https://www.eos.info/en/3d-printing-examples-applications/people-health/sports-lifestyle-consumer-goods/sports
90. Wang F, Zhu B, Shu L, Tao X. Flexible pressure sensors for smart protective clothing against impact loading. Smart Mater Struct. 2013;23: 015001.
91. Nag A, Simorangkir RBVB, Valentin E, Björninen T, Ukkonen L, Hashmi RM, et al. A Transparent Strain Sensor Based on PDMS-Embedded Conductive Fabric for Wearable Sensing Applications. IEEE Access. 2018;6: 71020–71027.
92. Jha P, Khare A. SrAl2O4:Eu,Dy mechanoluminescent flexible film for impact sensors. J Alloys Compd. 2020;847: 156428.
93. Rojas-Hernandez RE, Rubio-Marcos F, Rodriguez MÁ, Fernandez JF. Long lasting phosphors: SrAl2O4:Eu, Dy as the most studied material. Renewable Sustainable Energy Rev. 2018;81: 2759–2770.
94. Emon MOF, Choi J-W. A Preliminary Study on 3D Printed Smart Insoles With Stretchable Piezoresistive Sensors for Plantar Pressure Monitoring. ASME 2017 International Mechanical Engineering Congress and Exposition. American Society of Mechanical Engineers Digital Collection; 2018. doi:10.1115/IMECE2017-71817
95. Emon MOF, Choi J-W. Flexible Piezoresistive Sensors Embedded in 3D Printed Tires. Sensors . 2017;17. doi:10.3390/s17030656
96. Aare M, Kleiven S, Halldin P. Injury tolerances for oblique impact helmet testing. Int J Crashworthiness. 2004;9: 15–23.
97. Smith DH, Meaney DF, Shull WH. Diffuse axonal injury in head trauma. J Head Trauma Rehabil. 2003;18: 307–316.
98. Fernandes FAO, de Sousa RJA. Finite element analysis of helmeted oblique impacts and head injury evaluation with a commercial road helmet. Struct Eng Mech. 2013;48: 661–679.
99. McHenry BG. Head Injury Criterion and the ATB. ATB Users' Group. 2004. Available: https://www.mchenrysoftware.com/HIC%20and%20the%20ATB.pdf
100. Chou CC, Nyquist GW. Analytical studies of the Head Injury Criterion (HIC). SAE Technical Papers. 1974; 398–410.

101. Eppinger R, Sun E, Kuppa S. Supplement: Development of improved injury criteria for the assessment of advanced automotive restraint systems - II. [cited 8 Oct 2021]. Available: https://www.nhtsa.gov/sites/nhtsa.gov/files/finalrule_all_0.pdf
102. Newman JA, Shewchenko N. A Proposed New Biomechanical Head Injury Assessment Function - the Maximum Power Index. 2000 [cited 8 Oct 2021]. doi:10.4271/2000-01-SC16
103. Marjoux D, Baumgartner D, Deck C, Willinger R. Head injury prediction capability of the HIC, HIP, SIMon and ULP criteria. Accid Anal Prev. 2008;40: 1135–1148.
104. Lau IV, Viano DC. The Viscous Criterion — Bases and Applications of an Injury Severity Index for Soft Tissues. SAE Trans J Mater Manuf. 1986;95: 672–691.
105. Willinger R, Kang HS, Diaw B. Three-dimensional human head finite-element model validation against two experimental impacts. Ann Biomed Eng. 1999;27: 403–410.
106. Vander Vorst M, Stuhmiller J, Ho K, Yoganandan N, Pintar F. Statistically and biomechanically based criterion for impact-induced skull fracture. Annu Proc Assoc Adv Automot Med. 2003;47: 363–381.
107. Biocore. Helmet Test Protocol. Charlottesville, VA 22911; 2019 Sep. Available: https://static.www.nfl.com/image/upload/v1597314821/league/x1555pmeldebfym2qwky.pdf
108. D20 Committee. Test method for tensile properties of plastics. West Conshohocken, PA: ASTM International; 2015. doi:10.1520/d0638-14
109. Sasso M, Palmieri G, Chiappini G, Amodio D. Characterization of hyperelastic rubber-like materials by biaxial and uniaxial stretching tests based on optical methods. Polym Test. 2008;27: 995–1004.
110. Pearson I, Pickering M. The determination of a highly elastic adhesive's material properties and their representation in finite element analysis. Finite Elem Anal Des. 2001;37: 221–232.
111. Bradley GL, Chang PC, Mckenna GB. Rubber modeling using uniaxial test data. J Appl Polym Sci. 2001;81: 837–848.
112. Shahzad M, Kamran A, Siddiqui MZ, Farhan M. Mechanical Characterization and FE Modelling of a Hyperelastic Material. Mater Res. 2015;18: 918–924.
113. Reppel T, Weinberg K. Experimental Determination of Elastic and Rupture Properties of Printed Ninjaflex. TechMech. 2018;38: 104–112.
114. Heiml E, Kalteis A, Major Z. EXPERIMENTAL INVESTIGATION AND SIMULATION OF 3D-PRINTED LATTICE STRUCTURES. Australas Plant Pathol. 2019;25: 52–57.
115. Keerthiwansa R, Javorik J, Kledrowetz J, Nekoksa P. Elastomer testing: the risk of using only uniaxial data for fitting the Mooney-Rivlin hyperelastic-material model. Mater Technol. 2018;52: 3–8.
116. Bartolomé L, Aginagalde A, Martínez AB, Urchegui MA, Tato W. EXPERIMENTAL CHARACTERIZATION AND MODELLING OF LARGE-STRAIN VISCOELASTIC BEHAVIOR OF A THERMOPLASTIC POLYURETHANE ELASTOMER. Rubber Chem Technol. 2013;86: 146–164.
117. Bera M, Prabhakar A, Maji PK. Nanotailoring of thermoplastic polyurethane by amine functionalized graphene oxide: Effect of different amine modifier on final properties. Composites Part B. 2020;195: 108075.

118. Cho H, Mayer S, Pöselt E, Susoff M, in ’t Veld PJ, Rutledge GC, et al. Deformation mechanisms of thermoplastic elastomers: Stress-strain behavior and constitutive modeling. Polymer . 2017;128: 87–99.
119. Christ JF, Aliheidari N, Pötschke P, Ameli A. Bidirectional and Stretchable Piezoresistive Sensors Enabled by Multimaterial 3D Printing of Carbon Nanotube/Thermoplastic Polyurethane Nanocomposites. Polymers . 2018;11. doi:10.3390/polym11010011
120. Miao Y, He H, Li Z. Strain hardening behaviors and mechanisms of polyurethane under various strain rate loading. Polym Eng Sci. 2020;60: 1083–1092.
121. Nie Y. Cyclic tensile response of a polyurethane material. Purdue University. 2016. Available: https://docs.lib.purdue.edu/open_access_theses/977
122. Schemmer B, Kronenbitter C, Mecking S. Thermoplastic polyurethane elastomers with aliphatic hard segments based on plant-oil-derived long-chain diisocyanates. Macromol Mater Eng. 2018;303: 1700416.
123. Wang M, Shan D, Liao Y, Xia L. Investigation of inelastic behavior of elastomeric composites during loading–unloading cycles. Polym Bull. 2018;75: 561–568.
124. Yi J, Boyce MC, Lee GF, Balizer E. Large deformation rate-dependent stress–strain behavior of polyurea and polyurethanes. Polymer . 2006;47: 319–329.
125. Sarva SS, Deschanel S, Boyce MC, Chen W. Stress–strain behavior of a polyurea and a polyurethane from low to high strain rates. Polymer . 2007;48: 2208–2213.
126. Fan J, Chen A. Studying a Flexible Polyurethane Elastomer with Improved Impact-Resistant Performance. Polymers . 2019;11. doi:10.3390/polym11030467
127. Andena L, Briatico-Vangosa F, Cazzoni E, Ciancio A, Mariani S, Pavan A. Modeling of shock absorption in athletics track surfaces. Sports Eng. 2015;18: 1–10.
128. Shepherd T, Winwood K, Venkatraman P, Alderson A, Allen T. Validation of a finite element modeling process for auxetic structures under impact. Phys Status Solidi B Basic Res. 2020;257: 1900197.
129. Smith LV, Duris JG. Progress and challenges in numerically modelling solid sports balls with application to softballs. J Sports Sci. 2009;27: 353–360.
130. Welding and Gluing 3D-Printed Plastic Parts. In: AMFG / Autonomous Manufacturing [Internet]. 26 Jul 2017 [cited 22 Jul 2021]. Available: https://amfg.ai/2017/07/26/gluing-3d-printing-plastic/
131. Gaitanaros S, Kyriakides S. On the effect of relative density on the crushing and energy absorption of open-cell foams under impact. Int J Impact Eng. 2015;82: 3–13.